9-2009

Normal and Extreme Sedimentation and Physical Processes in Lake Tuborg, Ellesmere Island, Nunavut

Edward Lewis
University of Massachusetts Amherst, limno.ted@gmail.com

NORMAL AND EXTREME SEDIMENTATION AND PHYSICAL PROCESSES IN LAKE TUBORG, ELLESMERE ISLAND, NUNAVUT

A Dissertation Presented

by

EDWARD LEWIS

Submitted to the Graduate School of the
University of Massachusetts Amherst in partial fulfillment
of the requirements for the degree of

DOCTOR OF PHILOSOPHY

September 2009

Geosciences

NORMAL AND EXTREME SEDIMENTATION AND PHYSICAL PROCESSES
IN LAKE TUBORG, ELLESMERE ISLAND, NUNAVUT

A Dissertation Presented

by

EDWARD LEWIS

Approved as to style and content by:

_____
Raymond S. Bradley, Chair

_____
Julie Brigham-Grette, Member

_____
William D. McCoy Member

_____
Pierre Francus, Member

_____
David P. Ahlfeld, Member

_____
Michael L. Williams, Department Head
Department of Geosciences

ACKNOWLEDGEMENTS

The greatest thanks are owed to Chloë Stuart, who patiently, ceaselessly, and expertly supported me throughout the research and writing processes. She selflessly followed me to a new country, and helped me through good and bad times. It is a testament to her personal strength and character that during this time, she excelled at a new career, made lasting and admiring friends, and became an expert and loving mother.

My parents, Roger and Dorothea, constantly supported me. I am indebted for the combinations of characteristics that provided me with the skills of scholarship, the curiosity, and the perseverance to complete a Ph.D.

My advisor, Ray Bradley was incredibly helpful, not only for his vast expertise on arctic paleoclimatology and lake history, but also for his encouragement and development of my often vaguely formed research ideas. Equally important was Pierre Francus, who is responsible for much of the technical expertise that I gained at UMass. Although he had little to gain from it, he selflessly helped me and my project from beginning to end.

Mark Besonen and Frank Keimig are two people who should be specially thanked. They are both technical wizards, and all-round great guys, and made my time at UMass both easier and extremely enjoyable.

My field assistants at Lake Tuborg were Lesleigh Anderson, James Bradbury, Tim Cook, David Mazzucchi, Joe Rogers, Anders Romundset, Whit Patridge and Chloë Stuart. They all did wonderful jobs, provided ideas and energy, and were the best companionship available on Ellesmere Island. The students of the Climate System Research center were always inspiring and helpful. In particular, Kinuyo Kanamaru provided images from her Ph.D. project, which contributed to the results shown in Chapter 5.

The staff and pilots at the Polar Continental Shelf Project assured that we made it to and from Lake Tuborg in safety and with ease. Their equipment and support were top notch. Veco

Polar Resources need to be particularly thanked, because it was their support that allowed the 2003 field season to occur.

John Sweeney helped with the design and construction of numerous pieces of scientific equipment with little more than what is available at a hardware store and his immense talent. The Limnological Research Center, University of Minnesota-Twin Cities, provided time with on Geotek core scanners, and helped with core photography. Sheldon Smith and Carsten Braun provided data and advice on Lake Tuborg. Scott Lamoureux and Robert Gilbert at Queen's University provided hours of advice and encouragement. John Brady at Smith College provided training and time on his XRD.

This project was helped financially in many ways. It was supported by National Science Foundation (NSF) grant ATM-9708071, ATM-0402421, ARC-0454959, NSF Doctoral Dissertation Research Improvement Award 0221376, Geological Society of America graduate student grants, an Arctic Institute of North America grant-in-aid, and the Gloria A. Radke prize from the University of Massachusetts. The UMass Geosciences Department supported me by providing teaching assistantships. The Undergraduate Registrar's department also employed me for several years during my time at UMass.

ABSTRACT
NORMAL AND EXTREME SEDIMENTATION AND PHYSICAL PROCESSES IN LAKE TUBORG, ELLESMERE ISLAND, NUNAVUT

SEPTEMBER 2009

EDWARD LEWIS, B.Sc(H.)., QUEEN'S UNIVERSITY

M.S., QUEEN'S UNIVERSITY

Ph.D., UNIVERSITY OF MASSACHUSETTS AMHERST

Directed by: Professor Raymond S. Bradley

Lake Tuborg is a large lake on west-central Ellesmere Island, Nunavut. Part of the lake is meromictic, and contains trapped saltwater below about 55 m depth. The lake receives meltwater and sediments from multiple sources, including snowmelt and glacier melt.

A lake process study was undertaken from 2001-2003 at Lake Tuborg that involved obtaining profiles of water temperature, salinity, transmissivity, and dissolved oxygen. Networks of short and long sediment cores were also obtained throughout the lake.

During the last year of monitoring the lake and its sediments, a large catastrophic drainage of an ice-dammed lake occurred (a jökulhlaup). This was the largest jökulhlaup witnessed in Canada since 1947. Detailed measurements of lake conditions before, during, and after the jökulhlaup allowed the responses to be measured in great detail. The lake drained by floating its ice dam, an extremely rare drainage style in the Canadian High Arctic. The basin of Lake Tuborg closest to jökulhlaup inflow filled with fresh, cold and turbid water. A sill separates this basin from the larger more distal meromictic basin, and this sill effectively blocked turbidity currents from entering this basin. Conclusions from this phase of research include (1) salinity and temperature in the saltwater basin were minimally affected by the jökulhlaup, and (2) at a deep,

distal location, an identifiable thick, coarse-grained, non-erosive deposit was produced by the jökulhlaup.

The above conclusions allowed the varved sedimentary record to be examined for similar deposits in the past, with the assumption that similar deposits could be found in the long core record, the sediments could be dated, and that previous jökulhlaup deposits would also be non-erosive. Varve-thickness counting, Cesium-137 dating, and particle size analyses showed that prior to 1960, no similar events occurred in roughly the last thousand years. In addition, only three large jökulhlaups have occurred in the last thousand years, all of which occurred after about 1960. This significantly improves the understanding of the history of the lake, the surrounding glaciers, and the paleoclimate of the region.

The lake bottom deposits that were sampled before, during and after the 2003 jökulhlaup were extraordinarily unique. A major part of the work of characterizing these deposits involved determining the size of their constituent particles. Image analysis of sedimentary particles using backscattered electron microscope imagery is a method to determine particle size at extremely high resolution. This tool improves on existing techniques since it automates the process of statistically processing images, quantifies the percentage of disturbances on images, and allows for extremely small measurement windows relative to particle size by implementing special particle counting rules.

TABLE OF CONTENTS

LIST OF TABLES

LIST OF FIGURES

CHAPTER 1

INTRODUCTION

This project seeks to better understand the physical lake processes and deposits in High Arctic saline lakes. This is important because these types of lakes have the potential to record high resolution paleoclimatic archives in their sediment records. It is also important because their current physical conditions, and sediment-based inferences of past conditions, help us understand how the lakes have responded to climate change in the past, and how they will continue to evolve in the future.

Relatively little research has taken place in high arctic lakes, and particularly little has occurred in saltwater and glacially-fed lakes. Arctic lakes have the potential to record paleoclimatic information in their clastic sediment records without the complicating effects of human disturbance of their watersheds. The severe arctic climate promotes the formation of varves, since rivers flow and transport sediment for only a brief period during summer. This is followed by a long period of quiescence in winter, where clay size particles settle out and form clay caps on top of the coarser summer deposits. Arctic saltwater lakes have the potential to preserve finely laminated sediment records because their bottom waters typically do not mix; currents cannot move sediments once they are deposited, and bottom waters are typically anoxic, which limits bioturbation. Arctic glacially-fed lakes have the potential to record changes in summer air temperature, assuming that river flow and sediment transport are consistently related to atmospheric energy inputs. Water density relative to the density of inflowing water is an extremely important control on physical lake processes and deposits in arctic lakes, especially considering the vast differences in density between freshwater and saltwater lakes. This issue has received very little attention in the literature, so it is discussed in detail in Section 2.1.

The site chosen for this dissertation is Lake Tuborg, a large, deep lake on west-central Ellesmere Island in the Canadian High Arctic (Fig. 1.1). The lake was once a fiord, and its outlet was dammed by the advance of the Antoinette Glacier. The Agassiz Ice Cap feeds supraglacial streams into the lake from the south, while large a large snowmelt-fed watershed feeds the lake from the north. The lake is 20 km

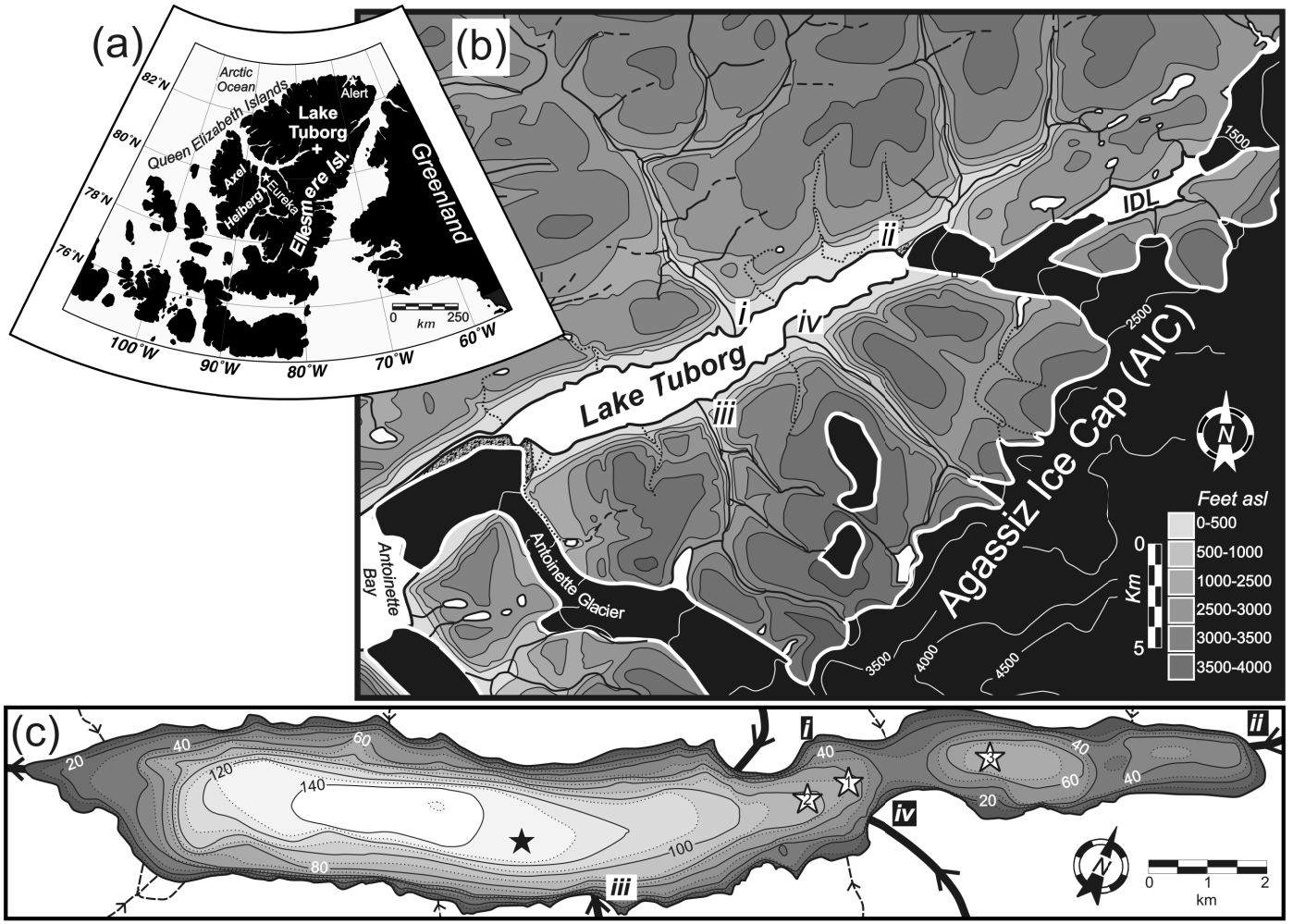

Figure 1.1. (A) Location of Lake Tuborg on Ellesmere Island in the Canadian High Arctic. (B) Physiography and topography near Lake Tuborg and the ice-dammed lake (IDL). Contour interval is 500 feet; shading is feet asl. 'i' through 'iv' mark the mouths of the major rivers that feed Lake Tuborg. (C) Lake Tuborg bathymetry and coring locations.. Solid bathymetric contours are every 20 m.

long and has an area of 42 km^2. It has two major basins. To the northeast is a 74 m deep entirely freshwater basin. The southwest portion of the lake is a much larger and deeper basin (maximum depth, 145 m), with saltwater trapped below 55 m depth. A shallow 34 m sill separates these two basins (Fig. 1.1).

When this project began, it was known that portions of the Lake Tuborg water column did not circulate (termed *meromictic*) and contained saltwater (Hattersley-Smith and Serson, 1964). It was also known that it was not a simple system with respect to its hydrology and sediment transport. A hydrologic process study was performed in 1995, where discharge and sediment transport were monitored in a large glacially fed steam. It was found that slush flows lasting only a few days were able to transport extremely large amounts of sediment. The sources of these flows were small supraglacial lakes on the Agassiz Ice Cap (Braun et al., 2000). Cores taken from several locations in the freshwater and saltwater basins revealed that sediments on the lake bottom were annually laminated (varved). The 300-year varve thickness record appeared to document air temperature changes. However, it also appeared to record extreme events in thick sand layers, which were likely a result of supraglacial lake drainages and other catastrophic processes (Smith et al., 2004). These results are reviewed in Section 2.3. It was recognized that an extremely large ice-dammed lake exists above Lake Tuborg (Fig. 1.1). However, it was not known how or when the lake drains into Lake Tuborg, or to what extent the lake drainages were recorded in the sediment record of the lake. Section 2.2 provides background and context for jökulhlaups, and the deposits they produce in downstream water bodies. Particular focus is placed on catastrophic lake drainages that have occurred in the Arctic, since they typically have unique drainage styles and are at a different phase in their evolution compared to more southerly ice-dammed lakes.

We were extremely fortunate to record a catastrophic drainage of the ice-dammed lake above Lake Tuborg at the end of the monitoring campaign in 2003. At least a third of a cubic kilometer of water drained into Lake Tuborg in less than four days. The most important observation made during this time was that although the event was extremely large, relatively low-energy processes deposited sediment far

from the point of jökulhlaup inflow. This was due to a suite of unique characteristics of Lake Tuborg, and is discussed in Chapter 3. From the perspective of the long-term evolution of Lake Tuborg, it was remarkable that the jökulhlaup did not greatly alter the salinity structure of its bottom waters. Changes in water column salinity, temperature and dissolved oxygen before, during, and after the jökulhlaup are also discussed in Chapter 3.

Chapter 3 describes a uniquely thick graded deposit that formed conformably on underlying thinner varved sediments. This allowed long cores from the same site to be examined for similar deposits. A greater than five meter sequence of overlapping sediment cores was obtained from this site. Varve counting combined with 137-Cesium dating showed that the record contained over a thousand years of laminae. Most strikingly, similar deposits to the 2003 event were only produced twice, both of which occurred after 1960. In addition, varve thickness generally increased beginning in the 19th century, which likely reflects a combination increased sediment availability within the watersheds of Lake Tuborg, and increasing air temperature following the Little Ice Age. These results are discussed in Chapter 4.

Chapter 5 describes a tool that was developed while analysing particle size in short sediment cores, the results of which contributed to Chapter 3. It was recognized that analysis of backscattered electron microscope imagery was the most appropriate technique for these short cores because they had the potential to record stratigraphy in great detail. While techniques for image analysis of sediment fabric and texture had been previously developed, the process was time intensive. Therefore, a macro was developed in the image analysis program ImageJ (Rasband, 2008). This macro has two major advantages. First, it allows extremely high resolution analyses to be performed, permitting analyses at the sub-lamina scale. Second, it largely automates the process, reducing the time required for results, and reducing the potential for user error. This macro is described in Chapter 5. Results from Lake Tuborg are shown, and the general applicability of the macro is also demonstrated by showing examples from South Sawtooth Lake, Ellesmere Island, and Saanich Inlet, Vancouver Island.

CHAPTER 2

LITERATURE REVIEW

2.1 Density in high arctic freshwater and saltwater lakes as a control for physical processes and sedimentary deposits

2.1.1 Introduction

Water density is determined by temperature, dissolved material, and suspended matter. Water density in lakes is important because it controls sediment plume depth, and the amount of energy needed to mix the water column, which in turn affect how sediment is deposited. Sediment plumes that plunge along the lake bottom can form density driven currents that can aid in the formation of annual layers (Gilbert et al., 1997), oxygenate bottom waters, and limit sediment deposition to delta-proximal areas or the deepest portions of the lake (Lamoureux and Gilbert, 2004). Alternatively, sediment plumes in the upper or mid portion of a lake tend to produce aerially extensive deposits that drape the lake bottom or even exit the lake without settling (Weirich, 1985). The stability of a water column is important because it affects the ability of lower and upper portions of the water column to mix, controlling the bottom water oxygenation, nutrient and solute flux, and sedimentation.

Lake water density in the Canadian High Arctic has unique characteristics for two main reasons. First, *meromictic* lakes (lakes where recirculation does not affect the entire water body; Boehrer and Schultze, 2008) can have extraordinarily high dissolved loads. For example, mean salinity of ocean water is about 35 PSU, and depending on the temperature of the water, this represents 27-28 g/L of dissolved ions. However, hypersaline meromictic lakes in the Canadian High Arctic have dissolved loads that increase water density by up to about 80 g/L. Second, water temperature in many Canadian High Arctic lakes and their tributaries often straddle the

temperature of maximum water density, 4 ^{o}C. Cooling *and* warming from 4 ^{o}C reduces water density. Therefore, in freshwater lakes, the interactions between the density of lake water and stream water are extremely important and dynamic, and can determine where the streamwater flows through the lake water column.

This discussion begins with a review of the types of subaqueous sediment density flows. The majority of pioneering and ongoing research on these flows is from the marine environment, and this work is briefly reviewed. Next, the characteristics of sediment density flows in high arctic lakes are described, both for circulating and meromictic lakes. To facilitate the discussion, water profile data of temperature, specific conductance, density, dissolved oxygen, and Brunt-Väisälä frequency are illustrated for a group of lakes in the High Arctic.

2.1.2 Methods

Profiles of water temperature, specific conductance, and oxygen were obtained for 12 lakes in the Canadian High Arctic (Figures 2.1, 2.2, 2.3; Table 2.1). Where original data were not available, published profiles were digitized. All data were interpolated to one meter vertical resolution using a cubic spline. Salinity (PSU) was calculated by constructing a polynomial best-fit relation with specific conductance using the online calculator at *http://www.es.flinders.edu.au/~mattom/Utilities/salcon.html*, assuming a pressure of 2 dbar (about 20 m). The practical salinity scale is only strictly valid for salinities between 2 and 42 PSU, and many high arctic lakes have dissolved loads below and above this range. However, limited studies of fresh and hypersaline lake water in the Canadian High Arctic show that the ionic ratios of these waters are very similar to seawater, justifying the cautious use of the practical salinity scale above and below the range it was designed for (Ouellet et al., 1989). This assumption is not valid for lakes that have undergone significant evaporative enrichment, chemical weathering, salt

precipitation, or where biological activity has significantly altered ionic ratios relative to seawater (ex. Doran et al., 1994).

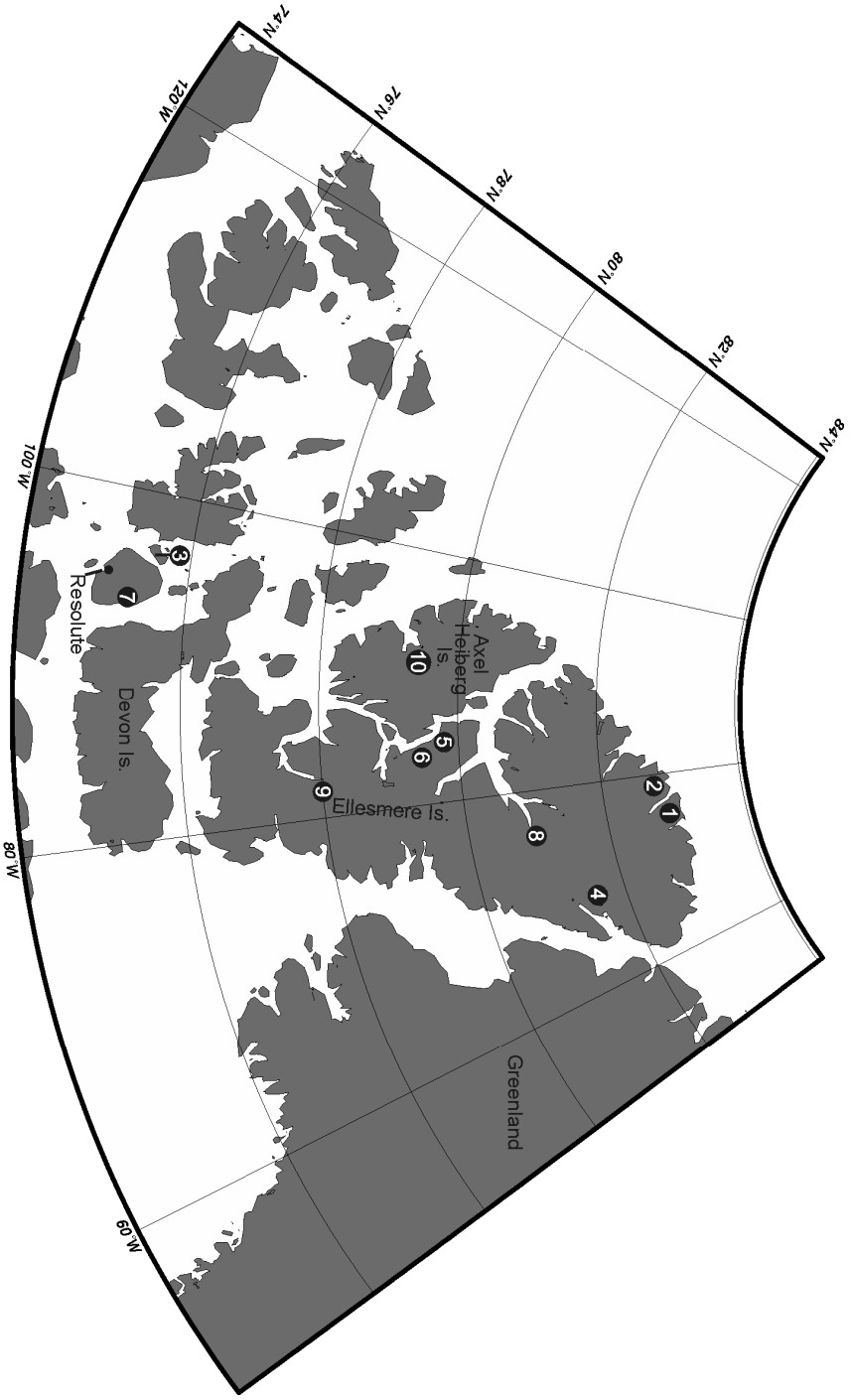

Figure 2.1. Location of the lakes discussed in Chapter 2. 1: Lakes A and B. 2: Lakes C1, C2, C3. 3: Garrow Lake. 4: Upper and Lower Murray Lakes. 5: Romulus Lake. 6: Sawtooth Lake. 7: Sophia Lake. 8: Lake Tuborg. 9: McMaster Lake. 10: Ice-dammed lakes studied by Maag, 1969.

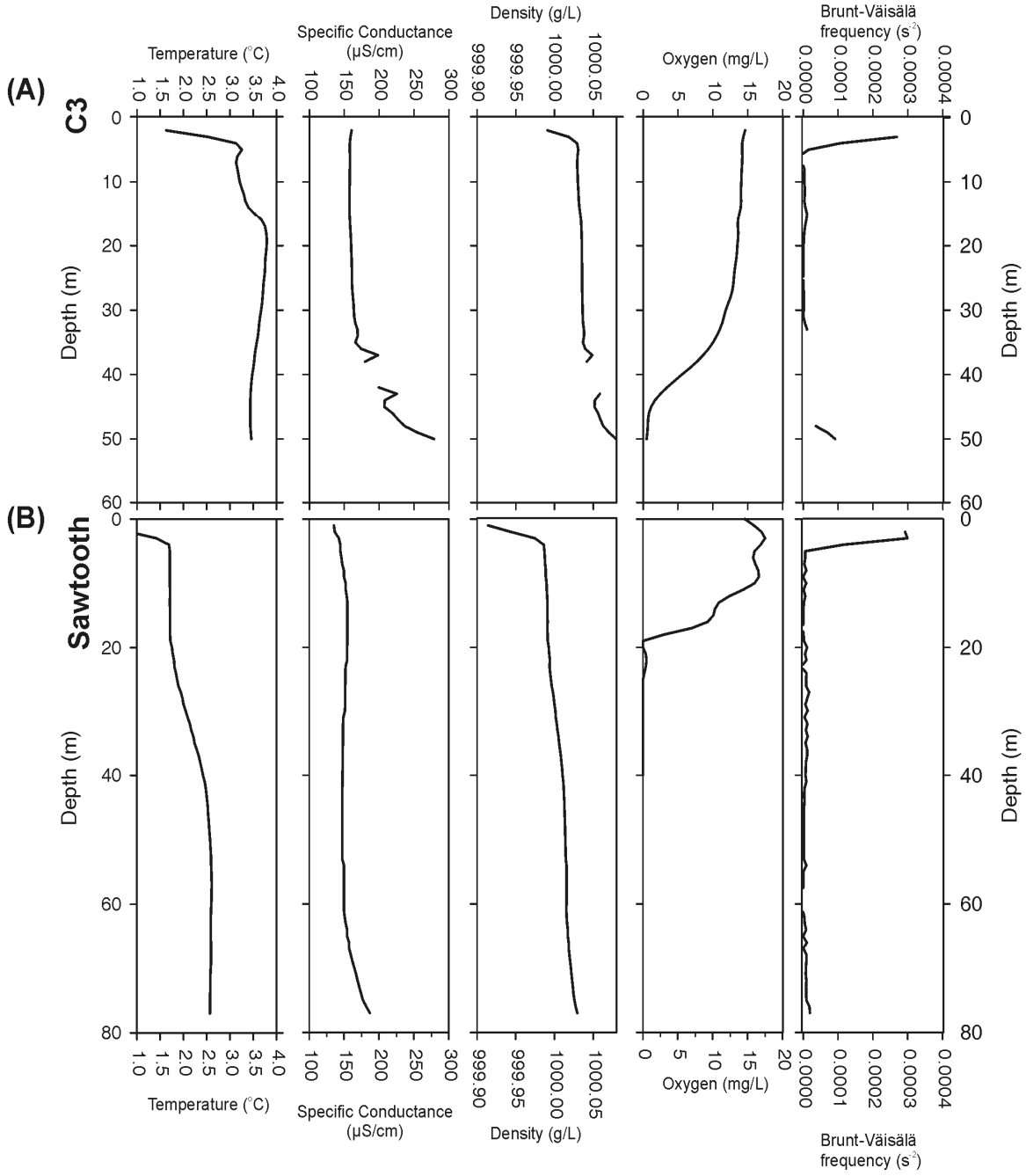

Figure 2.2. Water column profiles for 12 high arctic lakes showing temperature, specific conductance (SpC), density, dissolved oxygen, and Brunt-Väisälä frequency.

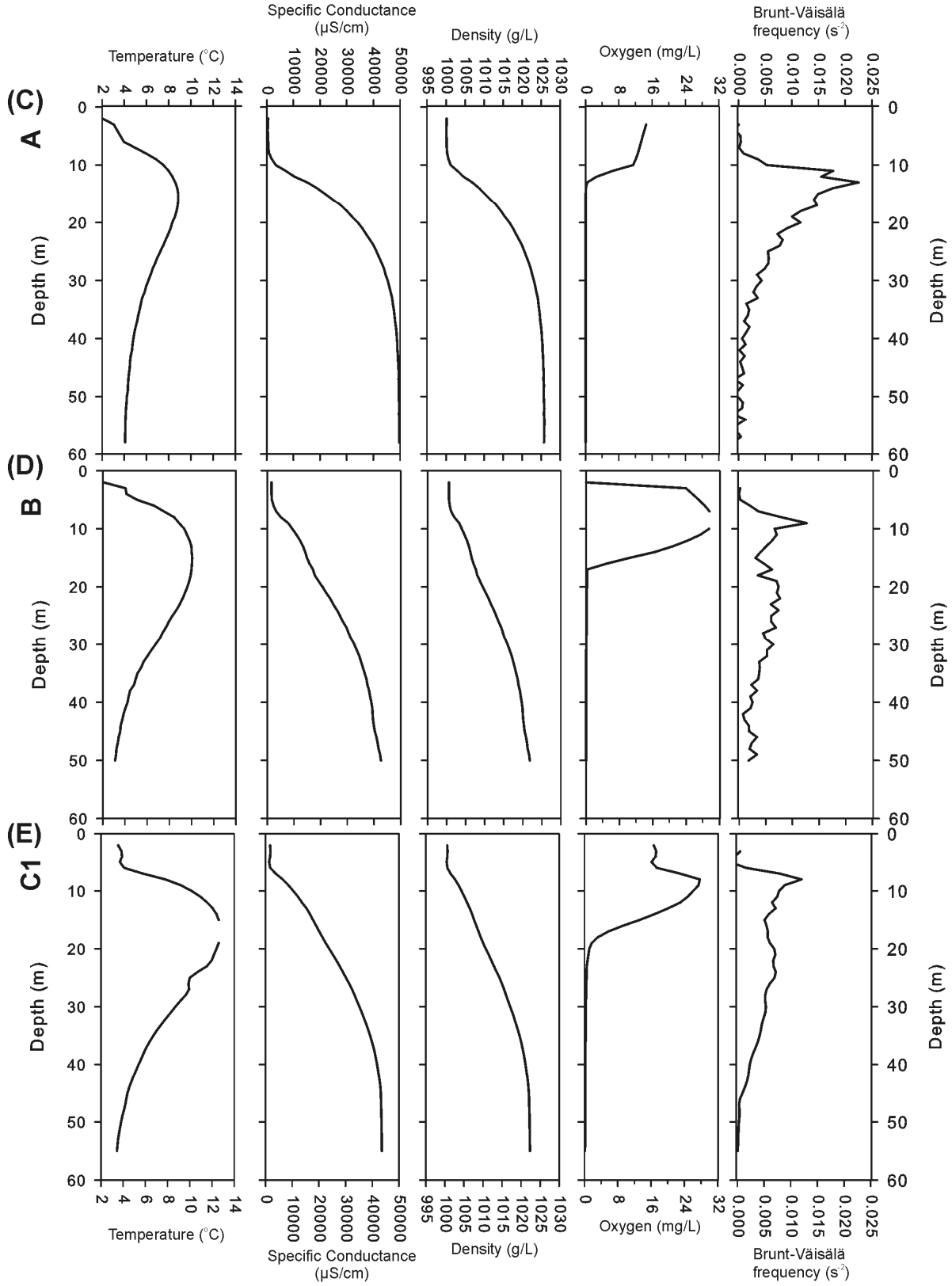

Fig. 2.2 Continued

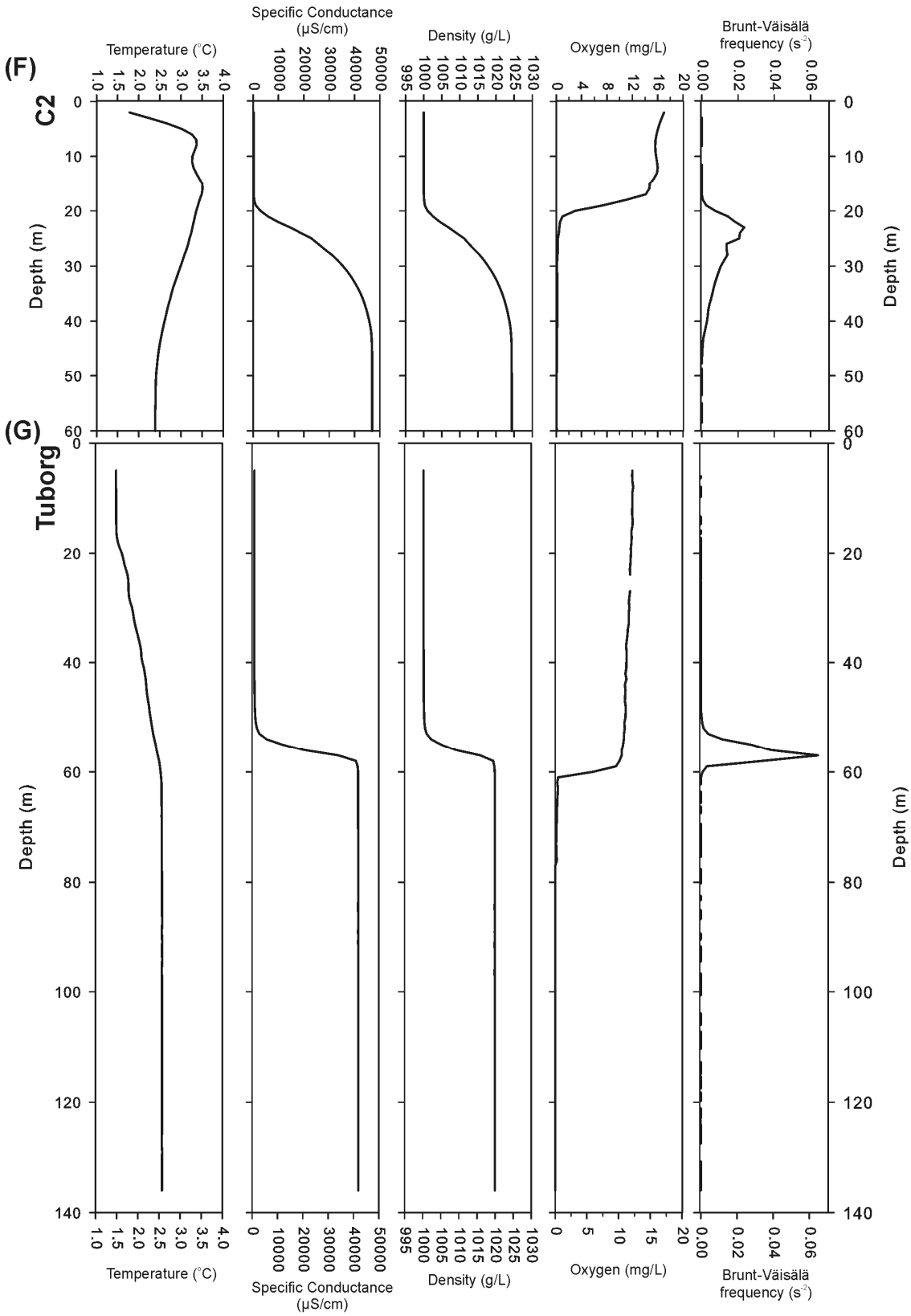

Fig. 2.2 Continued

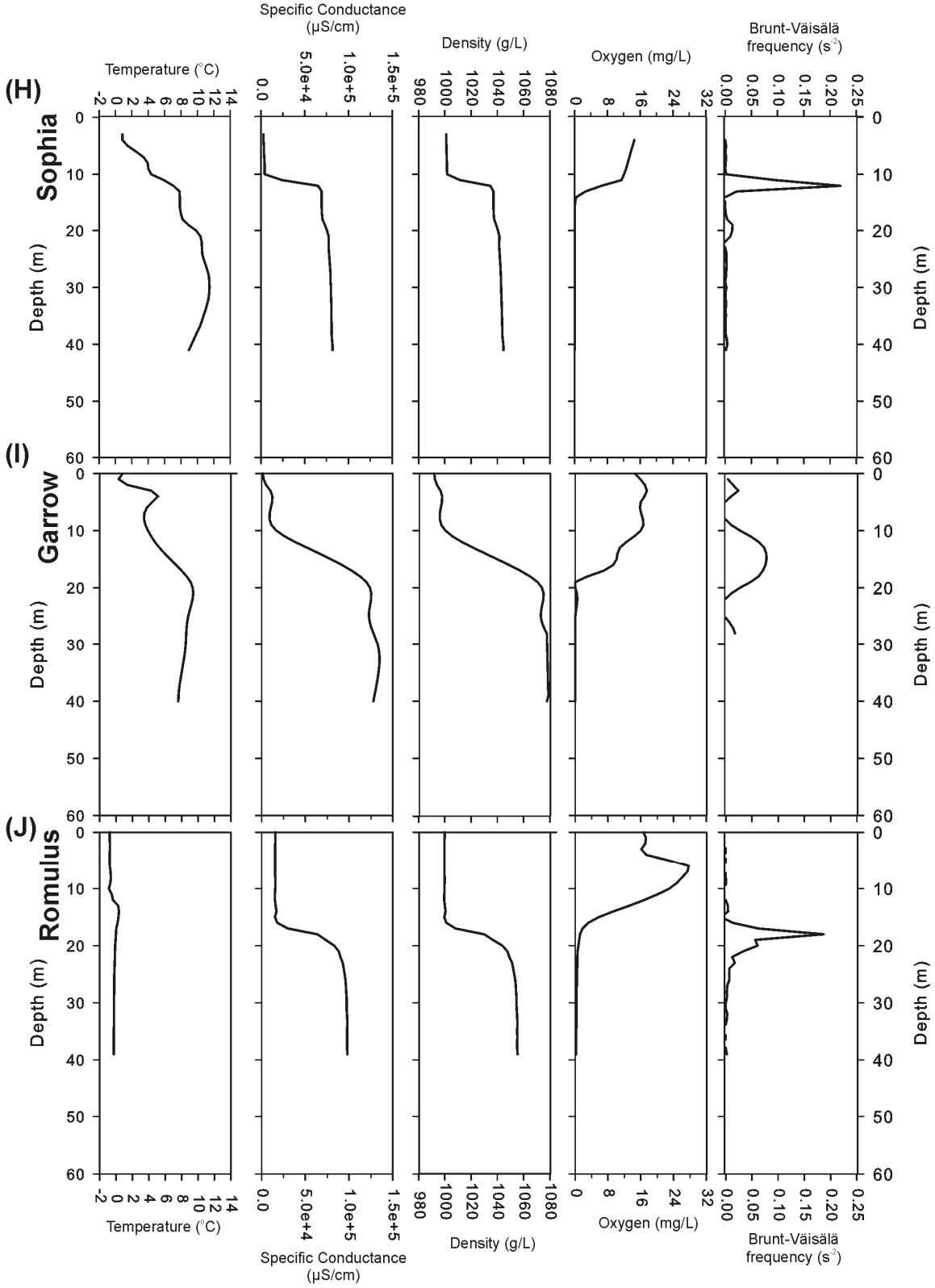

Fig. 2.2 Continued

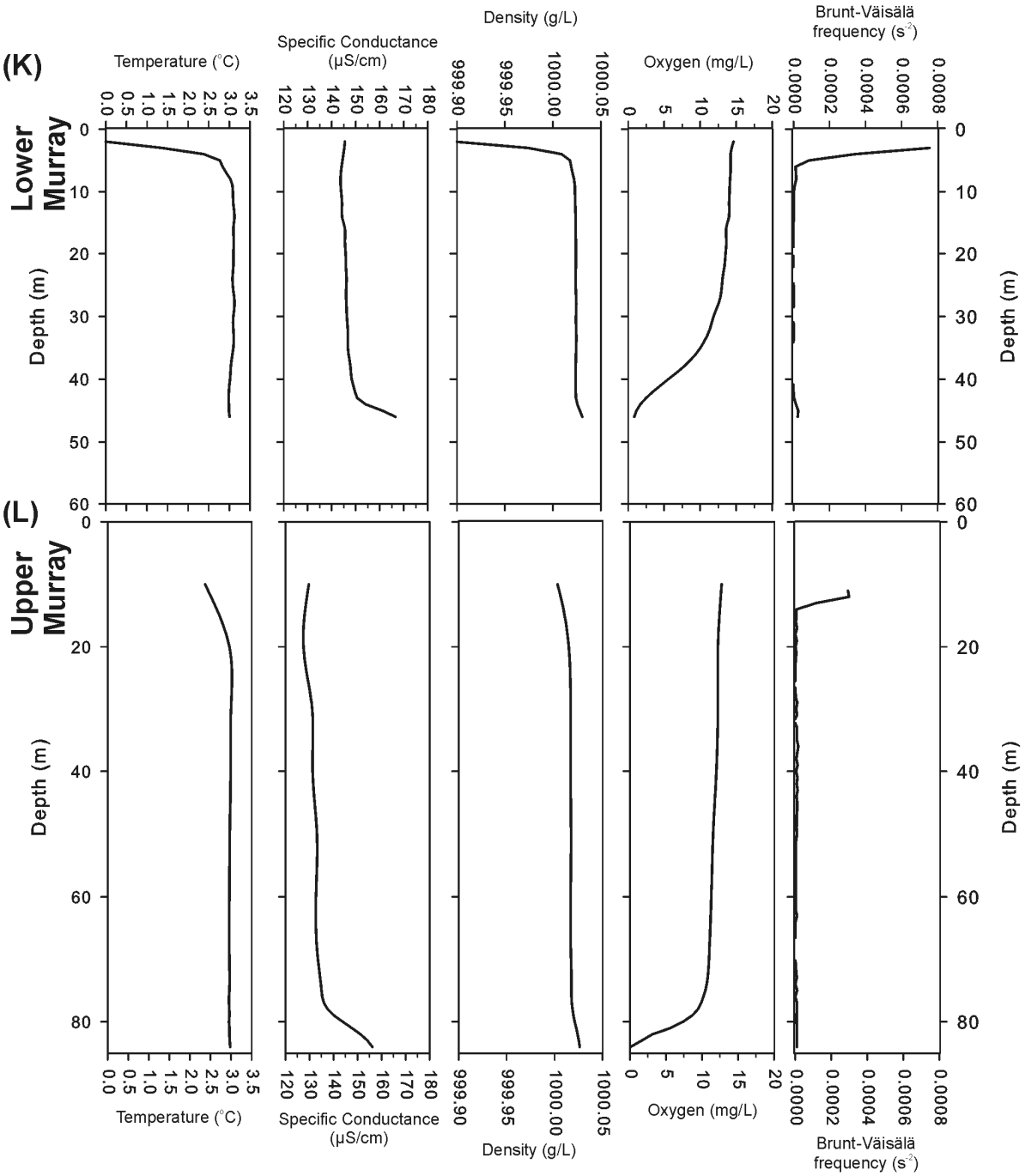

Fig. 2.2 Continued

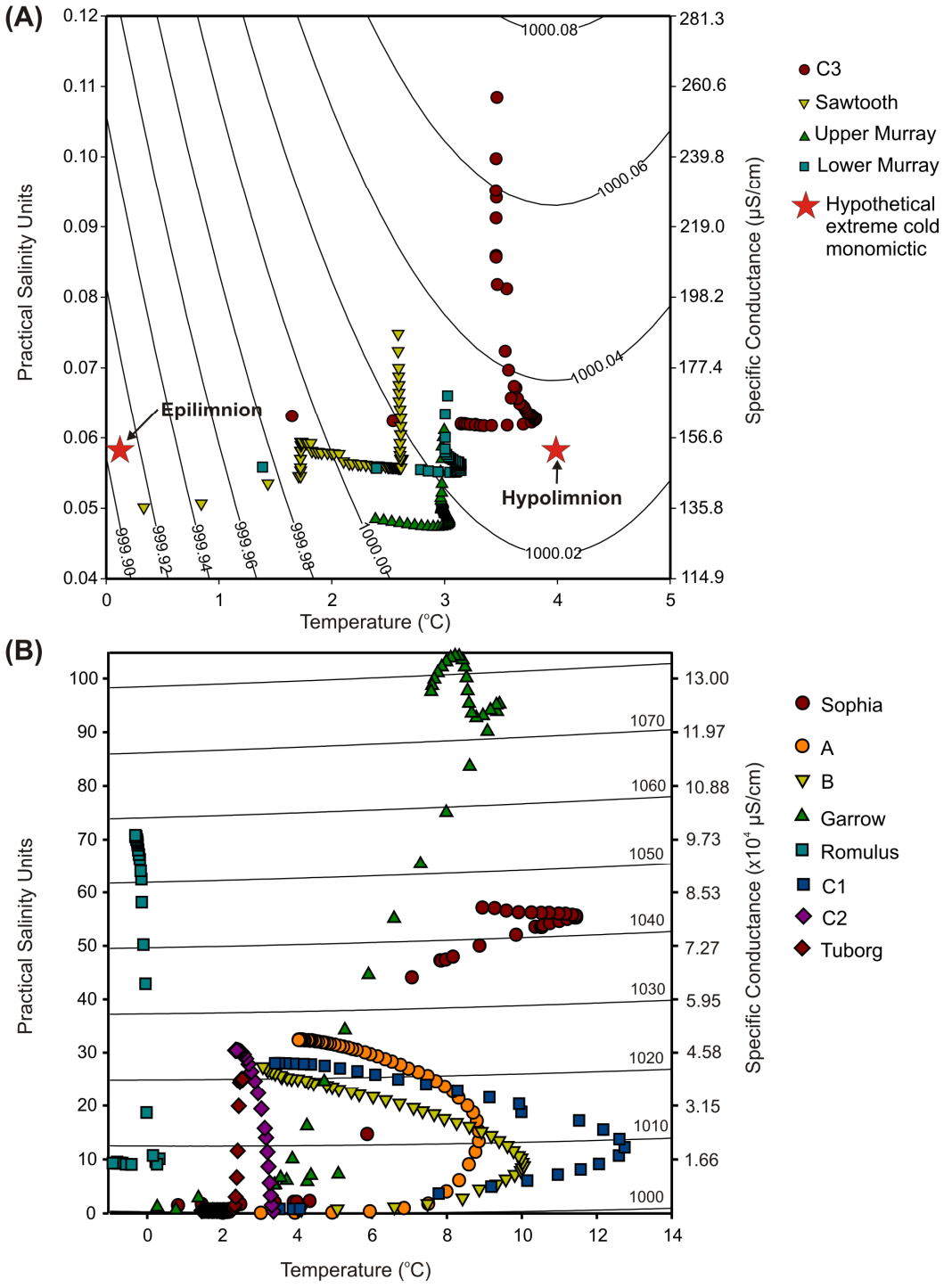

Figure 2.3. (A) Temperature, specific conductance and density for arctic freshwater lakes. (B) Temperature, specific conductance, salinity, and density for arctic meromictic lakes. Isopycnals are density in g/L (or kg/m^3).

Potential density was determined using salinity, temperature, and depth with the seawater equation of state (EOS-80) in the software *Ocean Data View* (Schlitzer, 2005). If ionic ratios differ from those of seawater, the calculated salinity, and hence density, will be imprecise. However, density *differences* in a given lake should be correct (Ludlam, 1996), so density differences rather than absolute densities are noted here wherever possible. Brunt-Väisälä frequency (N^2) is a measure of density stratification and resistance to mixing, where $N^2=(g/\rho)\cdot d\rho/dz$ (g is 9.83 m/s^2, ρ is density, z is depth; Wüest and Lorke 2003), and is calculated with 1 m depth bins.

Table 2.1. The twelve High Arctic lakes discussed in Section 2.1.

Lake	Coordinates	Stratification	Date	Source
A	83.00°N, 75.50°W	Meromictic	5/1993	Ludlam, 1996
B	~83.00°N, ~75.50°W	Meromictic	5/1993	Ludlam, 1996
C1	82.85°N, 78.20°W	Meromictic	5/2005	Unpublished
C2	82.83°N, 75.13°W	Meromictic	5/2005	Unpublished
C3	82.80°N, 78.08°W	Cold-monomictic	5/2005	Unpublished
Garrow	75.38°N, 96.83°W	Hypersaline	8/1980	Ouellet et al., 1989
Murray (Upper)	81.3°N 69.5°W	Cold-monomictic	6/2005	Besonen et al., 2008
Murray (Lower)	81.4°N 69.7°W	Cold-monomictic	6/2005	Besonen et al., 2008
Romulus	79.83°N, 85.00°W	Hypersaline	5/2000	Van Hove et al., 2006
Sawtooth	79.30°N, 83.90°W	Cold-monomictic	06/2000; 08/2006	Francus et al., 2008
Sophia	75.10°N, 93.62°W	Hypersaline	6/1993	Ludlam, 1996
Tuborg	80.95°N, 75.80°W	Meromictic	6/2001; 6/2003	Lewis et al., 2007

2.1.3 Types of subaqueous sediment density flows

Four types of flows have been identified based on their position within the water column: hypopycnal (*syn.* overflow), mesopycnal (interflow), hyperpycnal (underflow), and homopycnal flow (Smith and Ashley, 1985, Mulder and Alexander, 2001, Fig. 2.4). In a hypopycnal flow, the flow density (ρ_f) is less than the ambient water (ρ_w), and sediment flows buoyantly at the surface. In a mesopycnal flow, a density gradient (pycnocline) exists partway through the water column, as occurs in thermally and chemically stratified lakes, and the flow moves along the pycnocline. In a hyperpycnal flow, the sediment plume is negatively buoyant ($\rho_f > \rho_w$), and in a homopycnal flow $\rho_f = \rho_w$ (Fig. 2.4). By definition, these terms refer only to turbulent flows generated by suspended material in water that is initially riverine, so a slump or delta failure cannot create a hyperpycnal flow (Mulder et al., 2003).

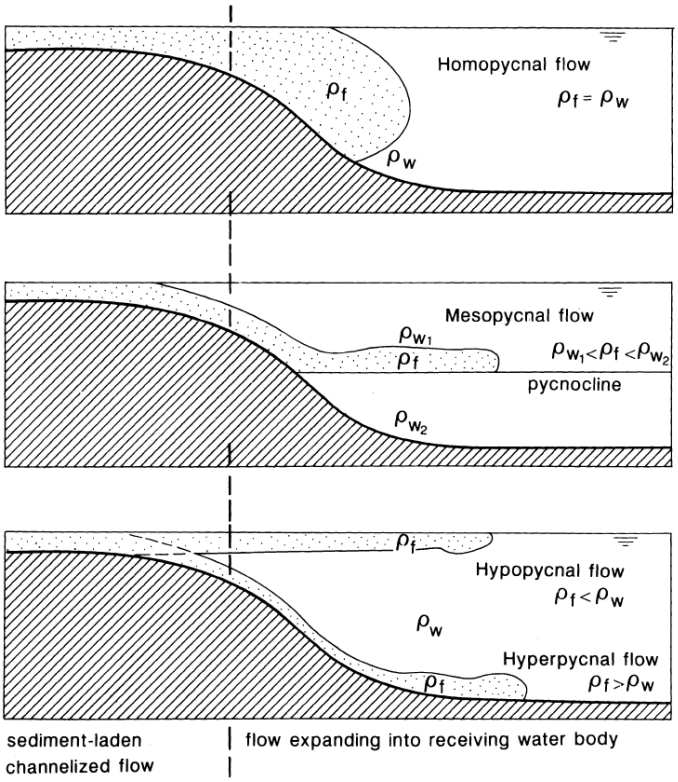

Figure 2.4. The four types of subaqueous density flows. ρ_f= flow density, ρ_w= ambient water density (Mulder and Alexander, 2001).

Hyperpycnal flows in the marine environment have received much study because their deposits are important oil and gas reservoirs, and they have the potential to destroy undersea pipelines and cables. For paleoenvironmental researchers, hyperpycnal flows are important because they can transport large volumes of sediment from nearshore areas into the deepest part of a basin, overwhelming typical annual mass accumulation rates in hours to days. They can also produce unconformities by eroding underlying sediments, and transport oxygen and nutrients to areas that are normally anoxic and nutrient limited.

A continuum of hyperpycnal flow types have been defined based on their sediment concentration, which affects flow velocity, particle support mechanism, and deposit thickness. Briefly, hyperpycnal flows with extremely high concentrations of sediment (about 35-85%) can flow as a cohesive non-Newtonian fluid, they do not mix with ambient fluid, and they are termed subaqueous mud flows or debris flows (Mulder and Alexander, 2001). Hyperpycnal flows with lower sediment concentrations move non-cohesively, and are termed hyperconcentrated density flows, concentrated density flows, and turbidity currents. Confusingly, turbidites are not just the deposits from turbidity currents. Deposits from all types of hyperpycnal flows have been called turbidites in the literature (Mulder and Alexander, 2001).

Turbidity currents are flows where sediment is suspended by fluid turbulence, and can form when sediment concentrations are <9% by volume. They have three main components: a head, a body, and a tail (Fig. 2.5; Boggs, 1987). Turbulence is intense in the head, and coarser grains are concentrated there. The head can erode and suspend underlying sediments, which replaces sediment lost to settling in the body, and maintains the density surplus of the current. Turbidity currents are subdivided based on their duration into surges that last seconds to minutes, and quasi-steady flows. Surge-type currents are likely rare, and would only occur where sediment supply is limited (Mulder and Alexander, 2001). Their deposits are typically thin and dominated by the head, since their tails are short. Quasi-steady flows often form from sediment laden river

inflow (Parsons et al., 2007). Their deposits tend to be thicker and are dominated by the body and tail (Mulder and Alexander, 2001).

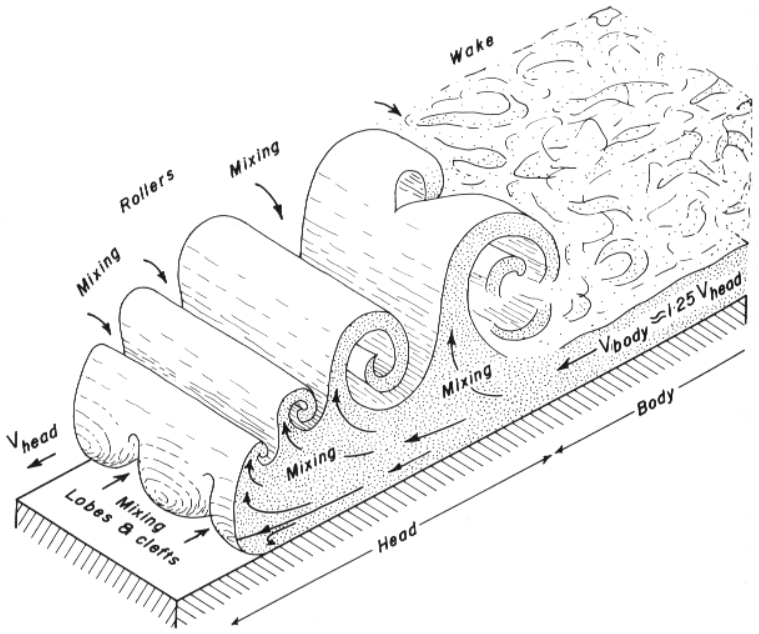

Figure 2.5. The head and body of a turbidity current (Boggs, 1987).

Quasi-steady turbidity currents slow and stop when the density difference between the head and the ambient fluid decreases, the slope they flow over diminishes (turbidity currents can flow in slopes as low as 1^{o}), or the head spreads. Alternatively, surge currents are not affected by bottom slope (Boggs, 1987). Turbulence in the head is eventually unable to maintain its density surplus relative to ambient water, and the surface of the head convects, or its base lofts off the floor of the basin.

Hyperpycnal flows initially contain fresh riverine water with a density of about 1000 g/L, not including density contributed through suspended sediment. It has long been recognized that for a hyperpycnal flow to form, the density of seawater (1024.34 g/L at 35.75 ‰ and 24^{o}C) must be exceeded by freshwater containing extremely large amounts of suspended sediment (24.34 g/L in this example). Such high densities of suspended particulate matter are very rare globally. Gilbert (2000) states that suspended sediment concentrations "*up to about 10 g/L are commonly*

reported in the literature". In a study of 150 small, medium, and large rivers flowing into the ocean worldwide, it was estimated that only nine were capable of producing hyperpycnal flows annually (Mulder and Syvitski, 1995). Hyperpycnal flows would therefore only be produced during extreme events like lahars, reworking of fine-grained sediment, floods from large active glaciers, jökulhlaups (catastrophic drainage of an ice-dammed lake), or extreme precipitation events (Gilbert, 2000; Mulder et al., 2003). The large difference in density between freshwater and saltwater also means that when hyperpycnal plumes do form in the ocean, they tend to have short run-out distances, loft off the bed early, and transform into buoyant flows (Rimoldi et al., 1996). Sediment that is not transported by hyperpycnal flow is advected by buoyant plumes, and in the marine environment these tend to either be scavenged early by saltwater flocculation, or transported close to the coast by longshore currents.

Somewhat paradoxically, very large rivers are unlikely to produce hyperpycnal flows with high return periods, because high discharge dilutes suspended particulate matter, and the large deltas that larger rivers build are sediment sinks (Mulder et al., 2003). For example, the Mississippi River can never produce hyperpycnal flows (Mulder and Syvitski, 1995). Of the nine rivers identified as being capable of producing hyperpycnal flows, eight were 'small and undersized', and eight had catchments with maximum elevations greater than 1000 m (Mulder and Syvitski, 1995). These small mountainous catchments have fewer sediment sinks than larger rivers, and have steep slopes, so they are prone to short but extreme sediment transfer events, for example during precipitation events (Milliman and Syvitski, 1992).

This is significant for paleolimnologists because small systems have frequently been targeted for sediment-based climatic reconstructions (ex. Zolitschka, 1996; Lamoureux, 2000; Francus et al., 2002; Besonen et al., 2008), since they have relatively simple hydrologic and sedimentary inputs that can be more easily linked to changes in weather and climate.

The classic interpretation of hyperpycnal flows only occurring when the density of the flow exceeds the ambient water density has been challenged and updated (Rimoldi et al., 1996; Hoyal et al., 1999; McLeod et al., 1999; Parsons et al., 2001; McCool and Parsons, 2004). Observations in density stratified flumes have led to the discovery of a process called convective circulation. Experiments where sediment plumes overlie denser water produce 'fingering' and 'leaking', where thin plumes of sediment are removed from the surface layer and extend into the deeper layer (Fig. 2.6). Convective circulation can create a 'divergent plume', where a buoyant plume with a much lower density than the underlying water creates a hyperpycnal flow (Fig. 2.6). In the absence of turbulence, convective circulation can occur at an interface with 1 g/L density difference (Parsons et al., 2001), and with turbulence the difference can be as little as 0.38 g/L (Parsons et al., 2007). Lowering the density threshold to 1 g/L increases the number of rivers worldwide that are capable of producing annual hyperpycnal flows from nine to 61 out of 150 (Parsons et al., 2001; Mulder et al., 2003).

2.1.4 Density in arctic freshwater lakes

From the above discussion, it is evident that hyperpycnal flows should be much more common in freshwater lakes than in meromictic lakes or in the ocean, since inflowing river water usually has a similar dissolved load to the ambient lake water, and the suspended load in inflowing rivers is often higher than the lake. This is particularly true for small mountainous lakes with small rugged watersheds that are often targeted by paleolimnologists. Indeed, hyperpycnal flows were first described in freshwater lakes (Lake Geneva, and later in Lake Mead; Mulder et al., 2003). Much subsequent research has thoroughly identified lacustrine hyperpycnal flows and characterized their deposits (Gilbert, 1975; Pharo and Carmack, 1979; Gilbert and Shaw, 1981; Weirich, 1986; Lambert and Giovanoli, 1988).

Density differences in freshwater lakes are driven by changes in temperature rather than dissolved load. The seasonal changes in river water relative to lake water were thoroughly described for a large temperate lake in British Columbia (Carmack, 1979; Carmack et al., 1979; Fig. 2.7).

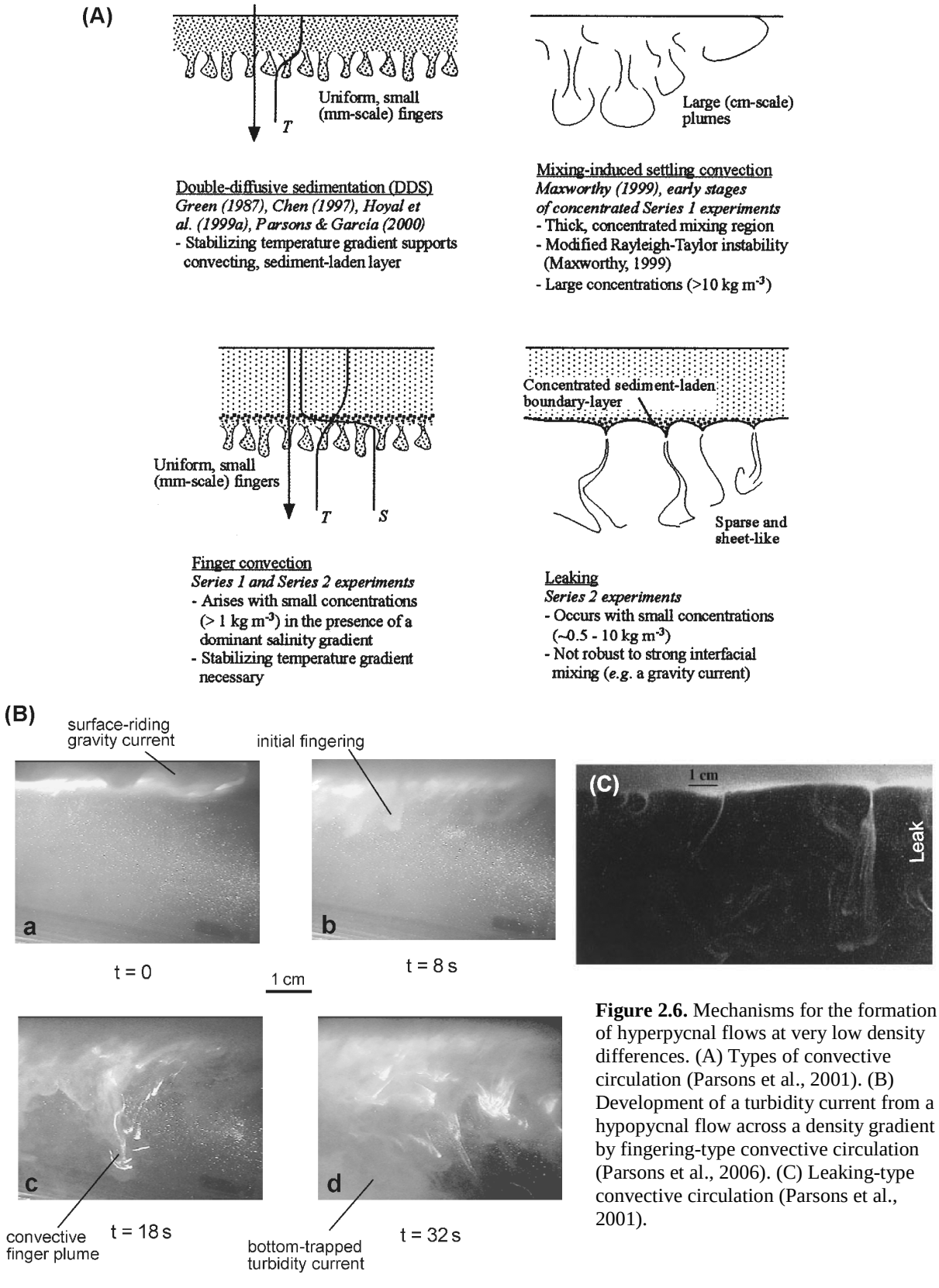

Figure 2.6. Mechanisms for the formation of hyperpycnal flows at very low density differences. (A) Types of convective circulation (Parsons et al., 2001). (B) Development of a turbidity current from a hypopycnal flow across a density gradient by fingering-type convective circulation (Parsons et al., 2006). (C) Leaking-type convective circulation (Parsons et al., 2001).

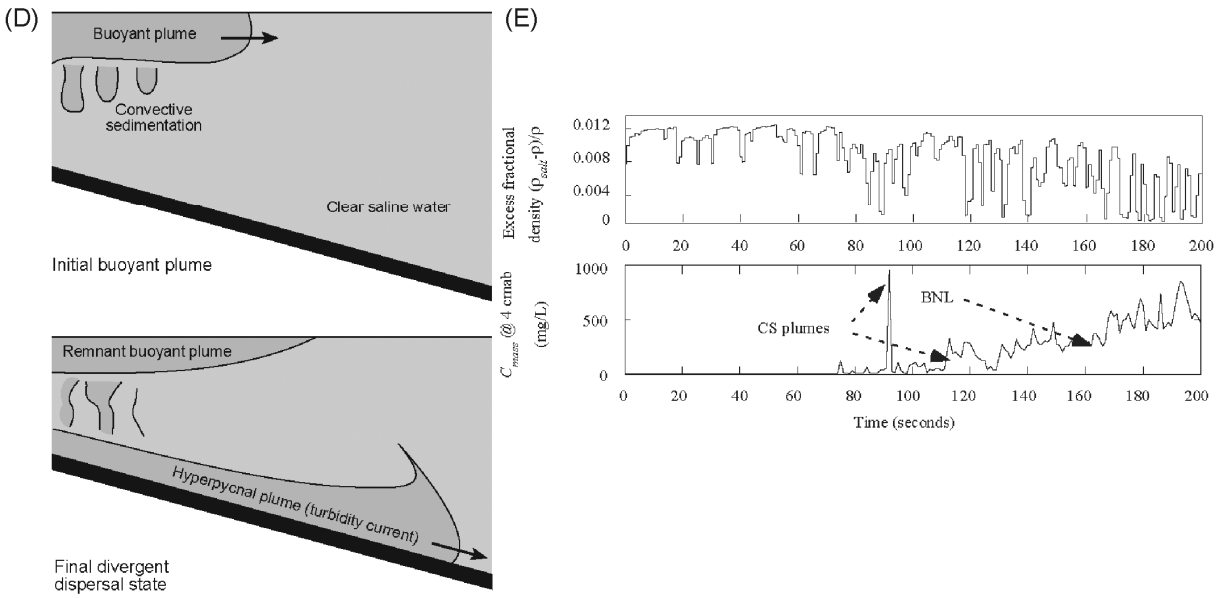

Figure 2.6 (continued). (D) Schematic diagram of the development of a divergent turbidity current from a hyperpycnal flow (Parsons et al., 2006). (E) Flume results of the development of a bottom nepheloid layer (BNL) being fed by convective circulation plumes. The top panel shows the progressive decrease in density of the upper water column relative to the bottom of the tank. The lower panel shows the progressive increase in particulate concentration at the bottom of the tank (McCool and Parsons, 2004).

In the High Arctic, temperature, and hence density differences between the upper portion of the water column (epilimnion), and the lower part (hypolimnion) are much less than in temperate dimictic lakes. Arctic lakes are usually either cold monomictic (warms to 4^{o}C for a brief period during summer) or amictic (does not circulate). A hypothetical 'extreme cold-monomictic' lake is considered here, where the epilimnion is 0.1 ^{o}C, and the hypolimnion is 4 ^{o}C (Fig. 2.8). This creates a thermally-derived density difference between the epilimnion and hypolimnion of about 0.12 g/L (Figs. 2.3A, 2.8). Density differences would be very much less for an amictic lake where vertical temperature changes are necessarily very small. Even in the extreme hypothetical cold-monomictic example, it appears that fluvially-derived suspended sediment could easily overcome the 0.12 g/L density difference in both glaciated and snowmelt-fed systems, before, during and after the period of peak river flow (Lewkowicz and Wolfe, 1994; Hardy, 1996; Braun et al., 2000a; Gilbert, 2000; Cockburn and Lamoureux, 2008). Indeed, this extreme hypothetical example is unlikely to occur naturally, except where the epilimnion is in

contact with glacial ice, in which case the hypolimnion would be unlikely to reach 4 °C, and the lake would more likely be amictic and isopycnal (Maag, 1969; Gilbert, 1971). Profiles from high arctic freshwater lakes show much lower thermally-derived density differences (Fig. 2.2 A, B, K, L), allowing fluvially-derived suspended sediment to very easily form hyperpycnal flows.

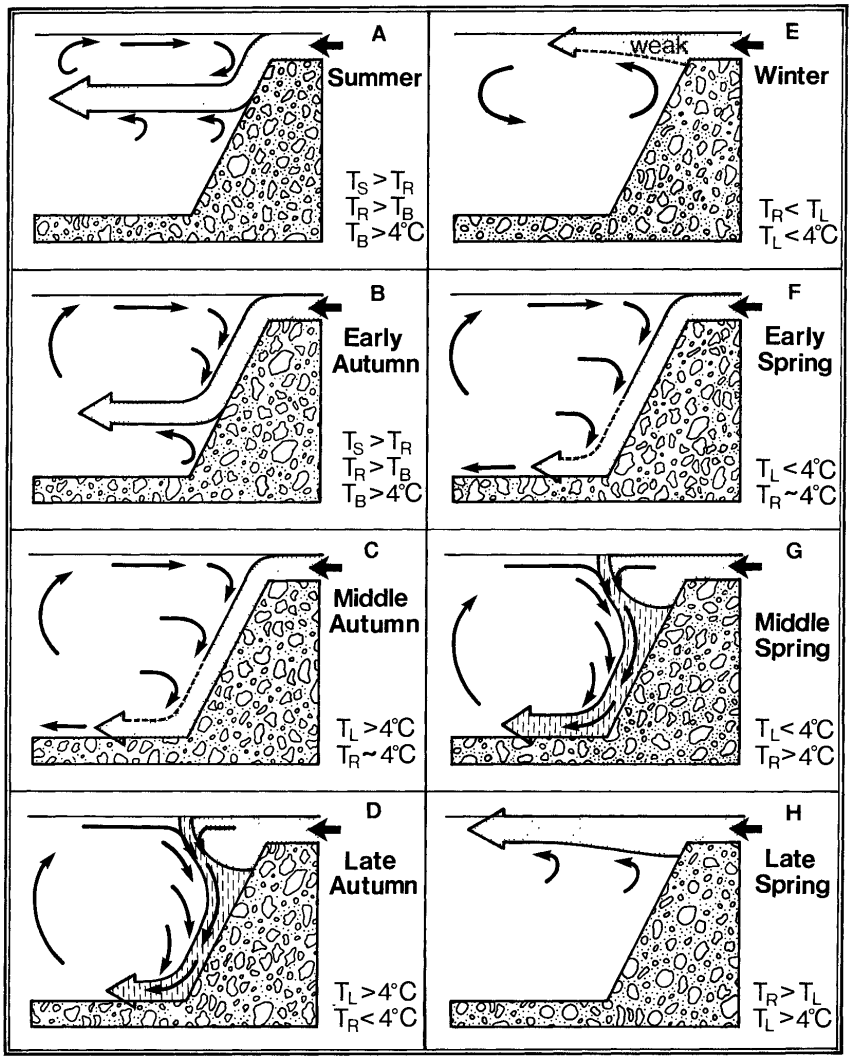

Figure 2.7. River-induced circulation changes over a year in a dimictic temperate lake illustrating the seasonally-changing effects of the interaction between river water temperature (T_R) and lake water temperature (T_L). In 'A', during summer, inflowing water is colder and more dense than lake surface water (T_s), but warmer and less dense than lake bottom water (T_B), so interflows form. In 'B-D' autumn cooling progressively cools inflowing river water, until it approaches 4 °C ('C'), and can plunge along the warmer lake bottom as a hyperpycnal flow. In 'E', in winter, low flows of cold, low density river water flows into the warmer, denser lake water, and overflows form. Underflows can form again in 'G' when dense inflowing water is warmer than 4 °C, and the lake water remains cooler than 4 °C. As the lake warms past 4 °C, inflowing water is again warmer and less dense than the lake water, and overflows form in 'H' (Carmack et al., 1979).

Cooling of the upper part of the epilimnion by lake ice is often the largest contributor to density differences in arctic lakes (ex. Fig. 2.2A, B, K). This helps explain why overflows are often recorded early in the melt season when the ice cover is thick. For example, at Lower Murray Lake, the wholly thermally derived density decrease in the upper three meters of the water column is responsible for more than 0.1 g/L density differences (Fig. 2.2K). As previously noted, this is small in relation to fluvial suspended sediment concentrations in medium-sized arctic rivers. However, it should be noted that suspended sediment often settles close to the point of inflow, and lacustrine plumes exceeding 100 mg/L appear to be uncommon in arctic lakes (Retelle and Child, 1996; Lewis et al., 2007; Francus et al., 2008).

Thermally-derived density differences in the upper epilimnion are important because they can occur during times of peak river flow and sediment transport, and tend to force sediment plumes into the upper water column at these times (Francus et al., 2008). Near-surface density differences tend to disappear later in the melt season when the ice cover breaks up, or perhaps when riverine-generated mixing of the water column occurs. This probably makes hyperpycnal flows more common later in the melt season, despite reduced fluvial suspended particulate matter and sediment flux relative to times of peak flow.

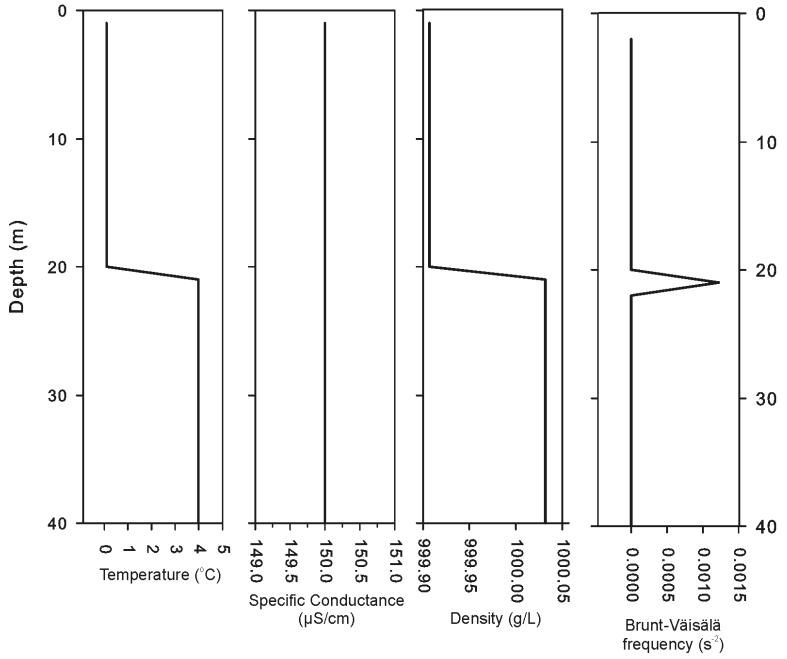

Figure 2.8. A CTD profile of a hypothetical cold-monomictic lake with the largest possible density difference between hypolimnion and epilimnion, and the largest possible resistance to mixing from an extremely abrupt pycnocline.

Thus far, changes in conductivity as a control on density in freshwater arctic lakes have not been considered. Near-bottom conductivity increases have been recorded in the deepest portions of all freshwater lakes where data are available: Lake C3 (Fig. 2.2A), Sawtooth Lake (Fig. 2.2B), and Upper and Lower Murray Lakes (Fig. 2.2K, L). Where lakes are below marine limit, these near bottom conductivity increases might reflect remnant salinity from when the lakes were meromictic (the origin of meromictic lakes is discussed in Section 2.1.5). In other cases, the phenomenon might be ongoing, and might be caused by annual exclusion of salts from the lake ice (Stewart and Platford, 1986), the surrounding land (Pagé et al., 1984; Ouellet et al., 1989), or mobilization of ions in lake sediments in anoxic conditions (Francus et al., 2008). Based on the freshwater lake profiles obtained thus far, near-bottom conductivity increases affect density and stability to a lesser extent than thermally-derived density changes (Fig. 2.3A). For example, Lake C3 has the largest near-bottom conductivity increase of any freshwater high arctic lake studied

thus far, but this increase is responsible for only a 0.03 g/L density difference between the epilimnion and hypolimnion (Figs.2.2A, 2.3A). The cooling of the upper epilimnion creates a Brunt-Väisälä frequency peak that is three times greater than the Brunt-Väisälä frequency peak created by the near-bottom conductivity increase (Fig. 2.2A). Interestingly, part of the low sensitivity of density to salinity at Lake C3 is because much of its water column is close to 4 ^{o}C. A similar salinity increase at lower temperatures would create a much larger density increase (Fig. 2.3A). Whatever the origin of near-bottom conductivity increases, they likely exist as a continuum between entirely freshwater lakes and meromictic lakes. There are likely to be many lakes with much higher near-bottom conductivity increases that have yet to be profiled. These would impart much more important density differences.

Although the near-bottom conductivity increases recorded to date do not greatly affect density and Brunt-Väisälä frequency, they appear to sufficiently resist mixing, so that localized stagnant zones are created at the deepest portions of the lakes. These stagnant pools are very low in dissolved oxygen, can prevent bioturbation, and finely laminated sediment archives can be preserved in these areas (Francus et al., 2008). In some cases, these near-bottom conductivity increases are eroded throughout a melt season, presumably by hyperpycnal flows (Lamoureux, personal communication, 2008). Their ease of erosion is understandable given the relatively low density and resistance to mixing they provide (Figs. 2.2, 2.3A). Given the importance of near-bottom conductivity increases to preserving a laminated sediment record, they clearly deserve more detailed study.

2.1.5 Density in arctic meromictic lakes

Comparison of the temperature and specific conductance axes, and isopycnals, of Figures 2.3A and 2.3B illustrates the immense physical differences between lakes in very similar climatic,

geomorphic, and topographic regions (Fig. 2.1). Arctic meromictic lakes can be extremely warm (up to +13 ^{o}C; Figs. 2, 3B), in a region where mean annual temperature is about -20 ^{o}C. This has been explained as trapping of solar energy in saline, stagnant bottom waters (Ludlam, 1996; Van Hove et al., 2006). Also, several meromictic lakes are hypersaline, with salinities much greater than seawater (>34.7 PSU; Fig. 2.3B).

A brief discussion of the types of meromictic lakes is necessary. *Ectogenic* meromixis occurs where an external process brings saltwater to a lake and acts for a limited time. For example, Lake Tuborg is an ectogenic meromictic lake, because a glacier isolated it from the sea (Hattersley-Smith and Serson, 1964), as are Lakes C1 and C2, because isostatic uplift isolated them from the ocean (Bradley et al., 1996). *Crenogenic* meromixis occurs when denser water is continuously brought to a lake, as is the case with saltwater exclusion from lake ice and permafrost, and mineralized springs (Pagé et al., 1984; Stewart and Platford, 1986; Ouellet et al., 1989). Biogenic meromixis occurs where electrolytes concentrate due to the decomposition of organic material (Hutchinson, 1937). These three processes can interact in a single lake; for example, hypersaline Garrow and Sophia Lakes have been called ‘ecto-cryo-crenogenic ‘ (Ouellet et al., 1989). However, only crenogenic and biogenic processes are capable of producing hypersaline lakes.

Although changes in temperature can be very large in meromictic lakes, temperature has very little control over density when salinity is high (Fig. 2.3B). For example, the monimolimnion of Garrow Lake is about 80 g/L denser than fresh water in its epilimnion (Figs. 2.2I, 2.3B). Compare this with the 0.12 g/L density difference in the hypothetical cold-monomictic lake example (Fig. 2.8). Dense saline and hypersaline lake water makes it extremely difficult for sediment-laden hyperpycnal flows to form, for the same reason as discussed in Section 2.1.3 for rivers flowing into oceans. Thus, inflowing fresh river water should almost

always be restricted to the mixolimnion (the fresh water layer), and should rarely, if ever, interact with the monimolimnion (the salt water layer).

Large density differences between the monimolimnion and mixolimnion of meromictic lakes results in extremely strong resistance to mixing, which is always at least an order of magnitude greater than in cold-monomictic lakes (Table 2.2). However, resistance to mixing is not proportional to salinity. For example, Garrow Lake has a much lower peak Brunt-Väisälä frequency than both Sophia and Romulus Lakes, although it has a much more concentrated monimolimnion. Similarly, Lake Tuborg has a higher Brunt-Väisälä frequency than Lakes C1, C2, A, and B, although it is less saline than all these lakes (Table 2.2). This underscores the importance of the rate of change of salinity at the chemocline. Lakes with relatively sharp chemoclines like Lake Tuborg, Sophia Lake, and Romulus Lake can resist mixing to a greater extent than more saline lakes with more gradual chemoclines. Where chemoclines are shallow, and the lake ice cover breaks up, wind-generated mixing can make a sharp chemocline more gradual, and hence greatly lower the resistance to mixing.

The sensitivity and unique responses of meromictic lakes to climate change can be illustrated with two examples. First, warming air temperatures are shifting Lake A from a perennially ice-covered system to a system that experiences limited breakup. Wind-generated mixing during ice-free periods is making a sharp chemocline become more gradual (Van Hove et al., 2006). This would be a positive feedback, in that a gradual chemocline would lower the maximum Brunt-Väisälä frequency, and hasten the eventual evolution of the lake into a freshwater system. Alternatively, at Lake Tuborg, large jökulhlaups began occurring in the latter half of the 20th century, and these events were unique in at least the last millennium (Lewis et al., 2008). Sediment-laden jökulhlaup-derived currents move along the chemocline at about 55 m depth, and these currents make the chemocline extremely sharp and abrupt (Lewis et al., 2007). Jökulhlaups have been occurring sufficiently frequently that the very slow process of molecular

diffusion cannot create a gradual chemocline (Toth and Lerman, 1975), and mixing during infrequent breakup of the ice cover does not allow mixing as deep as 55 m. The sharp chemocline creates a strong resistance to mixing, and effectively armors the monimolimnion. Therefore, while CTD casts exist from Lake Tuborg since 1963 (Section 2.3.2), there has been remarkably little change in the salinity of the monimolimnion, particularly considering that this was a period of unprecedented jökulhlaup activity. This is a surprisingly contrary response to warming at Lake A.

Table 2.2. Ranked maximum Brunt-Väisälä frequency and maximum specific conductance in the 12 studied lakes and the hypothetical cold monomictic lake.

Lake	Brunt-Väisälä frequency (max)	Specific Conductance, µS/cm (max)	Stratification
Sophia	0.21992	81850	Meromictic and hypersaline
Romulus	0.18645	98180	Meromictic and hypersaline
Garrow	0.07792	134836	Meromictic and hypersaline
Tuborg	0.06481	41950	Meromictic
C2	0.02349	47023	Meromictic
A	0.02251	49830	Meromictic
B	0.01265	42642	Meromictic
C1	0.01203	43588	Meromictic
Hypothetical	0.00122	150	Cold-monomictic
Lower Murray	0.00076	167	Cold-monomictic
Sawtooth	0.00030	187	Cold-monomictic
C3	0.00027	279	Cold-monomictic
Upper Murray	0.00002	156	Cold-monomictic

It is hypothesized that the salinity of Lake Tuborg bottom waters dropped to near-current levels (~25 PSU) relatively early following marine isolation when comparatively little stratification existed, and resistance to mixing was relatively low.

In most cases, the chemocline in meromictic lakes coincides with a sharp oxycline because the density difference and high resistance to mixing isolates the monimolimnion from overlying fresh water (Fig. 2.2C, D, E, F, G, H, I, J). This might make meromictic lakes ideal targets for paleoenvironmental reconstruction because of the lack of influence from hyperpycnal flows and bioturbation in their monimolimnia. This is likely true for some ectogenic meromictic lakes. However, hypersaline crenogenic meromictic lakes are likely hypersaline because fluvial input has been unable to balance seasonal influxes of salts into the monimolimnion. This would only be the case in lakes with small watersheds with low total discharge and sediment flux, and this would either produce extremely thin varves, or prevent their formation altogether (Braun et al., 2000b; Van Hove et al., 2006).

2.1.6 Conclusions

Arctic freshwater lakes are likely affected by frequent hyperpycnal flows in the absence of lake-specific controls like sills that limit bottom currents to proximal basins, and exclude them from distal basins (Chikita et al., 1996; Lewis et al., 2002; Lewis et al., 2007; Francus et al., 2008). The increases in conductivity in the arctic freshwater lakes documented thus far create very small density increases and small Brunt-Väisälä frequencies, and may be seasonally transitory. However, these subtle features can be extremely important, since they have the potential to control the preservation of paleoenvironmentally important sediment records (Francus et al., 2008). The salinity of meromictic high arctic lakes is likely much more difficult to remove by hyperpycnal flows because of the large stability the salinity imparts. This is particularly true where large salinity gradients occur. Depending on their origin, evolution, and watershed characteristics, meromictic lakes may be more likely to possess undisturbed sediment archives. This also assumes that the lake watersheds do not experience floods capable of transporting

extreme loads of suspended particulate matter, as would occur in jökulhlaups. This is the subject of the following section.

2.2 Jökulhlaup hydrology, relation to glacier position, and distal sedimentary deposits

2.2.1 Introduction

Many papers have investigated jökulhlaup drainage mechanisms and triggers, hydrology, proximal sedimentary deposits, and relationships with climate. This review begins with a synthesis of this work with the goal of providing an understanding of jökulhlaup-derived processes and deposits in distal basins, both marine and lacustrine. There has been relatively little research with this focus, despite the potential for these basins to contain climatically-sensitive records of jökulhlaup activity. There are also very few studies of high arctic jökulhlaups, but results from these areas are highlighted wherever possible.

2.2.2 Jökulhlaup triggers

Drainage of ice-dammed lakes can be triggered by subglacial volcanic activity, seismic activity, overspill, flotation, siphoning, subareal breach widening, and hydrostatic pressure forcing a hole in the dam (the Glen mechanism). Subglacial volcanic activity is a common trigger in Iceland (Russell et al., 2006). No jökulhlaups are known to have been triggered by seismic activity (Tweed and Russell, 1999). In siphoning, lake water can interact with a pre-existing glacial drainage network, and a jökulhlaup occurs when water pressure in the lake exceeds the pressure in a tunnel network. The Glen mechanism occurs when horizontal stress on the wall of a

dam is sufficient to force a hole in the dam; water depths of at least 120 m, and more likely 200 m are required (Tweed and Russell, 1999).

Dam flotation is a very commonly cited drainage trigger, and theoretically occurs in warm based glaciers when the lake level reaches 90% of the dam height, since glacier ice is roughly 10% less dense than water. However, this theoretical triggering point is rarely observed. A flood may be triggered at lower lake levels where crevassing is extensive (Thorarinsson, 1939; Liestøl, 1956), or at higher levels where debris increases the glacier density (Tweed, 2000). Dam flotation has only been observed once in the Canadian High Arctic, in McMaster Lake (Blachut and McCann, 1981). The lake is near the head of Vendom Fiord, Ellesmere Island (Fig. 2.1), and partially drained each year it was studied between 1973 and 1975. The largest jökulhlaup was in 1973, and was likely catalyzed by an enormous 55 mm precipitation event (Cogley and McCann, 1976). However, the lake drained incompletely in each of the three events, with the 1973 event draining only about 3% of the total lake volume.

When a glacier is cold-based and frozen to its bed, flotation cannot occur. In this case, the lake overspills either supraglacially or along a marginal channel, and this drainage is typically not catastrophic. This has been called the '*simplest way imaginable for the drainage to start*' (Liestøl, 1956). However, the only area where this triggering mechanism has been thoroughly described is Axel Heiberg Island, northeast of the head of Expedition Fiord, near the margins of Thompson, White, and Crusoe glaciers (Fig. 2.1). One hundred twenty five lakes were assessed, and all drained supraglacially by overtopping ice dams via outlet channels (Maag, 1969). This mechanism was so pervasive that Maag (1969) called it 'normal drainage'. In this sense, the drainage may not be catastrophic. The only other documented case of cold-based dam overtopping was observed in a July 1967 jökulhlaup upstream of Ekalugad Fiord on Baffin Island (Church, 1972).

When the lake level approaches the dam height, the glacier dam can fail, and the lake drains catastrophically (termed a 'subareal dam breach'). This type of drainage has not yet been described in the Arctic.

2.2.3 Drainage mechanisms and hydrograph shape

Dam flotation, the Glen mechanism, and volcanic activity can allow subglacial and englacial tunnels to form. Tunnel systems are created when sensible heat in moving water is transferred to ice walls through conduction, potential energy is converted to kinetic energy, and ice is mechanically eroded through fluvial abrasion and cavitation (Roberts, 2005). The efficiency of tunnel formation increases with increasing water temperature, discharge, and slope. Conduit development is initially slow, but a positive feedback occurs as tunnel area expansion allows for increasingly more discharge, and more conduit melt (Ng and Björnsson, 2003). The flood ends abruptly when the lake completely drains or ice overburden pressure can seal the dam (Walder and Costa, 1996). Thus, a typical hydrograph has a prolonged approach to peak flow followed by an abrupt decrease in discharge. If a glacier dam is thicker than about 50 m, it can reseal; a thinner dam might result in a loss of the ability for the basin to dam water (Liestøl, 1956; Russell, 1989).

Cold-based ice has been observed to impede tunnel formation. A glacier in northern Sweden that dams a lake has cold-based ice at its perimeter, where ice is thin. Meltwater channels form away from the cold based fringe, under the warm-based central section of the glacier (Klingbjer, 2004).

Although McMaster Lake, Ellesmere Island, drains by flotation, tunnel systems do not develop (Blachut and McCann, 1981). Hydraulic head is low, since there is only about 6 m elevation difference between the dam and the flood outlet, and lake water temperatures are near 0

^{o}C, so little energy is available for melt (Blachut and McCann, 1981). Rather, the lake incompletely drains, discharge is relatively low, and flooding ends when the lake level drops enough to resettle the ice dam.

By contrast, overspilling in the Canadian High Arctic tends to trigger floods with relatively low peak discharge, and lakes have tended to incompletely drain by this mechanism. Three of four overspilling lakes studied in detail in the Expedition Fiord area produce annual floods as a consequence of their incomplete draining (Maag, 1969). Hydrographs tend to show a rapid increase up to a peak, followed by a gradual decrease (Benn and Evans, 1998).

Ice dam breach is likely rare in the Canadian High Arctic since water temperatures are often near freezing, and dams are usually frozen to their beds. Where dam breach does occur, jökulhlaup hydrographs tend to have a very abrupt onset and rapid decline, since the dam fails catastrophically and the lake can drain completely. As a result, the peak discharge and volume drained in these floods tends to be higher than for lakes that drain by tunnel enlargement and overspilling (Walder and Costa, 1996). A subareal breach likely occurred in July 1967 on Baffin Island. About 12 hours after the jökulhlaup began, peak discharge was about 200 m^3/s, compared to a typical peak of about 20 m^3/s. A volume of 4.8 x 10^6 m^3 of water was transported, and 90% of the annual sediment transport in the river occurred during the event (Church, 1972, 1988; Walder and Costa, 1996).

Deviations from idealized hydrographs can occur where temporary ice dammed lakes store meltwater (Roberts et al., 2003), when meltwater leaks through deformable sediments (Gilbert, 1971), or when tunnels are temporarily blocked (Marcus, 1960; Maag, 1969).

2.2.4 Empirical prediction of peak discharge

Given the difficulties of measuring maximum discharge (Q_{max}) during catastrophic flows, several attempts have been made to empirically predict Q_{max} using the volume drained from an ice dammed lake. The first attempt used data from ten ice dammed lakes where Q_{max} and volume drained were known. The resulting power law is called the 'Clague-Mathews' relationship (Clague and Mathews, 1973). More recently, data from 26 lakes allowed the relationship to be refined:

$$Q_{max}=46V^{0.66} \ (r^2=0.70; \text{Walder and Costa, 1996})$$

Floods drained through subaerial dam breaching tend to have higher Q_{max} for a given volume drained compared to jökulhlaups routed through tunnels. The additional data allowed a unique correlation for these floods:

$$Q_{max}=1100V^{0.44} \ (r^2=0.58; \text{Walder and Costa, 1996})$$

The success of the empirical approach is somewhat surprising given the variety of jökulhlaup drainage styles, and climatic and physiographic settings, especially considering that lake water temperature and hydraulic head vary from site to site. However, while these relationships were initially empirically derived, they have subsequently been physically explained (Ng and Björnsson, 2003). Finally, it should be stressed that these relationships are not applicable to cold-based glaciers, where lakes drain by ice-dam overtopping.

2.2.5 The jökulhlaup cycle and climate

The frequency and magnitude of jökulhlaups are related to the triggering and drainage mechanisms, which are in turn related to glacier position. Therefore, jökulhlaup activity might be

related to climate, though likely in complex ways (Evans and Clague, 1994; Ng et al., 2007). Relationships between glacier position and jökulhlaups were first formalized by Thorarinsson (1939), who suggested that a thick glacier dam should produce large floods and vice versa. More recently, an idealized 'jökulhlaup cycle' has been proposed for a tributary glacier that advances across a trunk valley (Clague and Evans, 1994; Evans and Clague, 1994). Initially, a newly advanced glacier is thick, its dam is strong, so the ice dammed lake is large. Drainage is not catastrophic, and is likely caused by overspilling through a marginal or supraglacial channel (Fig. 2.9 #1). When the glacier begins to retreat, its dam is thinned and weakened, and a jökulhlaup cycle begins (Fig. 2.9 #2). Initially the dam is relatively strong, and a large, relatively stable lake can form, so jökulhlaup magnitude is high and frequency is low. With continued retreat, the dam becomes increasingly unstable, and jökulhlaup magnitude continues to decrease (Fig. 2.9 #3). Eventually the glacier no longer dams the valley, and the jökulhlaup cycle ends (Fig. 2.9 #4). Ice dammed lakes are most common during periods of glacial retreat (Evans and Clague, 1994); however, the inverse is expected during advances: jökulhlaup magnitude is initially assumed to be low, with a high frequency of events. Magnitude increases and frequency decreases with continued advance and dam strengthening (Marren, 2005). Examples of the jökulhlaup cycle include a 90-year historical record from Tulsequah Lake (Geertsema and Clague, 2005), and repeated flood deposits in paleolakes downstream of glacial Lake Missoula (Atwater, 1984; Waitt, 1984; Waitt, 1985; Atwater, 1986; Section 2.2.7.2).

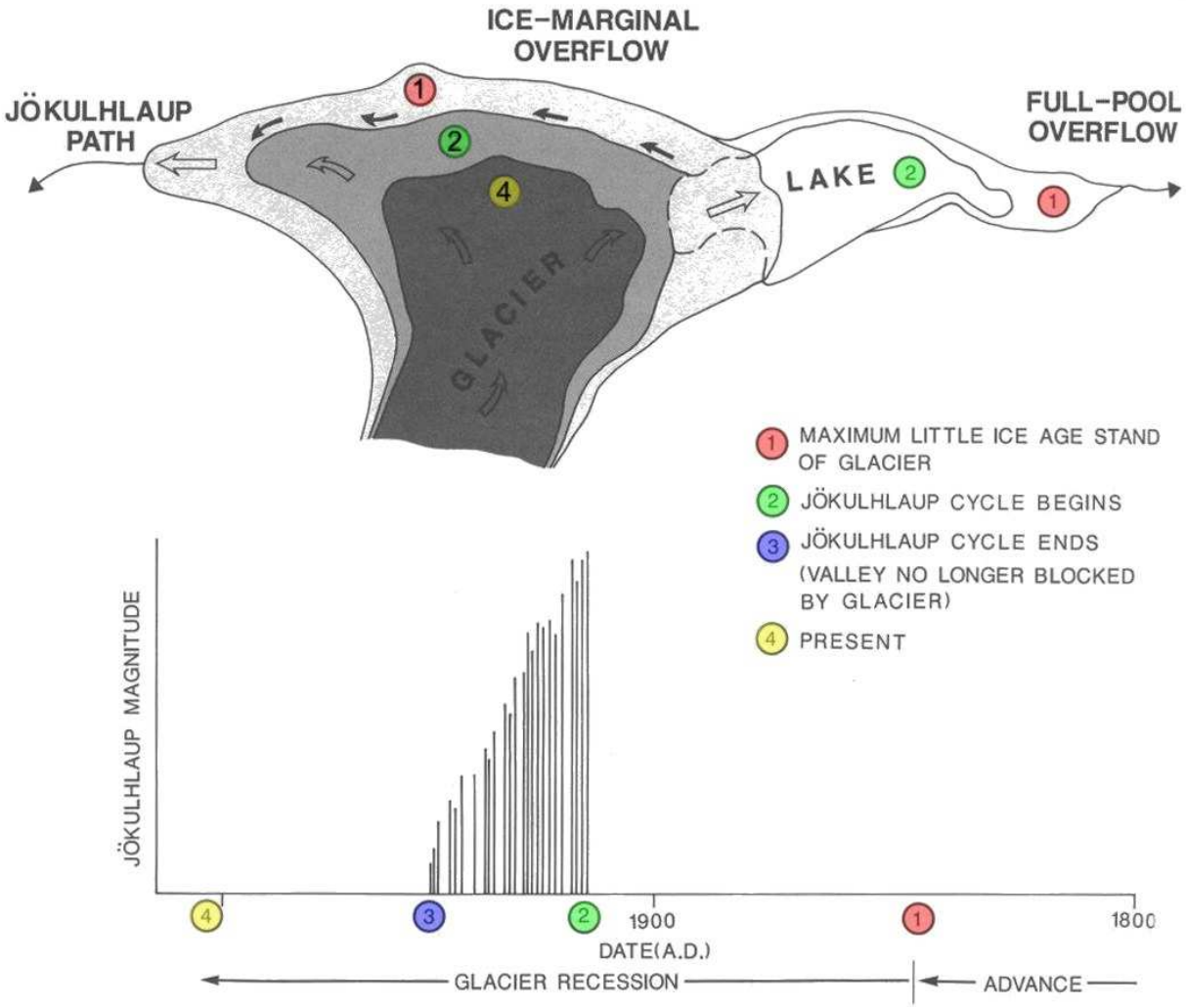

Figure 2.9. The Clague and Evans (1994) jökulhlaup cycle relating jökulhlaup magnitude to glacier position. Time increases to the left on the lower panel (Clague and Evans, 1994).

The role of precipitation on lake filling has been noted in the Canadian High Arctic. From July 21-23, 1973, 54.6 mm of rain were recorded at a station near Sverdrup River (Cogley and McCann, 1976). A few days after the precipitation event, McMaster Lake, which catastrophically drains annually into Sverdrup River, experienced the largest jökulhlaup and largest lake level drop recorded in three years of monitoring (Blachut and McCann, 1981). Maag (1969) also recognized the role of snow and rain. In 1961, unusually thick and late snow in the Between Lake watershed increased the glacier albedo, and delayed and dampened runoff. Later that summer, rainfall caused the lake to rapidly fill. Air temperature and ablation were also cited as controls on

lake filling. It was concluded that "*an ice dammed lake… is a kind of a 'run-off totalizer', from the amount of water in the lake at a particular time, the ablation on the neighbouring glaciers and the weather prior to that date*" (Maag, 1969).

It has also been proposed that extremely large jökulhlaups can *cause* rapid and profound climate change (Colman, 2002; Alley et al., 2003).

2.2.6 Sediment concentration, transport, and supply

Measurements of suspended sediment concentration in jökulhlaups are rare. The highest reported concentration is from the 1996 Grímsvötn jökulhlaup, where discharge reached 50,000 m^3/s, and sediment concentrations were at least 200 g/L (Mulder et al., 2003), which would at least initially be transported as a debris or mud flow with non-Newtonian rheology (Maizels and Russell, 1992; Parsons et al., 2007).

A uniquely detailed and continuous record of suspended sediment and discharge was obtained in a relatively small subglacially-derived jökulhlaup in southern Iceland (Old et al., 2005). Peak sediment concentrations reached about 8.5 g/L at the channel edge, with a peak discharge of 572 m^3/s (Fig. 2.10). Discharge and suspended sediment concentration relationships during the jökulhlaups were significantly different than at times of non-catastrophic discharge. Clockwise hysteresis was clearly observed as suspended sediment on the rising limbs of jökulhlaup hydrographs was readily available, but was limited on falling limbs (Fig. 2.10; cf. Lewkowicz and Wolfe, 1994). Interestingly, suspended sediment particle size during jökulhlaups was less than at times of normal flow, probably because during the jökulhlaup, the subglacial reservoir contributed fine volcanic ash to the fluvial sediment supply (Old et al., 2005).

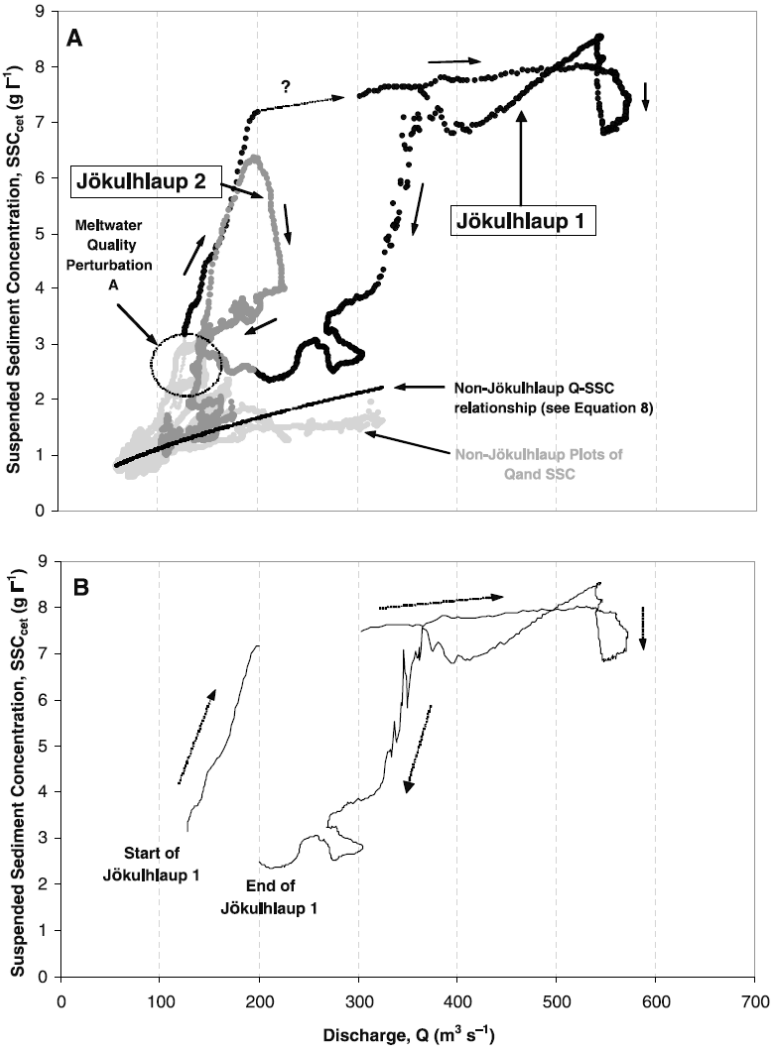

Figure 2.10. Clockwise suspended sediment hysteresis in two jökulhlaups on the Skaftá River, southern Iceland (Old et al., 2005).

Site-specific conditions of sediment supply are likely more important than hydrograph shape in determining sediment transport in jökulhlaups. Nevertheless, it has been hypothesized that extended events are capable of transporting more sediment than jökulhlaups with steep rising and falling limbs, assuming that sediment exhaustion does not occur (Tweed and Russell, 1999). In addition, the first jökulhlaup in a cycle will likely transport the most sediment (Maizels and Russell, 1992).

Jökulhlaups can transport much more sediment in hours to days than is possible during years of non-catastrophic discharge. Subglacially-derived jökulhlaups in Iceland can transport 10^7 to 10^8 tons of sediment in rivers where normal sediment transport rates are about 10^6 tons/a (Marren, 2005). As noted above, the 1967 jökulhlaup in South River, Baffin Island was responsible for about 90% of the annual sediment transport (Church, 1972).

2.2.7 Distal sedimentary processes and deposits, and paleo records of jökulhlaup activity

2.2.7.1 In the marine environment

The 1996 eruption of Gjálp under Vatnajökull in Iceland created one of the largest jökulhlaups of the 20th century. Maximum discharge was 52,000 m^3/s, 3.2 km^3 of water was transported to the sea, and 1-3 x 10^9 tons of sediment were transported in less than 40 hours (Björnsson, 2002). Sediment deposition caused the shoreline to prograde by 7 km^2 where floodwaters entered the ocean at the end of a long sandur (Maria et al., 2000). Despite the immensity of the flood and sediment transport, an analysis of a network of marine sediment cores after the jökulhlaup showed that flood related deposition was remarkably aerially limited, and deposit thicknesses were amazingly low. Flood deposits were 70-200 cm thick, but did not extend for more than 28 km from shore. It was concluded that "deposition during the 1996 jökulhlaup was restricted to nearshore regions close to points of outflow" (Maria et al., 2000). Three explanations were presented: (1) a 25 km long sandur separates the jökulhlaup outflow from the sea, and a large fraction of the sediment was likely deposited there when discharge abruptly ended. (2) much of the sediment transported was likely coarse grained, allowing for rapid nearshore deposition. (3) longshore currents likely deflected fine grained sediment plumes, keeping them close to shore. Two other possibilities are presented here. First, when large floods carry high concentrations of suspended sediment flow into saltwater, flocs form (Kranck, 1973),

settling velocities increase, and suspended sediment is quickly removed from hypopycnal plumes. There is a positive relationship between the rate of floc formation and suspended sediment concentration, so deposits from large, turbid floods tend to be quickly deposited and aerially limited (Hill et al., 2000; Wheatcroft, 2000). Second, freshwater entered the sea initially as an underflow that was denser than the surrounding salt water because of the extraordinarily high suspended particulate concentrations. Particle settling would reduce the density of the underflow and cause it to lift off the sea bottom. This would generate convective upwelling, resulting in decreased flow velocity, and limit the areal extent of the flow (Section 2.1.3; McLeod et al., 1999).

In Saanich Inlet, Vancouver Island, two clay-rich beds date to 10,500 ^{14}C B.P (Blais-Stevens et al., 2003). The beds contain microfossils and clay minerals consistent with an interpreted source of sedimentary rocks on the mainland side of the Strait of Georgia. The first bed is normally graded, while the second has gradational upper and lower contacts. It was concluded that ice dammed lakes in the Fraser and Thompson valleys catastrophically drained, and flowed into the Strait of Georgia just south of Vancouver. Suspended sediment flowed across the 200 m strait, but turbidity currents would have been blocked from entering Saanich Inlet by the 70 m deep sill at its mouth. The flood units were therefore deposited by hypopycnal plumes (Blais-Stevens et al., 2003).

2.2.7.2 In lakes

Bowser Lake, in the Coast Mountains of British Columbia, is downstream of a valley that used to be dammed by the Frank Mackie Glacier (Fig. 2.11). The glacier created Tide Lake, which formed and drained several times in the Holocene, but drained completely in 1930, and has not reformed. Bowser Lake is large (~25 km long), and has a sharp 90 degree bend and sill

halfway along its length (Fig. 2.11). Varves form in the lake sediments; however the bend and sill prevent river generated turbidity currents from entering the distal basin (Gilbert et al., 1997). As a result, recently deposited sediments in the distal basin are diffusely laminated and difficult to distinguish, but appear to be varved. Within these thin, diffuse laminae, two anomalously thick, massive, silty layers with unique mineralogy were noted. The massive deposits are 10 and 8 cm thick, while normal varves at the coring site are 0.25 to 3.5 cm thick. Cesium dating and laminae counting allow their age of deposition to be estimated between the late nineteenth and early twentieth centuries. It was concluded that the deposits represent catastrophic outburst of Tide Lake at the end of the Little Ice Age (Gilbert et al., 1997).

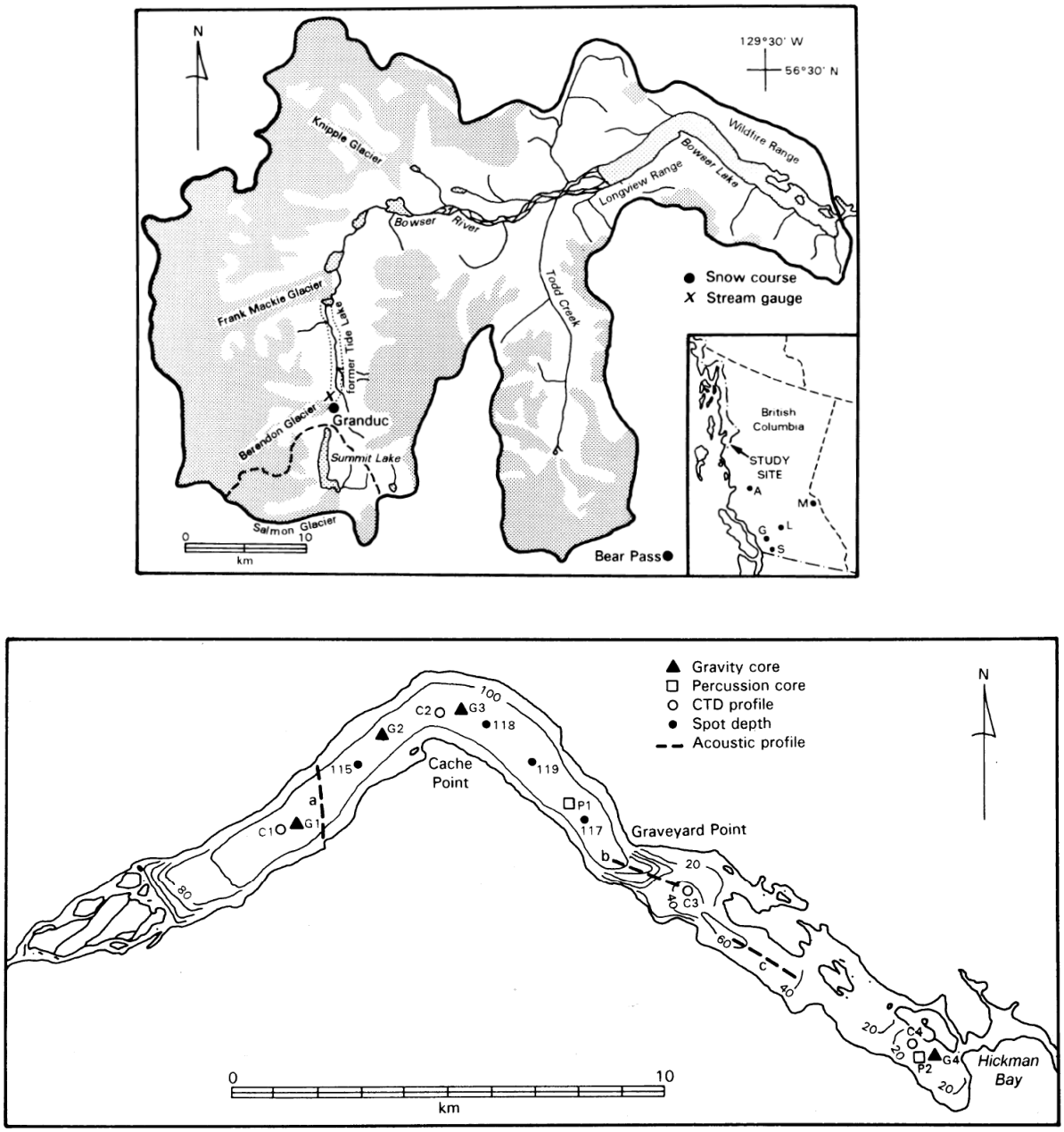

Figure 2.11. Bowser Lake and surroundings (Gilbert et al., 1997).

Glacial Lake Missoula formed in western Montana in the late Wisconsinan when the Purcell Trench Lobe of the Cordilleran Ice Sheet advanced and dammed the Clark Fork River. The dam was about 600 m thick, creating a lake with a maximum volume of about 2600 km^3 that existed between 15,300 and 12,700 B.P (Waitt, 1985; Smith, 2006). Flotation of the ice dam

allowed catastrophic flood(s) to erode the channeled scablands of eastern Washington that extend to the Pacific Ocean. While early debate centered on whether the scablands were created catastrophically, more recent debate has centered on whether one, or many, jökulhlaup(s) occurred (Shaw et al., 1999; Clague et al., 2003). Consensus appears to be forming on the repeated flood hypothesis, which was initially proposed based on examination of fine-grained glaciolacustrine deposits downstream of glacial Lake Missoula (Atwater, 1984; Waitt, 1984; Waitt, 1985; Atwater, 1986). In particular, more than 40 flood beds were separated by 20 to 55 varves over 2000-2500 years (Waitt, 1984; Waitt, 1985). The thickness and grain size of the flood deposits thinned upwards, consistent with successively smaller Lake Missoula jökulhlaups.

Particularly good evidence of repeated Missoula floods is found in glaciolacustrine sediments in the Sanspoil River Valley, which was an arm of glacial lake Columbia (Atwater, 1984; Atwater, 1986). The Sanspoil arm was beside (rather than in) the main path of Missoula floods, which likely provided protection from the highest flood velocities. At least 15 flood deposits are found, separated by 35-55 of varves. Varves were deposited by flows from the north, while flood deposits had indications of paleocurrent from the south. Deposits were likely created by turbidity currents, and are typically fining upward, with cross laminae, plane laminae, with massive sections. At the base of the section, deposits are at least 1 m thick, have sand at their base, and grade upward to silt and clay. Higher in the sections, flood bed thickness decreases to 5-10 cm, evidence of erosion is less frequent, and the beds consist entirely of silt and clays. At the top of the section, the interval between floods decreased, which is interpreted as a decrease in jökulhlaup frequency; however, several periods of increased flood frequency were noted, and explained as periods of glacial advance and dam thickening (Atwater, 1984; Atwater, 1986).

2.2.8 Summary

No complete lake drainage of an ice-dammed lake has been recorded in the Canadian High Arctic. As a consequence of the pervasiveness of cold-based ice, most lakes there drain incompletely by overtopping their ice dams (Maag, 1969). The only jökulhlaups known to be triggered by ice-dam flotation ended when the dam resettled, and resulted in incomplete lake drainage (Blachut and McCann, 1981).

Ice dammed lakes in the Canadian High Arctic that drain by dam overtopping are likely about to begin a jökulhlaup cycle as climate warms and glaciers thin and retreat. By contrast, many lakes at lower latitudes are at the end of their jökulhlaup cycle because of post-little ice age warming, glacial retreat, dam thinning, increased flood frequency, and decreased flood magnitude (e.g. Geertsema and Clague, 2005). Study of High Arctic ice dammed lakes thus provide analogues to postglacial physiography at more southern latitudes.

Given the low contributions of suspended sediment required to produce hyperpycnal flows in freshwater lakes, it is not surprising that few studies of jökulhlaup deposits in downstream water bodies have been attempted. Reconstructions from freshwater lakes have come from areas far from the source of the jökulhlaup, and where sills or bends could potentially restrict hyperpycnal flows in more distal areas. In the marine environment, hyperpycnal flows may loft off the bed early, but the remaining hypopycnal flows tend to be deflected by currents and produce aerially limited deposits, except where flow is confined.

2.3 PREVIOUS RESEARCH AT LAKE TUBORG

2.3.1 Introduction

Lake Tuborg is a large glacially-fed meromictic lake on Ellesmere Island (Figs. 2.1, 3.1). It was once a fiord, and was isolated from the sea at some point in the past. The lake has a large, deep saltwater basin (Fig. 2.12), with a sharp and strong chemocline at about 56 m depth (Fig. 2.13a) that likely strongly inhibits hyperpycnal flows (Section 2.1.5). Portions of its bottom sediments are varved, and a large ice-dammed lake exists above its northeast end. In addition, hyperpycnal flows are likely minimized in distal locations because a shallow sill separates a proximal freshwater basin from a distal saltwater basin (Fig. 2.12). Therefore, the lake may be an ideal location to reconstruct several millennia of jökulhlaup activity (Lewis et al., 2008).

Limnological research at Lake Tuborg included early pioneering research on the limnology of arctic meromictic lakes. A long record of physical lake conditions exists, as CTD profiles have occurred intermittently between 1963 and 2005 (Table 2.3). Studies of the varved lake record suggest that this time period is anomalous in at least the last thousand years, as the lake appears to be increasingly influenced by large catastrophic jökulhlaups that subtly dilute the saltwater in the southwest basin, and produce recognizable thick deposits in the distal basin (Chapters 3 and 4; Smith et al., 2004; Lewis et al., 2008).

A review of the physical and chemical limnological work (Section 2.3.2), and previous paleoenvironmental reconstructions from the lake (Section 2.3.4), provide insight into the evolution of the lake and the surrounding landscape, while a review of in-situ hydrometeorology studies shows the climatic, meteorologic, and geomorphic controls on sediment delivery to the lake (Section 2.3.3).

2.3.2 Water chemistry and physical limnology

Sr/Cl ratios of water from the Tuborg monimolimnion are very similar to the ratios found in seawater (Jones and Faure, 1972). It has been suggested that marine isolation occurred at approximately 3000 yr BP, based on ^{14}C measurements from bicarbonate in the monimolimnion (Long, 1967). However, it is possible that the ^{14}C was contaminated by old carbon in the watershed, so this is likely a maximum date for isolation. The lake has certainly been isolated since at least 1883, when J.B. Lockwood sledged through its valley.

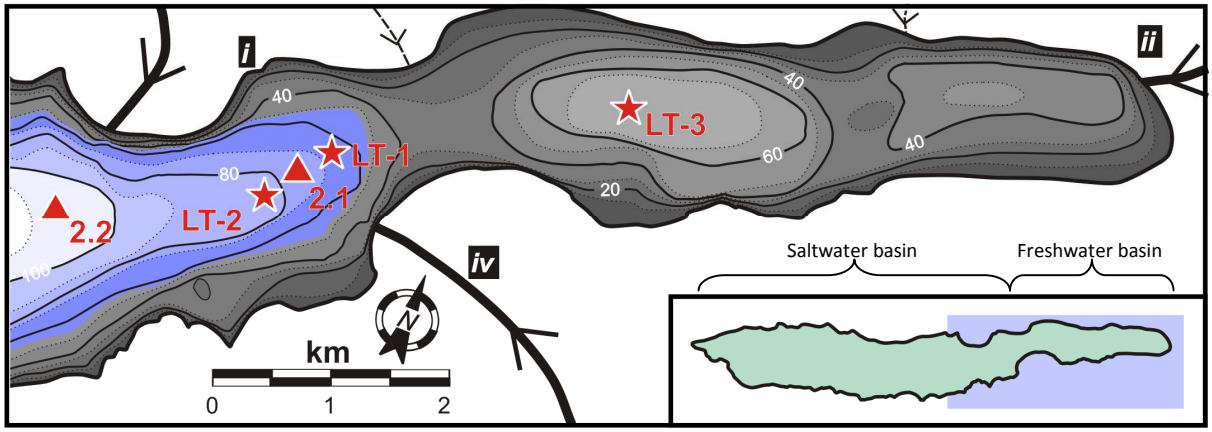

Figure 2.12. The northeast portion of Lake Tuborg, showing locations discussed in this chapter. Blue shaded areas are regions of the lake deeper than the 55-56 m chemocline. Triangles are CTD casts, and stars are coring locations. Station 2.1 is the location of a CTD cast obtained in 1995, and station 2.2 is a 2001 CTD cast (Fig. 2.13). LT1-3 are percussion cores obtained in 1995 (Figs. 2.16, 2.17). '*i*', '*ii*', and '*iv*' are major tributaries. *iv* is the Deception River, and marks the 1995 hydrometeorological station. The inset shows the portion of Lake Tuborg mapped here. See Fig. 3.1 for a smaller scale map.

Table 2.3. Lake Tuborg monimolimnion salinity, conductivity, chemocline depth, and temperature, 1963-2005*

Year	PPT**	PSU**	Conductivity (S/m)	Specific Conductance (µS/cm)	Temp-erature (^{o}C)	Chemocline Depth (m)	Source
1963	**25.6**		2.3514	42,753	2.5	53-57	Hattersley-Smith and Serson, 1964
1967	**~25.9**		~2.3953	~43,232	2.8	~54	Bowman and Long, 1967
1993		24.6	2.2740	41,196‡	2.6	56.7	Ludlam, 1996
1995	**25.1**		2.3203	42,036	2.6	58	Phelps, 1996
2001		25.0	2.3108	**41,893**	2.58	55.5	Lewis et al., 2007
2003		24.7	2.2797	**41,389**	2.54	55.5	Lewis et al., 2007
2005		22.9	2.1123	**38,758**	2.25	56	Lewis et al., unpublished

** Bold indicates the salinity/conductivity reported in the literature. Other salinity/conductivity values are calculated using the International Equation of State Calculator (JPOTS Editorial Panel, 1991; Chapman, 2006).*

***Early salinity measurements were reported in PPT. For our purposes, PPT and PSU are equivalent.*

*‡This value is slightly higher than the 40,900 µS/cm reported in Ludlam, 1996, who increased conductivity by 2%/^{o}C to 25^{o}C to determine specific conductance (SpC). By contrast, we used SpC (µS/cm) = (C * 10,000) / (1 + A * [T – 25]), where (C = conductivity (S/m), T = temperature (° C), A = 0.020 (User's Manual for SEASOFT-Win32: SBE Data Processing, 2005).*

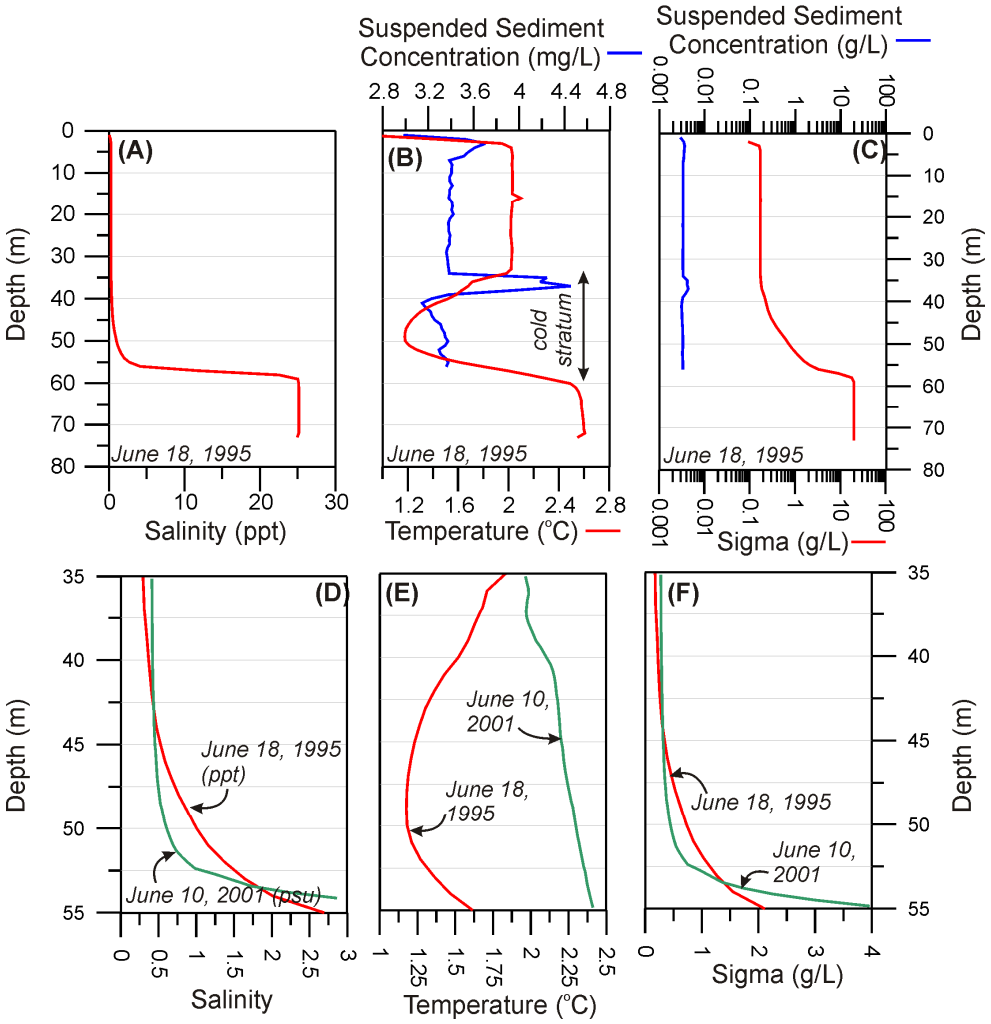

Fig. 2.13. A comparison of CTD casts from Lake Tuborg obtained in 1995 and 2001. Panels A, B, and C are salinity, temperature, suspended sediment concentration, and sigma density (σ; σ =ρ-1000 g/L, where ρ is potential density), recorded at Station 2.1 on June 18, 1995 (Phelps, 1996). A cold stratum is present between 35 m and the chemocline (panel B). Note that peak suspended sediment concentration on June 18, 1995 would have had to increase by more than three orders of magnitude to exceed the density contributed by saltwater below about 56 m depth (panel C). Panels D, E, and F highlight the unique physical and chemical conditions in the cold stratum relative to a nearby cast obtained on June 10, 2001. Station locations are marked on Fig. 2.12.

It was discovered in June 1963 that Lake Tuborg is meromictic (Hattersley-Smith and Serson, 1964). Water samples were obtained at 3, 44.5, 53, and 57 m depth for determination of salinity, and a temperature profile was performed in the upper 57 m of the meromictic basin. This early work showed that Lake Tuborg has an extremely sharp and strong chemocline (Fig. 2.13A), which imparts a strong density contrast between the saltwater and overlying freshwater (Fig.

2.13C). Very similar bottom water salinities were measured in 1967, when a more complete profile was obtained to a depth of 110 m (Table 2.3; Bowman and Long, 1968).

The physical properties of the Lake Tuborg water column were not measured again until June 6, 1993 (Table 2.3; Ludlam, 1996). Unfortunately, the conductivity of the monimolimnion at that time is not precisely known. In Table 2 of Ludlam, 1996, maximum Tuborg specific conductance is listed at 40,900 µS/cm (24.59 PSU). However, a range between 40,900 and 49,600 µS/cm is cited in the text. The lower limit of the salinity range is *lower* than salinities measured with the same instrument two years later, *after* a jökulhlaup occurred (R.M. Koerner, personal communication, 1996; Phelps, 1996). The accuracy of conductivity cell drifts through time, and the drift is almost always towards lower conductivity (D. Murphy, personal communication, 2004), so it is possible that the conductivity cell had not been calibrated recently, or was fouled in 1993. The upper limit of this range is extraordinarily high relative to all other profiles from the lake, and has a nearly oceanic salinity (30.19 PSU), which is highly suspect given the previous and subsequent salinity measurements Lake Tuborg (Table 2.3).

A jökulhlaup occurred later the same summer that Ludlam obtained his CTD casts (1993). The next water profiles were obtained in 1995 at Station 2.1 (Fig. 2.13; Table 2.3), when maximum salinity was 25.14‰ (~42,040 µS/cm; Phelps, 1996). Interestingly, in early June 1995, temperature profiles showed a very pronounced temperature minimum between 35 m and the chemocline (a 'cold stratum'; Fig. 2.13b). Compared to profiles obtained nearby in 2001, salinities within the 1995 cold stratum were much higher (Fig. 2.13d), which significantly increased water density between 45 and 53 m (Fig. 2.13f). In addition, in 1995, a weak interflow was present on top of the relatively saline water in the cold strata (Fig. 2.13b). The elevated salinity and density in the cold stratum likely controlled the vertical position of the interflow in the water column. However, the suspended sediment concentration in the interflow made a truly minuscule addition to the total density of the water in the cold stratum (Fig. 2.13c).

Cold strata appear to form in the meromictic basin of Lake Tuborg following jökulhlaups. The cold stratum recorded in 1995 is consistent —in position, but not magnitude— with a cold stratum that was recorded after the 2003 jökulhlaup (*cf.* Figs. 3.11, 3.12). Extremely cold, dense, sediment laden water from the ice-dammed lake flowed above the chemocline and on top of the more dense monimolimnion, leaving a zone of brackish, mixed water above the chemocline all the way to southwest end of Lake Tuborg (Section 3.5.3.3). In 2001, monimolimnion salinity was 25.02 PSU (41,893µS/cm). After the 2003 jökulhlaup, it was 24.69 PSU (41,389 µS/cm; Fig. 3.12).

It is remarkable that monimolimnion salinity and temperature changed very little over the forty year measurement period (Table 2.3); especially considering that large jökulhlaups have likely only begun occurring there since the early 1960's (Chapter 4; Lewis et al., 2008). This attests to the large resistance to mixing induced by the sharp and strong chemocline (Fig. 2.2, Table 2.2).

2.3.3 Hydrometeorology

Monitoring weather, discharge and sediment flux over one or more full melt seasons is extremely beneficial for understanding, and even calibrating, the paleoenvironmental and paleoclimatic signal contained in lake sediments (Hardy, 1996; Hardy et al., 1996). Such a study was undertaken at Lake Tuborg from early June to late July, 1995 (Braun, 1997; Braun et al., 2000a). The Deception River (unofficial name; '*iv*' on Fig. 2.12), the largest glacially-fed tributary at Lake Tuborg, was monitored. The Deception River watershed drains approximately 460 km^2, and is approximately 88% glacierized.

First, weather conditions at Lake Tuborg and Eureka were compared to determine whether meteorologic controls on streamflow and sediment flux at Lake Tuborg might be

regionally coherent. Correlation coefficients for daily air temperatures at Eureka (surface and 900 mB) and the Tuborg watershed (63, 800, and 1261 m ASL) were extraordinarily high (0.76-0.84) considering that more than 200 km separates the two sites. Atmospheric pressure at both locations was also highly correlated (r=0.98). Air temperatures at Lake Tuborg were on average 1.4^{o}C warmer than at Eureka, probably because of a slight continental effect at the lake (Braun, 1997).

Snowmelt and sediment transport in 1995 were divided into four distinct subperiods (Table 2.4; Braun, 1997). All sub-periods have high correlations between air temperature and discharge on hourly and daily scales, after variable lags were introduced to compensate for delays between solar energy inputs, snowmelt, meltwater retention, and water transport.

Table 2.4. Summary of hydrometeorologic conditions for the four subperiods of the 1995 Deception River monitoring campaign.

Sub-period	**Dates (1995)**	**Days**	**MDD ***	**Cumulative Q (x10^5 m^3)**	**Q (%)**	**Rate (x10^4 m^3/d)**	**SSQ (x10^3 kg)**	**SSQ (%)**	**SSQ Rate (x10^3 kg/d)**
1	June 2 - June 12	11	37.8	3.4	6.5	3.1	63	2.5	5.70
2	June 13 - July 7	25	153.3	8.1	15.5	3.3	15	0.6	0.59
3	July 8 - July 15	8	129.4	19.8	37.8	24.8	143	5.7	17.9
4	July 16 - July 20	5	30.1	21.1	40.2	105	2272	91.2	1140
		∑	**350.6**	**52.4**	**100**		**2493**	**100**	

*Melting degree days (MDD) using daily average air temperature at Camp, 63 m asl.

Discharge and sediment transport co-varied on seasonal, daily, and hourly scales, but in somewhat complex and temporally variable ways. Nevertheless, polynomial regression curves for hourly and daily suspended sediment concentration and discharge yielded high correlation coefficients (polynomial fit; hourly r=0.84; daily r=0.99) without the need for treating each of the four subperiods separately.

In Subperiod 1, snowmelt occurred in low watershed elevations and within stream channels. Discharge lagged air temperature by almost a day due to long meltwater retention times in snowpack and immature channel development. In Subperiod 2, snowmelt occurred at somewhat higher elevations, but discharge was very low (Fig. 2.14). Very little sediment transport occurred (Table 2.4; Fig. 2.14d), probably because discharge decreased and much of the readily available sediment had been transported in Subperiod 1. By Subperiod 3, snowmelt had reached a sufficiently high elevation to begin melting winter snowpack on the Agassiz Ice Cap. Discharge and sediment transport were high, and increased throughout this period (Fig. 2.14).

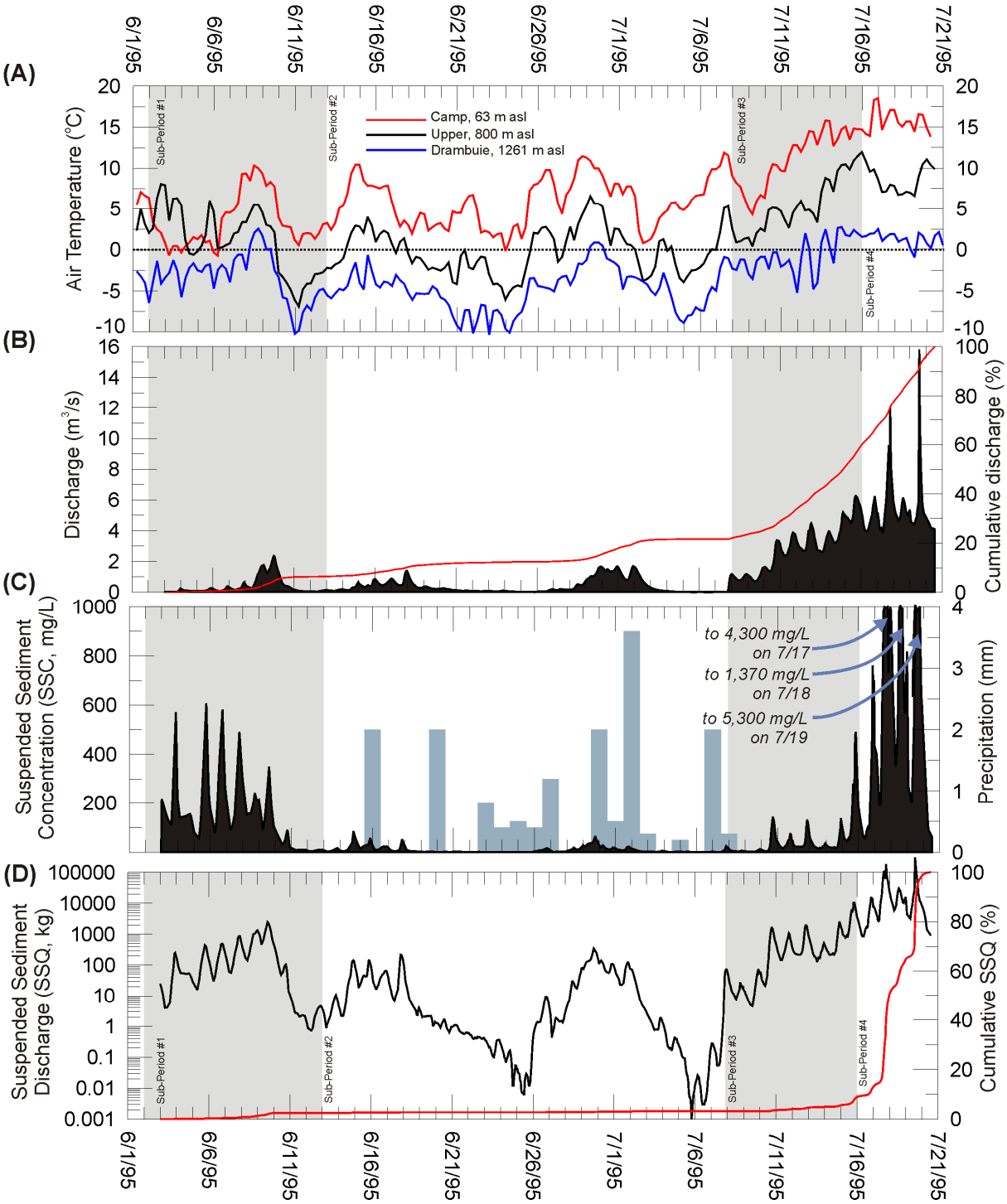

Fig. 2.14. Hydrometeorologic variables measured in the Deception River in 1995. Hydrologic subperiods are alternately shaded gray and unshaded. Redrawn from Braun, 1997.

By far the most significant hydrologic and sediment transport events of the summer occurred on July 17 and 19, when two slush flows occurred (Fig. 2.14). Over 90% of the recorded sediment transport occurred in only five days, and the rate of suspended sediment transported exceeded 1000 metric tons per day in Subperiod 4 (Table 2.4). The highest single suspended sediment concentration was 5.3 g/L, measured during the July 19 event. Discharge data are somewhat uncertain, since channel instability and braiding during the slush flow events was a serious impediment to using temporally consistent stage/discharge rating curves. Furthermore, the hydrologic monitoring station was destroyed on the morning of July 19. For these reasons, after July 17, discharge was estimated using previously determined suspended sediment concentration rating curves (Braun, 1997).

It is difficult to estimate whether slush flows were common in previous years. However, the melting degree days needed to initiate the 1995 slush flow event is known, and air temperature at Eureka and Lake Tuborg co-vary predictably. Therefore, the 1948-to-modern Eureka air temperature record can be used to identify years where slush flow events were particularly likely. It was concluded that threshold melting degree day rates were exceeded in nine years: 1956, 1957, 1959, 1960, 1962, 1968, 1976, 1991, 1994 (Braun, 1997). Given the uncertainties of this degree day model, Braun et al. (2000) concluded that "*slushflows… may very well be an annually recurring phenomena and the 'normal' rather than exceptional mode of snowmelt runoff initiation on the ice cap margin*" This supposition is supported by subsequent fieldwork at Lake Tuborg, where extreme discharge events were noted in mid-to-late late July in the Deception River in 2001, 2002, and 2003.

Summer rainfall was low at Lake Tuborg in 1995, and was insufficient to cause an increase in discharge (Fig. 2.14C). Most precipitation fell in solid form in the majority of the Deception river watershed.

2.3.4 Paleoenvironment

Three percussion cores were obtained in 1995 in the saltwater and freshwater basins of Lake Tuborg (Fig. 2.12; LT1-3; core lengths 234-250 cm; Smith, 1997; Smith et al., 2004). Each core was finely laminated, and laminae counts were performed on polished epoxy impregnated slabs of sediment. To determine whether the laminae were deposited annually, ten subsamples were taken from the upper nine centimeters of LT-2 for determination of ^{210}Pb, ^{226}Ra, and ^{137}Cs activities by alpha and gamma spectroscopy (Fig. 2.15). No wood fragments were found, precluding the use of ^{14}C dating.

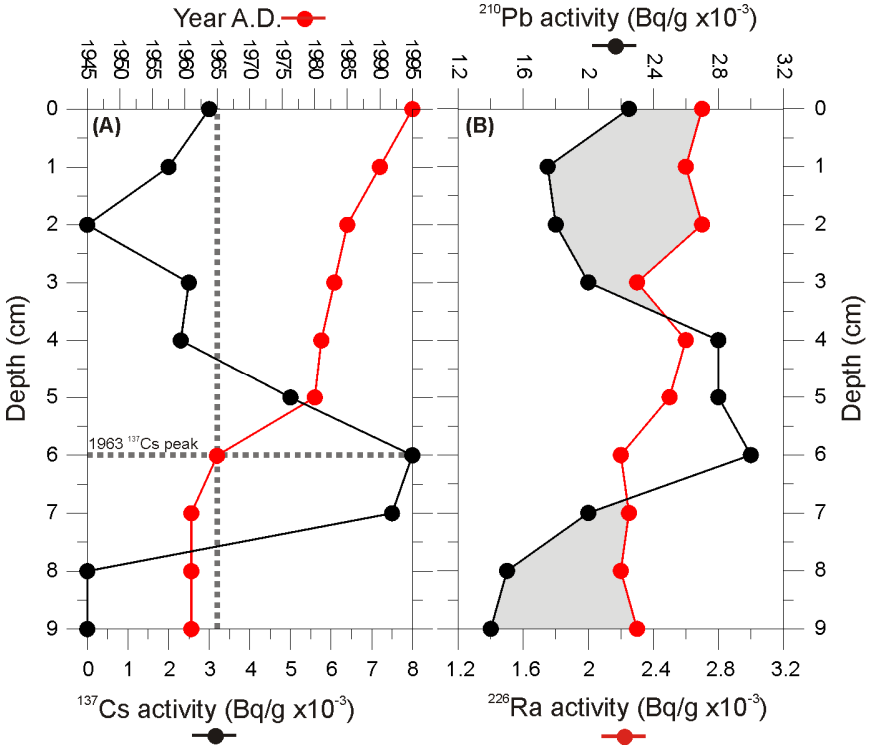

Fig. 2.15. ^{137}Cs, ^{210}Pb and ^{226}Ra activities from the upper nine centimeters of core LT-2, with the corresponding varve/age plot. Gray shading highlights areas where ^{226}Ra activity is greater than ^{210}Pb activity. Redrawn from Smith, 1997.

Gamma counting of ^{137}Cs activity revealed a strong and distinct peak at the depth of the 1965 varve in core LT-2 (Fig. 2.15a). This is a good indication that the counted laminae were indeed varves, and provides support for laminae counting as a chronometer in the deeper sections

of the sediment cores. ^{137}Cs typically peaks in sediment deposited in 1963, reflecting the peak in ^{137}Cs fallout from atmospheric nuclear bomb testing, which occurred immediately before the 'Partial Test Ban Treaty' was enacted (Wolfe et al., 2004). No smaller peak associated with the 1986 Chernobyl accident was found in the upper sediments (Fig. 2.15a; Smith, 1997).

Three possibilities could easily explain the 1963 peak being found at the depth of the 1965 varve: (1) The subsample thickness likely spanned multiple varves. The sedimentation rate near the 1963 peak was 5-10 years/cm, and gamma analysis of ^{137}Cs requires 7-15 g of freeze dried sediment. (2) Laminae subsampled from the core face may been at slightly different depths from those in thin sections, especially since the dated sediment was from a percussion core, where the laminae were likely somewhat bowed, even near the surface. (3) Two subannual laminae may have been counted as varves, resulting in a two year age model error over 30 years.

^{210}Pb was measured on ten samples in core LT-2 by alpha counting (Fig. 2.15b); however, no age models could be constructed, since: (1) the ^{210}Pb profile did not decrease exponentially with depth as should ideally occur (Wolfe et al., 2004), and (2) ^{226}Ra activity was greater than ^{210}Pb activity in two areas (Fig. 2.15b; Smith, 1997). ^{210}Pb forms both in the atmosphere ('unsupported' ^{210}Pb) and in the subsurface ('supported' ^{210}Pb) as part of the ^{238}U decay series (Wolfe et al., 2004). The ^{210}Pb dating technique requires that total ^{210}Pb (supported plus unsupported) exceed ^{226}Ra, since ^{226}Ra is used as a proxy for supported ^{210}Pb activity only. It was hypothesized that the high ^{226}Ra in Lake Tuborg sediments was sourced from local bedrock, notably the Danish River Formation (Smith, 1997). Unsupported ^{210}Pb was likely very low, since the nearly perennial lake ice would minimize lake/atmosphere interaction (Wolfe et al., 2004).

Varve thickness time series and grain size results from each core show thin, fine-grained laminae interrupted by occasional thick, coarse deposits (Fig. 2.16; Smith, 1997; Smith et al., 2004). The sedimentation rate was particularly high in LT-3, in the freshwater basin (Figs. 2.12,

2.16). There is a distinct but episodic increase in sedimentation rate in LT-2 after about 1862. In core LT-2 from the saltwater basin (Fig. 2.12), mean sedimentation rate was comparatively low, and discrete sand beds were less common, though thick (up to ~30 cm).

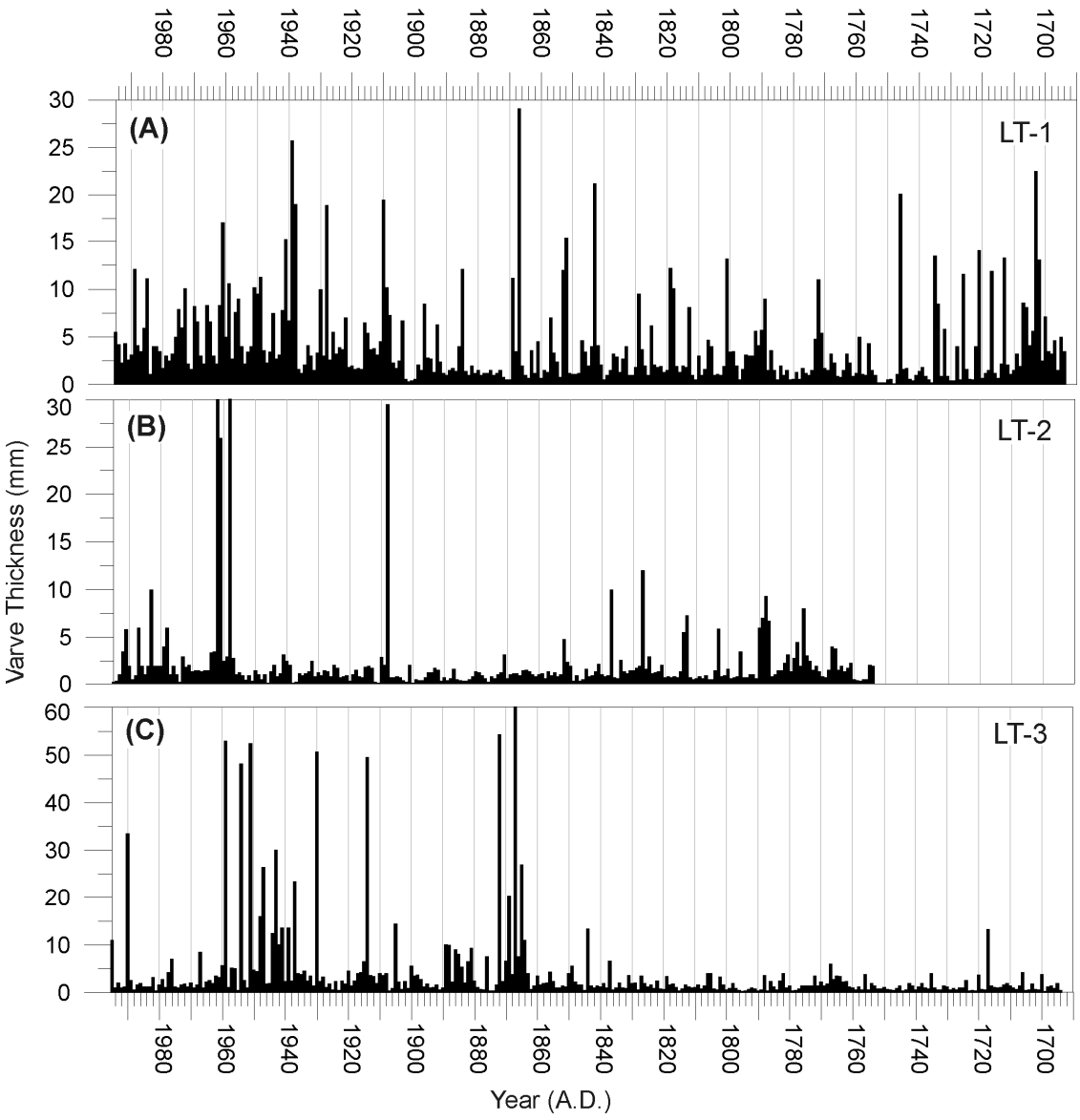

Fig. 2.16. Varve thickness time series for cores LT1-3. Redrawn from Smith, 1997.

Site LT-3 in the freshwater basin would receive large volumes of sediment during jökulhlaups from the ice-dammed lake (Fig. 2.12), probably largely via high energy and potentially initially erosive turbidity currents. To some extent LT-2 and LT-1 would be protected

from turbidity currents by the 35 m sill that separates the saltwater from freshwater basins (Fig. 2.12; Chapter 3), and the high density of the salt water (Fig. 2.13a, c). However, sediment from episodic high energy slush flows from ponded meltwater on the Agassiz Ice Cap (Braun, 1997; Braun et al., 2000a), appear to have influenced sedimentation at these sites that are approximately 1-1.5 km from inflow at tributary '*iv*'.

The varve thickness records from cores LT1-3 were combined by averaging to produce a 'stacked mean' (Smith et al., 2004; Fig. 2.17a). A distinct increase in sedimentation rate, and an increase in the occurrence of discrete, thick laminae, occurred after about 1860, and continued at least until the early 1960's. The increase in varve thickness after approximately 1862 is attributable to an increase in summer air temperature following the Little Ice Age, which would have raised freezing levels on the Agassiz Ice Cap, produced more supraglacial melt, and transported more sediment to Lake Tuborg. Peak melt appears to have occurred in the 1950's, which is consistent with historical records of warmth from the region (Smith et al., 2004).

The stacked mean thickness record is also significantly correlated with ice core records from the Agassiz Ice Cap (Fig. 2.17c). Annual laminae in the ice core records variable percentages of melt, which is used as a proxy for summer warmth (Fisher et al., 1995). In a general sense, it appears that warm summers on the Agassiz Ice Cap produce large amounts of glacial melt, which is transported to Lake Tuborg, forming thick varves. However, it is important to note that the three coring sites receive sediments from multiple sources, and the composite varve thickness record integrates signals from slush flows as well as from jökulhlaups. It is likely that the component of the stacked mean record that correlates with Agassiz Ice Cap melt percent is largely from glacial melt and slush flow events. Residuals are likely from signals such as jökulhlaups, sediment availability, climate, weather, and within-lake processes (Gilbert, 1975; Leonard, 1986; Lamoureux, 1999, 2000; Hodder et al., 2007; Lewis et al., 2007). Disentangling

some of these signals, and obtaining a record that extends beyond the last 300 years are potential areas for new research at Lake Tuborg (Chapters 3 and 4).

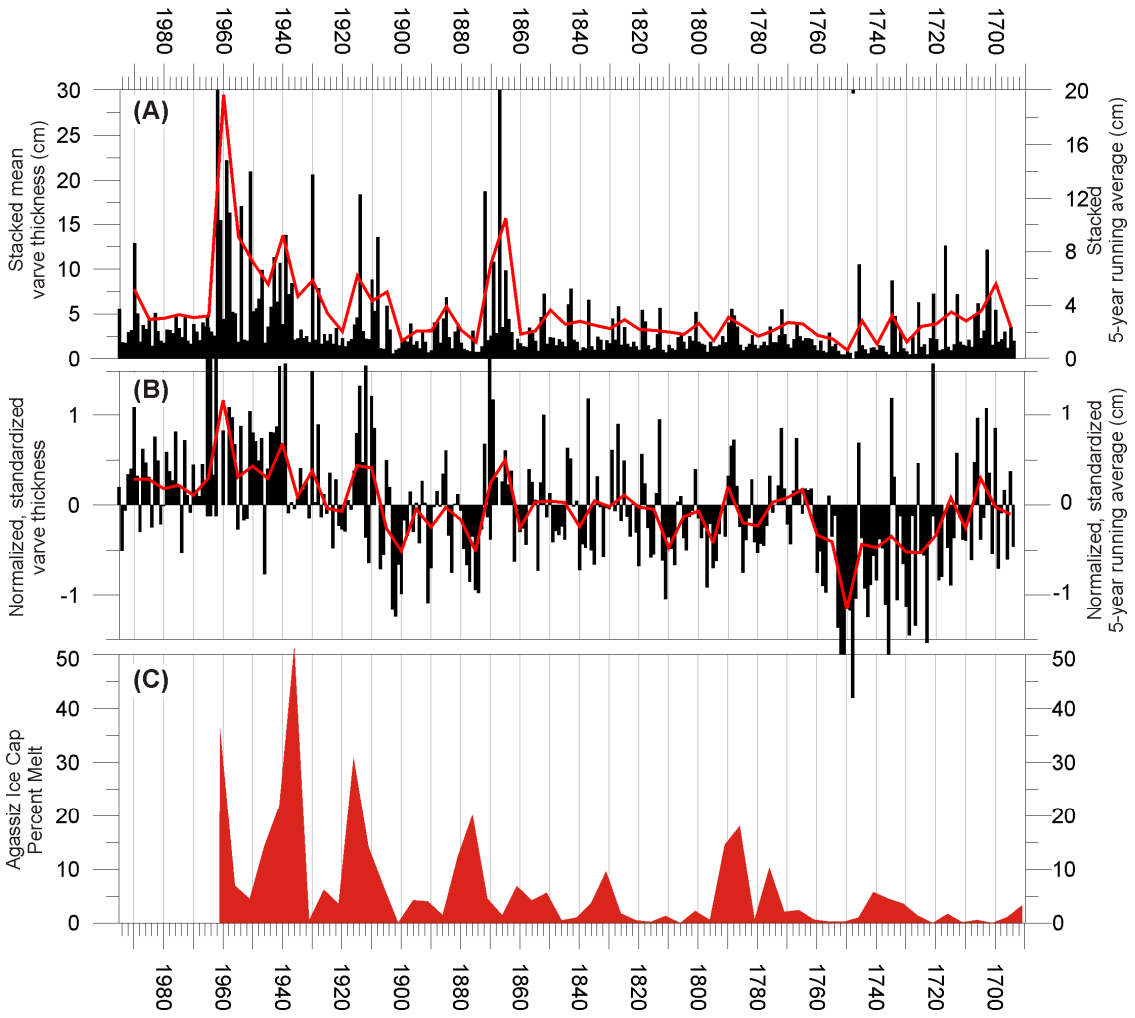

Fig. 2.17. Comparison of Smith (1997) varve thicknesses with Agassiz Ice Cap Melt percent. (A) Stacked mean of cores LT1-3 with a 5-year running average (red). Redrawn from Smith, 1997. (B) Log-normalized, standardized, and averaged time series for cores LT1-3 with a 5-year running average (red). (C) 5-year running average of Agassiz Ice Cap melt % (redrawn from Fisher et al., 1995).

It should be noted that mean varve thickness and standard deviation varied greatly between cores LT1-3 (Fig. 2.16a-c). Therefore, the 'stacked mean' (Fig. 2.17a), where an arithmetic mean was taken from the three core records may not be meaningful. A more statistically valid approach would be to 'standardize' each thickness measurement to the time series' mean and standard deviation (Fig. 2.17b; Ohlendorf et al., 1997; Overpeck et al., 1997),

then log-normalize each time series (each time series failed a Shapiro-Wilk normal distribution test; Hodder et al., 2007; Rittenour et al., 2000). This procedure slightly weakens correlations with the Agassiz Ice Cap melt record (Fig. 2.17c); however, the correlation coefficient remains statistically significant ($r=0.58$ $p<0.01$ for the stacked mean approach; $r=0.42$ $p<0.01$ for the log-normalized, standardized approach).

2.3.5 Conclusions

The majority of sediment is delivered to Lake Tuborg during glacial melt during times of peak summer warmth, though water storage in supraglacial ponds and an ice dammed lake may make the relationship between climate and sedimentation indirect. Strong climatic seasonality produces a distinct runoff period, and the stability of the water column allows classic varves to form in the lake. Analysis of the varve record of the lake shows a pronounced post-Little Ice Age increase in varve thickness that is consistent with inferred warming from other regional paleoclimatic records. Lake Tuborg has a uniquely long limnological observation record, and the most salient feature of this record is the relative lack of change in salinity and temperature of the monimolimnion over a forty year period that included several extremely energetic and large inputs of sediment and water. This is understandable given the bathymetry and morphometry of Lake Tuborg. But above all, the relative lack of thermal and chemical change is due to the strong stability provided by the sharp and strong chemocline, and the extreme density of the saltwater layer relative to overlying freshwater and suspended sediment concentrations in the lake and rivers.

CHAPTER 3

LIMNOLOGY, SEDIMENTOLOGY, AND HYDROLOGY OF A JÖKULHLAUP INTO A MEROMICTIC HIGH ARCTIC LAKE

3.1 Abstract

A large ice-dammed lake drained catastrophically into Lake Tuborg, Ellesmere Island, beginning on 25 July 2003. Limnological, sedimentological, and hydrological parameters were recorded before, during, and after this event.

For several weeks prior to the jökulhlaup, water overtopped the ice-dammed lake, and flowed into Lake Tuborg's freshwater basin. A shallow sill separates the freshwater basin from a larger, deeper basin containing ~25 PSU (Practical Salinity Units) saltwater. The sill blocked underflows from entering the saltwater basin before the jökulhlaup.

The ice-dammed lake drained completely and catastrophically when englacial or subglacial conduits developed, and a glacier portal formed 980 m from the Lake Tuborg shore, marking the beginning of the jökulhlaup. The level of Lake Tuborg increased by 7.6 m in 84 hours. This jökulhlaup is the largest known to have occurred in the High Arctic, and the largest witnessed in Canada since 1947. A strata of very cold water flowed above the chemocline for about 14 km, from the sill to the southwest end of the lake. The cold strata turbulently mixed with underlying salt water, allowing for saltwater flocculation of suspended sediment, causing rapid settling. The saltwater layer very slightly freshened and cooled. Near surface sediments close to the sill derived from the jökulhlaup are coarse and laminated; however, no erosion occurred toward the distal end of the lake, where a fining upward unit with a coarse base was deposited.

3.2 Introduction

Jökulhlaups (Icelandic for 'glacier-burst') have never been monitored in detail entering downstream water bodies. The potential for erosion and sediment bypassing during jökulhlaups is assumed to be great, and this is probably why models describing glacier dam position and jökulhlaup frequency and intensity (e.g., Clague and Evans, 1994) have not yet been tested using long sediment archives. If a site could be identified where a characteristic jökulhlaup facies is deposited without producing an unconformity, an uninterrupted record of jökulhlaup frequency could be obtained from a sediment archive.

Lake Tuborg is a large, fiord-type lake on Ellesmere Island in the Canadian High Arctic (Fig. 3.1) that is adjacent to the Agassiz Ice Cap. Its bottom sediments are annually laminated (varved) in some locations. It also contains trapped saltwater (it is meromictic). A large ice-dammed lake catastrophically drained into Lake Tuborg in July 2003. A limnologic process study was underway in Lake Tuborg at the time of the jökulhlaup. CTD casts, surface gravity cores, and a lake level record were obtained in the 2001-2003 melt seasons, so unique records of physical lake conditions before, during, and after the jökulhlaup were obtained.

A major objective of this paper is to identify the type and spatial variability of jökulhlaup-derived processes and deposits. These data also provide an opportunity to differentiate jökulhlaup-derived lacustrine sedimentary processes and deposits from those that are not jökulhlaup-derived. This is particularly important at Lake Tuborg because there are several relatively small supraglacial lakes on the Agassiz Ice Cap that drain—perhaps annually—as slush flows, that quickly and energetically transport large volumes of sediment to the lake (Braun et al., 2000). The data also allow characterization of boundary layer mixing processes along the sharp and strong Lake Tuborg chemocline; these processes have previously only been recorded in

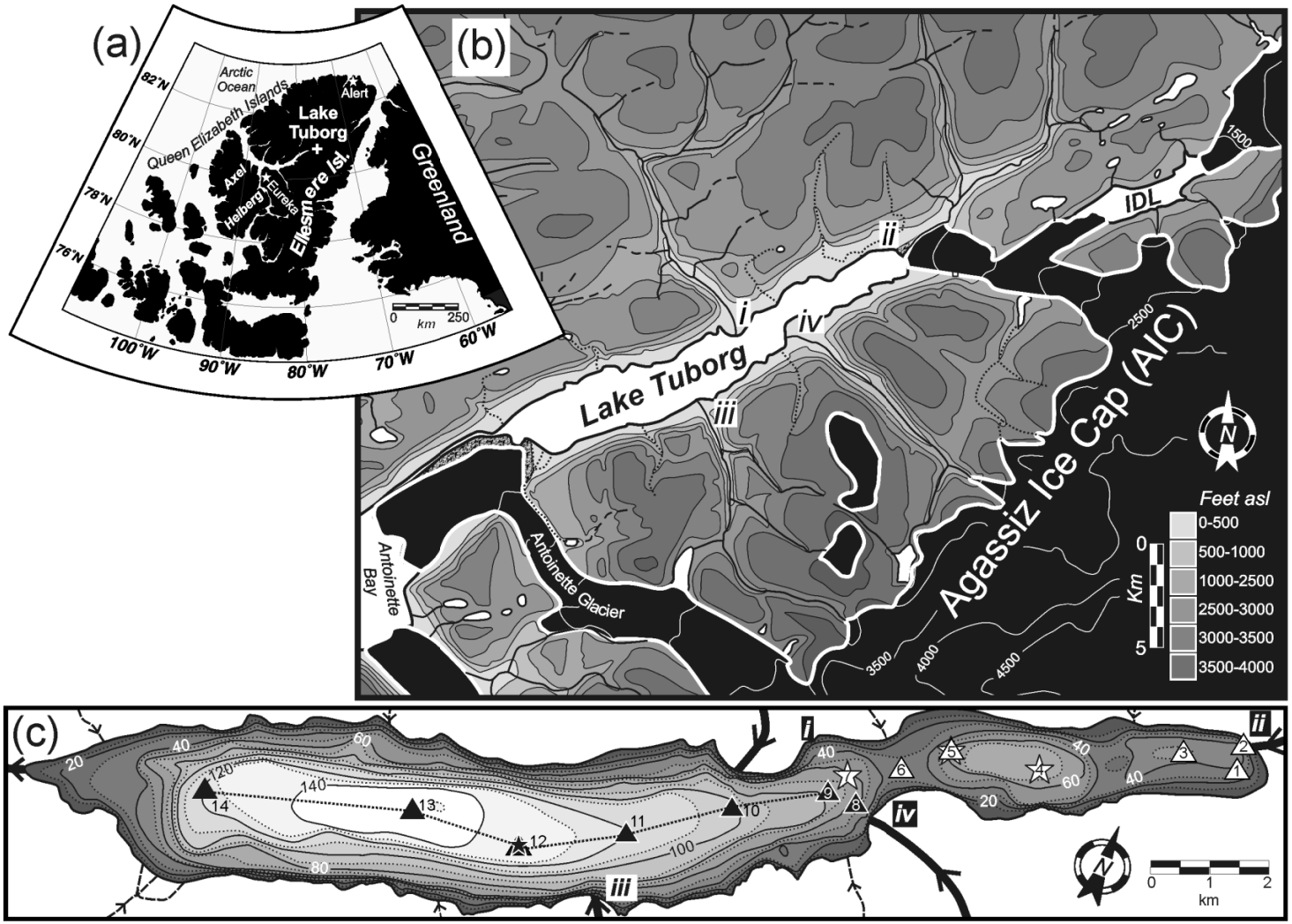

Figure 3.1. (a) Regional map of Ellesmere Island and surroundings in the Canadian High Arctic. (b) Physiography and topography near Lake Tuborg and the ice-dammed lake (IDL). Contour interval is 500 feet; shading is feet asl. (c) Lake Tuborg Bathymetry. Solid bathymetric contours are every 20 m. Core locations are stars; limnologic monitoring stations are triangles. 'i' in 'b' and 'c' is at 80.98°N, 75.555°W.

estuaries (e.g., Geyer and Smith, 1987) and laboratory experiments (e.g., Rimoldi et al., 1996). The regionally unique hydrology and drainage mechanisms of the 2003 jökulhlaup are also described.

3.3 Site description

Lake Tuborg was formed about 3000 years ago when Antoinette Glacier advanced and trapped seawater in the lake (Long, 1967). The lake is in a steep-walled ~450-600 m deep valley at ~11 m asl (Fig. 3.1b). Soils are very thin cryic regosols superimposed on permafrost, and vegetation is very sparse. Lake surface area is 42 km^2, and maximum length and width are 20.9 and 3.4 km, respectively (Fig. 3.1c). There is a large, deep, meromictic basin at the southwest end (maximum depth=~145 m), and a smaller, shallower freshwater basin at the northeast end of the lake (maximum depth=~74 m; Fig. 3.1c). A 34 m deep sill separates the two basins. Lake ice cover is nearly perennial.

A major stream enters Lake Tuborg at '*i*' (throughout the text, *'i'* to *'iv'* refer to locations in Fig. 3.1b). It is entirely fed by snowmelt; peak streamflow occurs in late June, and discharge decreases greatly when watershed snow cover is exhausted shortly afterward. Watersheds above *'iii'* and *'iv'* are extensively glacierized, with higher mean elevations than at *'i'*. This creates higher discharge duration and amount, and higher sediment transport than at *'i'*, but the timing of peak flow is delayed until early to mid-July when peak summer air temperature occurs (Braun et al., 2000). Small supraglacial lakes on the Agassiz Ice Cap quickly drained in July 1995, and discharge and suspended sediment transport briefly, but greatly, increased (Braun et al., 2000). The ice-dammed lake responsible for the 2003 jökulhlaup is part of the watershed above *'ii'*, but the lake captures almost all glacial melt from the catchment while filling, so the streamflow

regime at *'ii'* is normally nival. CTD casts and visual observations at the glacier terminus near *'ii'* show no evidence of subglacial meltwater discharge, even during peak summer melt.

The edge of the Agassiz Ice Cap parallels Lake Tuborg at ~900 m asl (Fig. 3.1b). The Agassiz Ice Cap generally is cold based, and discharge is from supraglacial snow and ice melt; however, outlet glaciers near sea level at the northeast and southwest ends of the lake are warm based (Braun et al., 2000). The ice-dammed lake is dammed by a tributary glacier of the Agassiz Ice Cap that branches into a small valley between 300 and 460 m asl (Fig. 3.1b). Bergs calve into the lake at its northeast and southwest ends, and the glacier dam at the southwest end normally blocks all outflow.

Mean annual air temperature at Eureka (Fig. 3.1a; 10 m asl), the closest Meteorological Survey of Canada weather station to Lake Tuborg, is –20^{o}C, and the only months with average temperatures greater than 0^{o}C are June (2.3^{o}C), July (5.6^{o}C), and August (3.1^{o}C).

3.4 Methods

Monitoring at Lake Tuborg took place continuously from mid May to mid August in 2001-2003. Coring and limnologic monitoring stations are shown on Fig. 3.1c. Air temperature was recorded every 15-minutes near lake level; precipitation was collected at ground level and manually read. Lake level was recorded every 15 minutes (cf. Reedyk et al., 1997). End of season lake level was marked with cairns to ensure a common lake level datum. The lake level recorder could not be used after 21 July 2003 because of shifting ice pans and rapidly rising lake level, so water height after this date was surveyed with a staff and level. The abovementioned measurements were made near '*i*'.

Water column conductivity, temperature, and density were measured with a SeaCat SBE 19 CTD (Table 3.1; Sea-Bird Electronics Inc, Bellevue, WA, USA). Conductivity is reported as specific conductivity in µS/cm, (SpC (µS/cm) = (C * 10,000) / (1 + A * [T – 25]), where (C = conductivity (S/m), T = temperature (° C), A = 0.020; User's Manual for SEASOFT-Win32: SBE Data Processing, 2005), temperature is reported as potential temperature (T_θ), and density is potential density (σ_θ) referenced to surface pressure. Brunt-Väisälä frequency (N^2) is a measure of density stratification and resistance to mixing (Wüest and Lorke, 2003), and is calculated with 1 m depth bins. CTD casts were plotted in *Ocean Data View* (Schlitzer, 2005). A damaged connector prevented the CTD from being lowered deeper than ~80 m in 2003. Dissolved oxygen was measured with a Hydrolab DataSonde 4a (Hach Company, Loveland, CO, USA).

Table 3.1. Manufacturer-stated and drift-inferred temperature and conductivity accuracies for the SBE19 Sea-Cat CTD. Drift-inferred accuracy is maximum sensor drift between factory calibrations, performed prior to the 2001-2003 field seasons. Drift-inferred conductivity cell accuracy was always better than manufacturer-stated accuracy (45 µS/cm < (10 µS/cm/month x ~12 months)). Conductivity cell drift is negligible when the sensor is not being used (D. Murphy, personal communication, 2004).

Parameter	Drift-Inferred	Manufacturer-Stated
Temperature (°C)	0.0084°C	0.01°C/6 months
Conductivity (µS/cm)	45 µS/cm	10 µS/cm/month

Transmissivity is measured in percent with a Sea Tech transmissometer (Sea Tech Inc, Corvallis, OR). When transmissivity is >10%, it is transformed to suspended sediment concentration (SSC). However, transmissivity from the saltwater layer is not transformed (Fig. 3.2).

Sediment cores were obtained with an Ekman dredge. Thin-sections were prepared by following procedures in Francus and Asikainen (2001). Grain size was determined by SEM image analysis of thin sections (Table 3.2; Francus, 1998). Grain size is presented as 'equivalent disc diameter' (EDD; Francus 1998). Virtually no microorganisms were present. Mean grain size was calculated every 500 µm along thin section photomosaics.

Table 3.2. Image analysis equipment, settings, and software.

Parameter	Details
Microscope model	JEOL JSM-5410 backscattered electron microscope (JEOL Inc., Tokyo, Japan)
Magnification	100x
Beam strength	20 kv
Working distance	20 mm
Image analysis software	ImageJ (Rasband, 1997-2006)
Image resolution and format	2560x1920 pixel (each pixel represents 0.5 µm), grayscale, uncompressed TIF
Minimum resolvable grain size	2 µm (Sorreghan and Francus, 2004)
Algorithms used	'enhance contrast', watershedding (manually checked), thresholding (manual), 'fill holes'

Three hundred and three bathymetric soundings were obtained in Lake Tuborg. Ice-dammed lake dimensions were determined with an aerial photograph (a-16687-47, ~1:60000, taken July 1959).

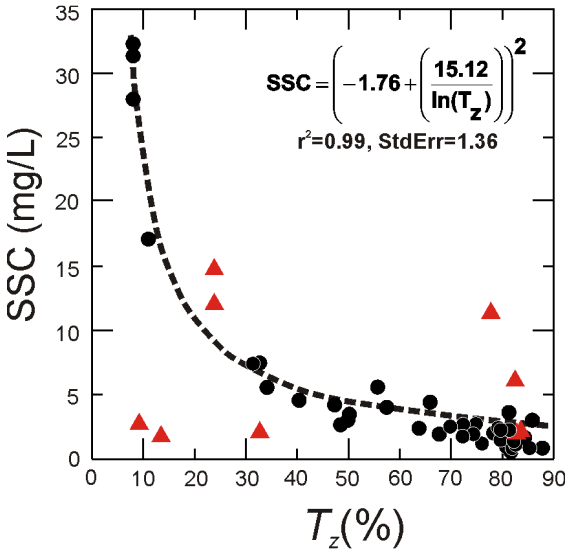

Figure 3.2. Relationship between transmissivity (T_z, %) and suspended sediment concentration (SSC, mg/L). SSC was determined by vacuum filtration through 0.45 µm Whatman Type WCN filter papers that were individually pre- and post- weighed. Van-Dorn water samples were obtained at varying depths, locations, and times in the mixolimnion (black circles) and monimolimnion (red triangles). Samples from the monimolimnion are outliers, and were excluded from the regression because T_z is most sensitive to <20 µm diameter particles that typically form >1 mm flocs in salt water (Hill, 1998), and the large dissolved load of the monimolimnion reduces T_z.

3.5 Results

3.5.1 Climate and weather

From 28 May to 10 August, 2001 to 2003, daily air temperatures at Eureka and Lake Tuborg are highly correlated (r^2=0.79, slope=0.84), with mean air temperature differences within 0.4°C in all years. In 2001 and 2002, melting degree-days at Lake Tuborg were very similar to the 1948-2002 Eureka mean melting degree-days, but 2003 Lake Tuborg melting degree-days were 23% greater (Fig. 3.3). Much of the anomalous warmth in 2003 occurred in July. Mean Eureka air temperature from 3-18 July was 4°C higher than the 1948-2002 mean for the same period. 2003 was the 10th warmest summer on record (1947-2003), with 435 melting degree-days. 37.5 mm of rain fell at Eureka in 2003: the 38th percentile for the 1948-2003 record. Only 28 mm fell at Lake Tuborg during monitoring in 2003, and no rain fell for over a month prior to the jökulhlaup.

3.5.2 Lake level, discharge and jökulhlaup observations

Lake level in all years began increasing in mid-June (Fig. 3.5) shortly after mean daily air temperature at lake level increased above freezing. Lake level was unusually high beginning in early July 2003. In early to mid July, the ice-dammed lake overflowed between the Agassiz Ice Cap to the south and bedrock to the north (Fig. 3.4). Water flowed over an ice ledge, eroding boulder-sized pieces of ice. These ice blocks were then transported to the outwash plain at '*ii*', where they conglomerated into ice rafts (Fig. 3.4). Sediment laden ice rafts detached from shore and floated around the freshwater basin as lake level continued to rise (Fig. 3.6a). No 'leaking' (Gilbert 1971) of the ice-dammed lake was observed near the glacier terminus. Lake Tuborg lake level decreased by ~0.75 m between 16 and 22 July (Fig. 3.5) after air temperatures fell following their peak on 4 July (Fig. 3.3).

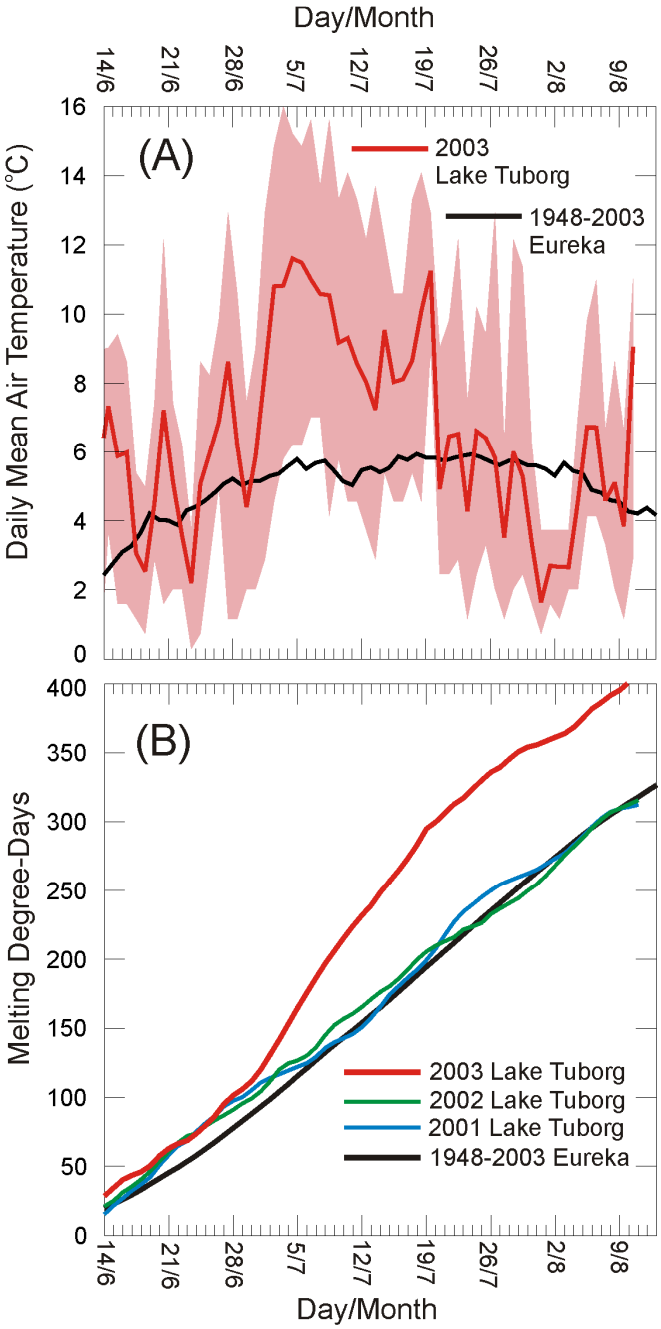

Figure 3.3. Air temperature at Eureka (10 m asl) and Lake Tuborg (~12 m asl). (a) Red line is 2003 Lake Tuborg daily mean air temperature, shading encompasses daily maxima and minima. Black line is 1948-2003 mean daily air temperature at Eureka. (b) Cumulative melting degree-days (MDD) from 2001-2003 at Lake Tuborg, and 1948-2003 mean at Eureka.

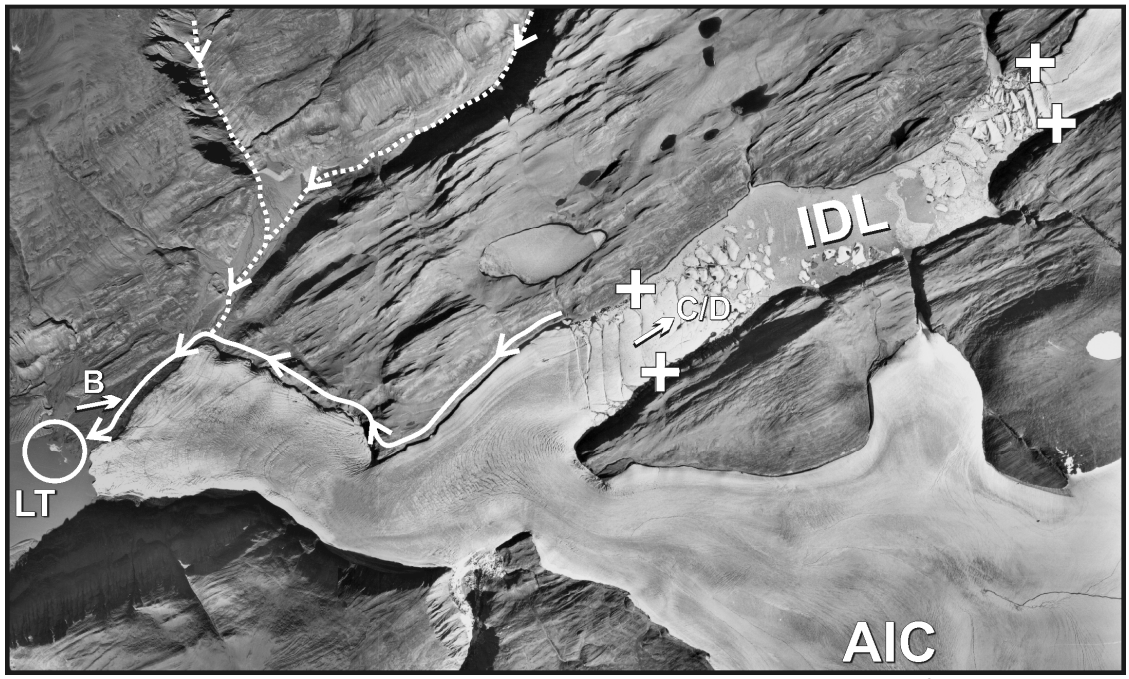

Figure 3.4. The Agassiz Ice Cap (AIC), ice-dammed lake (IDL), and Lake Tuborg (LT) from aerial photographs a-16687-47 and a-16977-63. Dotted lines mark channels that usually feed the northeast basin of LT, and the solid line represents the IDL overflow route. An 'ice raft' in LT on 2 August 1960 is circled. Arrows at 'B' and 'C/D' correspond to the locations and directions of photographs shown in Fig. 3.6. Crosses are the assumed northeast and southwest boundaries of the IDL. Scale is variable due to parallax, but the mosaic is about 15x9 km, and north is up.

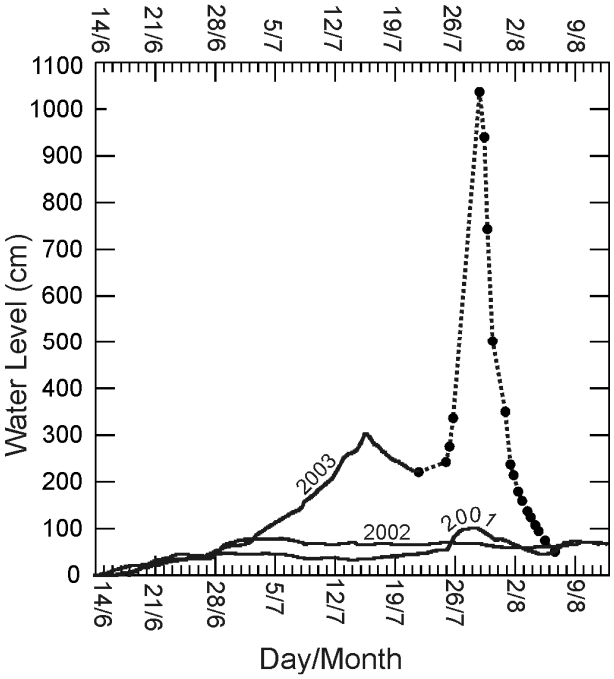

Figure 3.5. Lake Tuborg 2001-2003 lake level. Solid lines are automatically logged stilling well data. Circle symbols are lake heights determined with a staff and level.

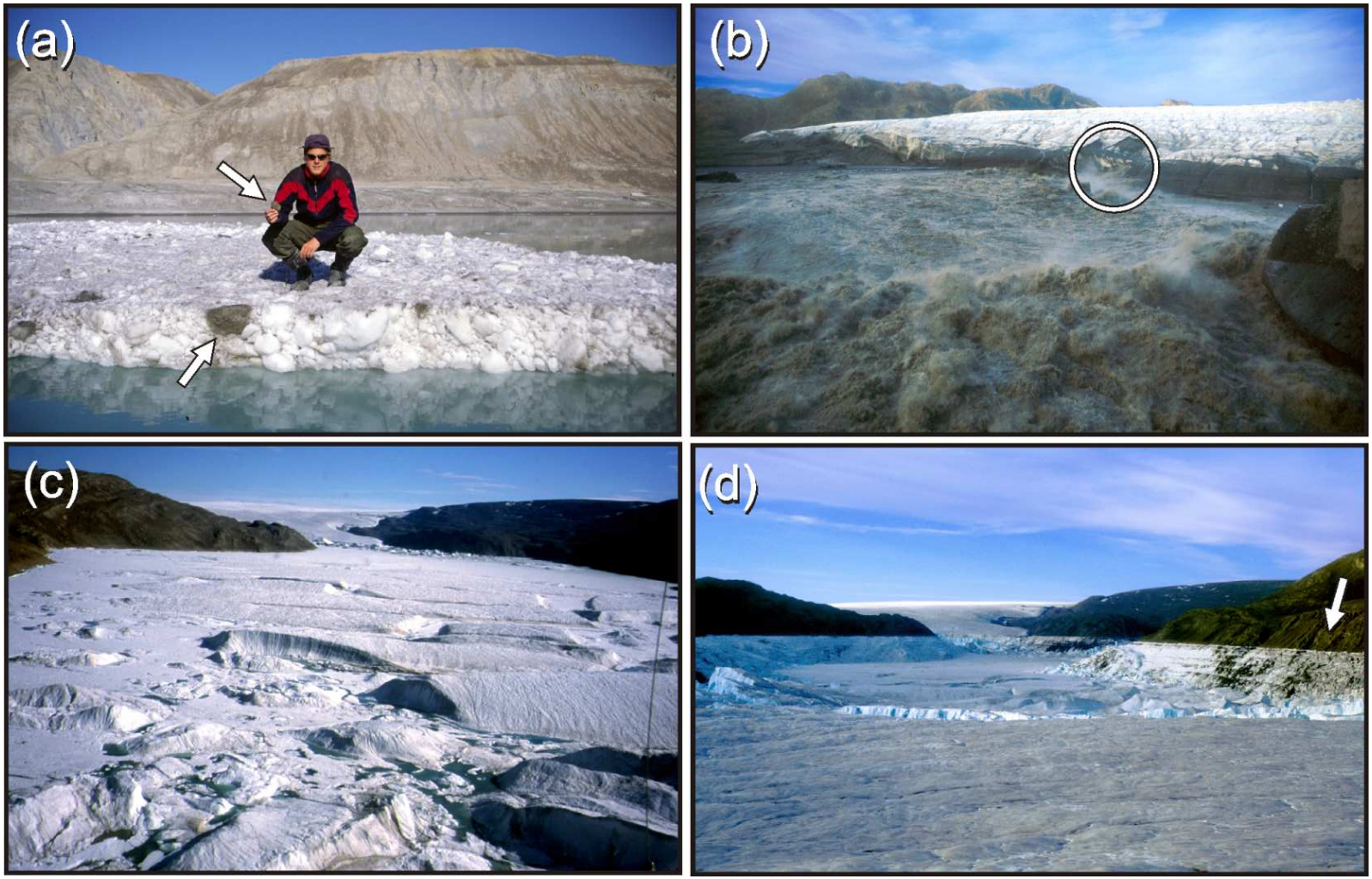

Figure 3.6. Photographs from Lake Tuborg and the ice-dammed lake (IDL) in 2003. (a) Ice raft; arrows point to a large clast and an ice boulder coated in fine-grained sediment. (b) The jökulhlaup on 28 July, with the portal circled. (c) Full IDL on 18 July. (d) Largely empty IDL on 28 July. Note the 'ice rims' below the arrow. Locations for 'b', 'c' and 'd' are shown in Fig. 2. Photos are courtesy of Anders Romundset.

The ice-dammed lake catastrophically burst, dramatically raising lake level by 7.6 m from 25 July 08:00 to 28 July 20:00 (Fig. 3.5). 3.2 x 10^8 m^3 of water is necessary to increase the Lake Tuborg lake level by this amount, and this provides a minimum estimate of the jökulhlaup volume (see *Discussion*). The rate of lake level increase requires that average discharge into Lake Tuborg for this period exceeded 1040 m^3/s.

The jökulhlaup volume can also be estimated assuming the ice-dammed lake morphology is ½ of an ellipsoid. The length, width, and maximum depth of the ice-dammed lake are 6 km, 1.5 km (Fig. 3.4), and 116 m, producing a volume of 5.5 x 10^8 m^3. 1959 boundaries are broadly similar to those of 2003, based on GPS waypoints obtained at the ice-dammed lake perimeter. Prominent 'ice-rims' on the empty ice-dammed lake walls were observed by helicopter on 28 July (Fig. 3.6d). The elevation difference between the uppermost ice-rim and the bottom of the drained ice-dammed lake was 116 m, providing the maximum depth.

Discharge issued from a newly developed glacier portal 980 m from the Lake Tuborg shore (Fig. 3.6b). When the jökulhlaup ended, the portal was ~50 m diameter. The outwash plain near '*ii*' prograded, and Lake Tuborg is now almost completely isolated from the northeast glacier (cf. 1959 photo in Fig. 3.4). Englacially eroded ice blocks floated as bergs in the freshwater basin during and after the event.

Maximum discharge (Q_{max}) from subglacially draining jökulhlaups is related to the volume drained (V_t, x10^6 m^3), where $Q_{max}=46(V_t)^{2/3}$ (Clague and Mathews, 1973; Walder and Costa, 1996). Q_{max} using the Lake Tuborg lake level V_t is 2200 m^3/s, and Q_{max} using the V_t from ice-dammed lake morphology is 3150 m^3/s (see *Discussion*).

3.5.3 Limnology and sedimentary processes before the jökulhlaup

3.5.3.1 The Northeast, freshwater basin

Before each melt season began, the upper water column (epilimnion) was inversely thermally stratified, and bottom waters (hypolimnion) were relatively warm (e.g. Fig. 3.7, 30 May cast). The water column was nearly isohaline, bottom water was ~50 mg/L more dense than near surface water (Fig. 3.7; 30 May cast), and N^2 at the lower thermocline was 4.1 x 10^{-5} s^{-2}, representing somewhat weak resistance to mixing (cf. Wüest and Lorke, 2003).

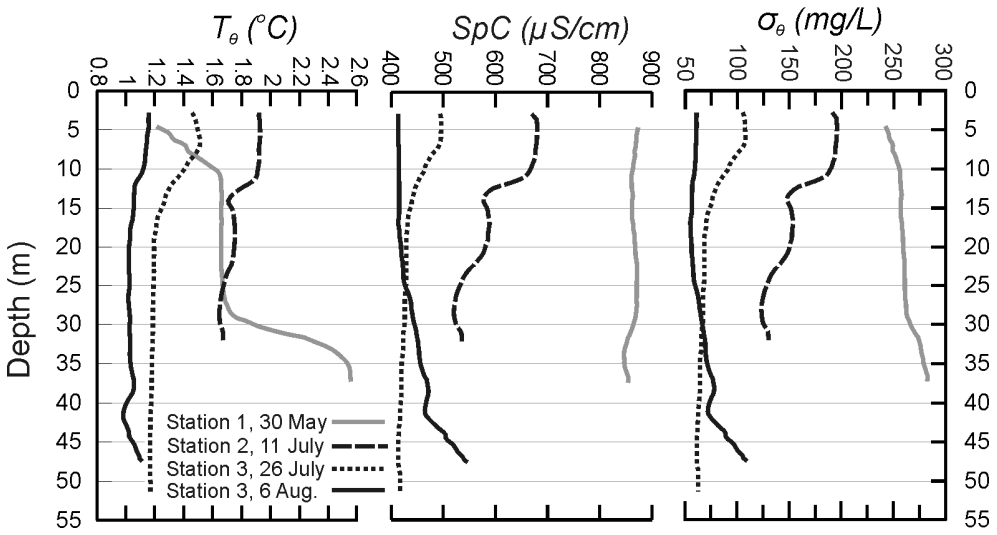

Figure 3.7. Freshwater basin CTD casts from before, during, and after the jökulhlaup in 2003. Potential temperature (T_θ), specific conductivity (SpC), and potential density (σ_θ).

During the period when the ice-dammed lake was overflowing, the water column was significantly fresher than in the pre-melt season (Fig. 3.7, 11 July cast). There was a maximum density inversion of 72 mg/L. Water samples at 10 m, and near bottom at 30 m had 47 and 218 mg/L SSC, respectively.

One day before the jökulhlaup began (24 July 2003), two CTD casts were performed on the sill and in the freshwater basin (Fig. 3.8, Stations 5 and 6). Casts were obtained 10 minutes apart, and stations are separated by 1 km. There was no hypolimnion in the freshwater basin. The

water column cooled and freshened with depth, producing a density inversion of 88 mg/L. SSC was >23 mg/L through most of the water column. By contrast, on the sill, near-bottom water was significantly warmer, had higher specific conductivity, and was much denser than in the freshwater basin. SSC only reached 16 mg/L in a 5 m thick overflow (Fig. 3.8, Station 6).

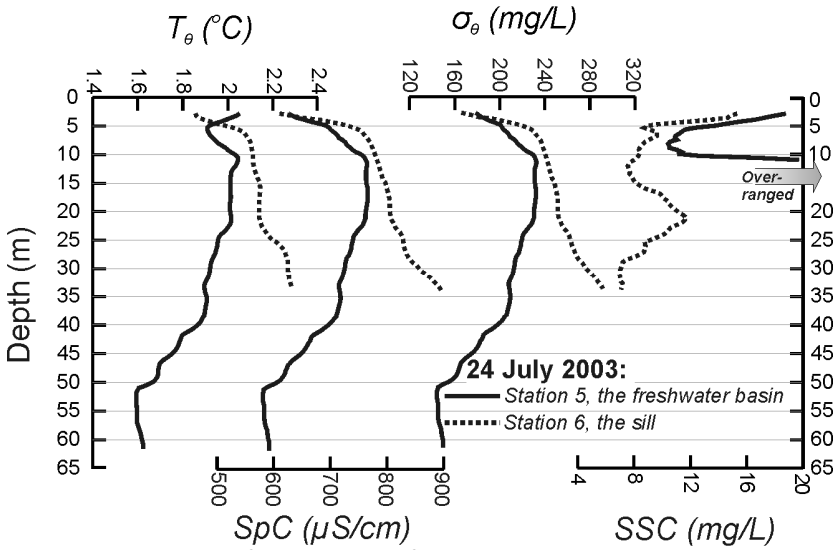

Figure 3.8. CTD casts from the day before the jökulhlaup began (24 July 2003) in the freshwater basin (Station 5) and on the sill (Station 6). Potential temperature (T_θ), specific conductivity (SpC), potential density (σ_θ), and suspended sediment concentration (SSC).

3.5.3.2 The Southwest, meromictic basin

Before the jökulhlaup in the saltwater basin, specific conductivity in the upper freshwater layer (mixolimnion) was ~900 µS/cm, and specific conductivity in the deeper saltwater layer (monimolimnion) was ~41 850 µS/cm (~25.01 PSU; Fig. 3.9). The extremely sharp and strong chemocline creates an abrupt ~20 000 mg/L density contrast between salt and freshwater, and ~0.06 s^{-2} N^2. Wüest and Lorke (2003) cite 0.1 s^{-2} as a typical maximum N^2 in lakes. Before the 2003 melt season began, dissolved oxygen was 10.5-12 mg/L from the surface to 58 m, and dropped to <1 mg/L below 60.5 m.

A sharp decrease to ~5% T_z consistently occurs near the chemocline (Figs. 3.9, 3.10, 3.11). Seven Van Dorn water samples were obtained from 50-59 m in late May 2003, and SSC

was always <2.5 mg/L. From the T_z calibration, SSC should have been extremely high (Fig. 3.2; see *Discussion*).

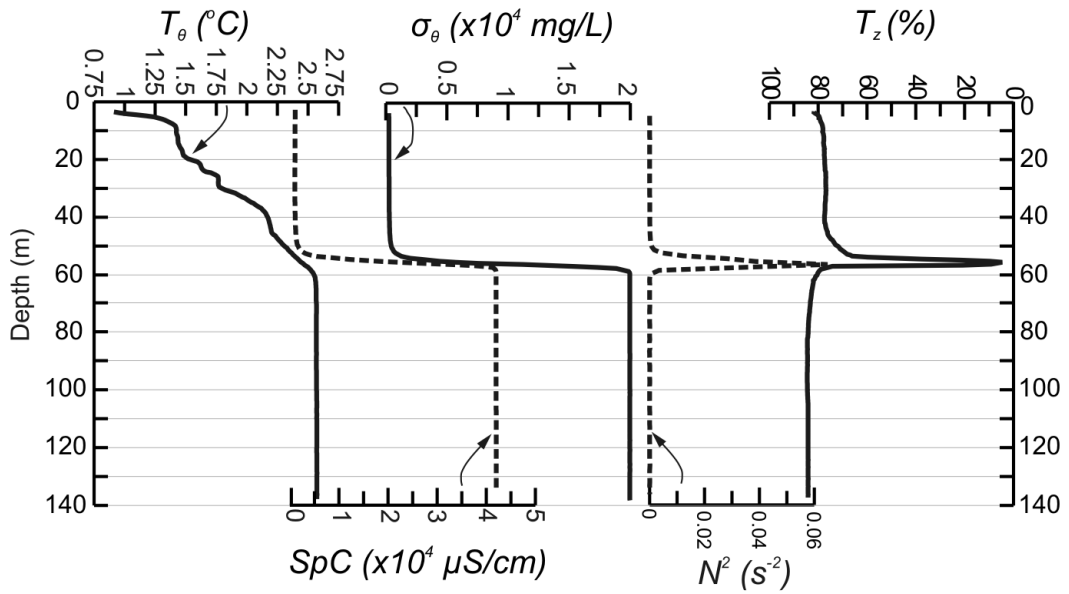

Figure 3.9. CTD cast from the meromictic basin (Station 13) before the jökulhlaup (10 June 2001): potential temperature (T_θ), specific conductivity (SpC), potential density (σ_θ), Brunt-Väisälä frequency (N_2), and beam transmissivity (T_z; note the reversed x-axis).

3.5.3.3 Response to slush flow events

In 2001, 2002, and 2003, small supraglacial lakes on the Agassiz Ice Cap drained, transporting large volumes of slush and sediment into Lake Tuborg near *'iv'* (cf. Braun et al., 2000). From late May to mid July 2003, CTD casts were repeatedly performed close to inflow near *'iv'* (Fig. 3.10a, Station 8). Before early July, discharge was only from unglaciated terrain at lower watershed elevations, and water column turbidity was <2.5 – 4 mg/L (Fig. 3.10a). Beginning on 3 July, discharge and sediment transport increased dramatically, and strong interflows formed at 25 and 48 m (Fig. 3.10a). The upper water column became increasingly turbid from the bottom up from 3-16 July (Fig. 3.10a).

During peak inflow at '*iv*', several casts were also performed farther from the delta, to determine the extent of processes derived from slush-flows in the meromictic basin (Fig. 3.10b, Station 9). On 8 July, the transmissometer was overranged below 30 m (Fig. 3.10b), but a near

bottom Van Dorn sample contained 70 mg/L SSC. The next day at the same location, the water column was significantly less turbid between 20-45 m, and beneath the chemocline (Fig. 3.10b).

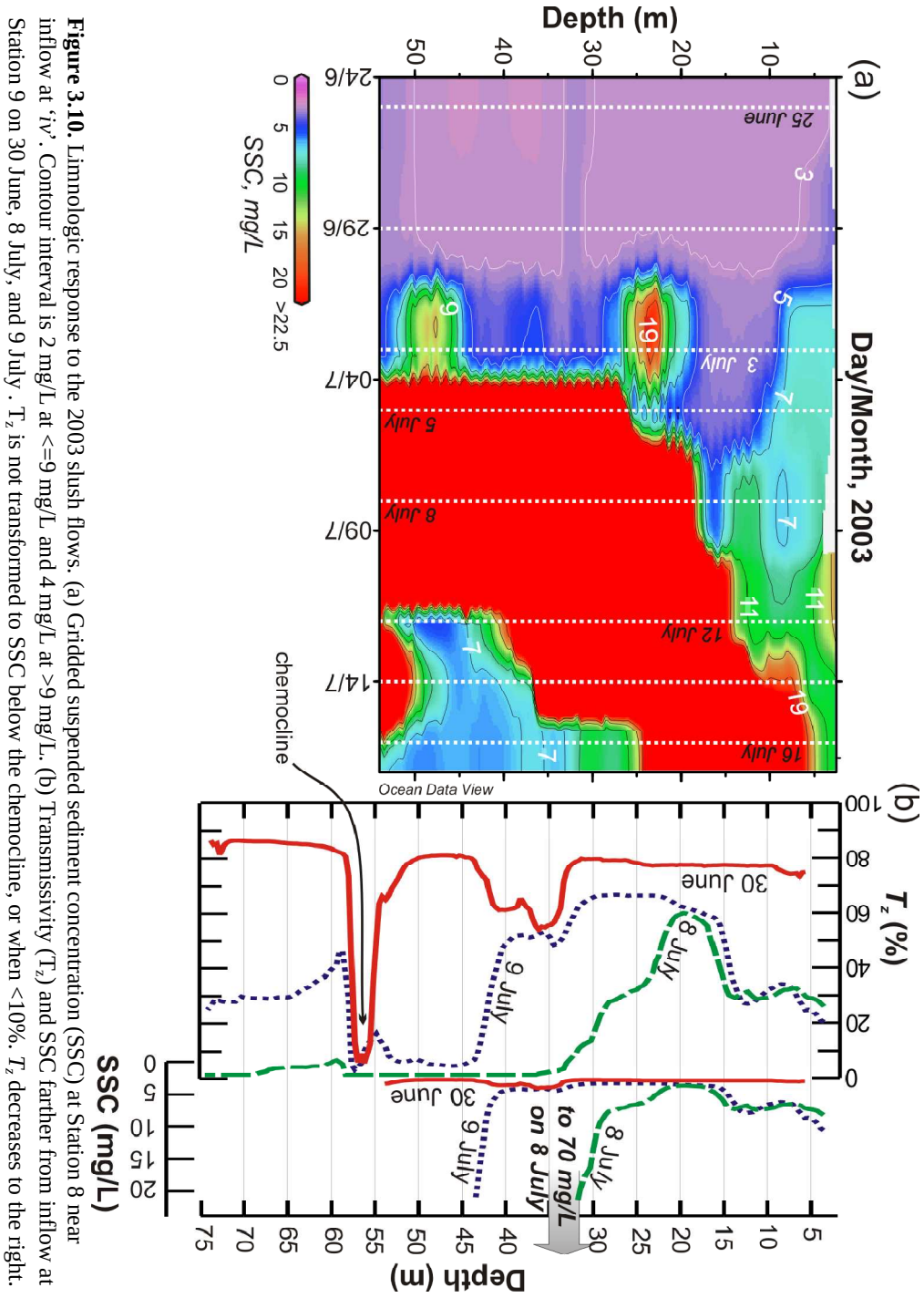

Figure 3.10. Limnologic response to the 2003 slush flows. (a) Gridded suspended sediment concentration (SSC) at Station 8 near inflow at 'iv'. Contour interval is 2 mg/L at <=9 mg/L and 4 mg/L at >9 mg/L. (b) Transmissivity (T_z) and SSC farther from inflow at Station 9 on 30 June, 8 July, and 9 July . T_z is not transformed to SSC below the chemocline, or when <10%. T_z decreases to the right.

Inflow at *'iv'* significantly dropped beginning on 13 July, and continued to wane through the remainder of the melt season. SSC was extremely high at Station 8 (near inflow at *'iv'*) until 12 July, then the lower water column began to freshen (Fig. 3.10a). The water column cleared from the bottom up, and freshening continued until profiling ended on 16 July (Fig. 3.10a). Specific conductivity below the chemocline decreased by ~100 µS/cm near inflow at *'iv'* following the 2003 slush flow events.

3.5.3.4 Limnology during and after the jökulhlaup

During and after the jökulhlaup in the freshwater basin, near bottom water samples were very turbid. At Station 3 on 26 July, near bottom SSC was 77 mg/L; at Station 4 on 28 July, SSC was 1093 mg/L.

After the jökulhlaup in the saltwater basin, a strong overflow was present in the epilimnion, extending ~9 km from the beginning of a transect near the sill (Figs. 3.11a; 3.1c). Close to the sill, turbid plumes extended as far as ~3 km above and below the chemocline. A very distinct 'cold stratum' was present between ~35 m and the chemocline (Fig. 3.11b; cf. Phelps, 1996). The epilimnion warmed with distance from the sill.

Pre- and post jökulhlaup temperature and specific conductivity in the meromictic basin are compared in Fig. 3.12. The 'cold stratum' was not present as late as 16 July 2003 (Fig. 3.12a). Although the cold stratum was less thermally dense than the overlying, warmer, epilimnion (Fig. 3.12a), the thermal density deficit was overcome by saltier, more dense water in the lower mixolimnion compared to pre-jökulhlaup conditions (Fig. 3.12b). When the post-jökulhlaup lower mixolimnion is visualized in a vertical section, specific conductivity is seen to slightly decrease with distance from the sill (Fig. 3.13b).

The post-jökulhlaup monimolimnion specific conductivity was ~550 µS/cm lower, and temperature was ~0.04°C lower compared to pre-jökulhlaup conditions recorded in June 2001 (Fig. 3.12c, d). As late as 16 July 2003, the monimolimnion was ~2.57 °C, and specific conductivity was ~41 800 µS/cm (Fig. 3.12c, d).

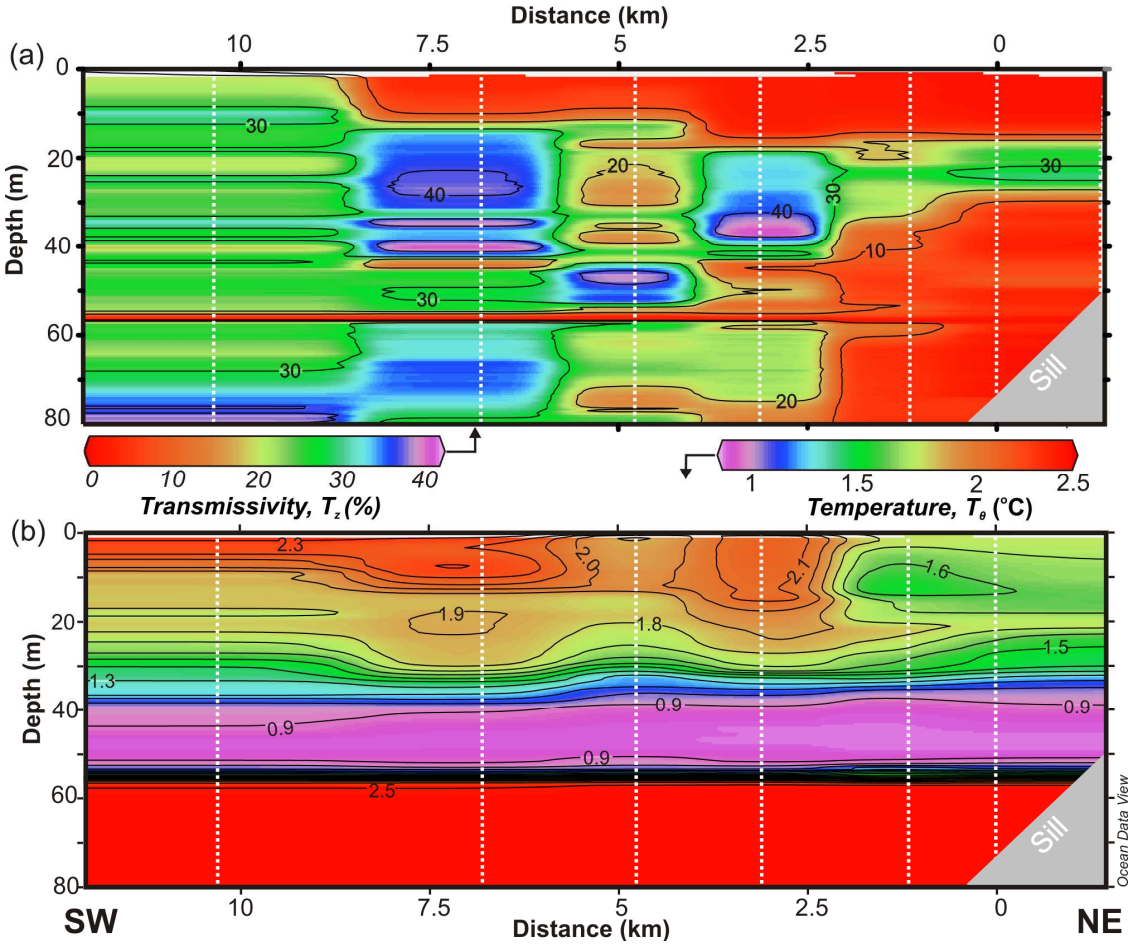

Figure 3.11. Post-jökulhlaup (9 August) vertical sections from Stations 9-14 (dotted line in Fig. 3.1c) in the upper 80 m of the meromictic basin. (a) transmissivity, T_z, and (b) potential temperature, T_θ. Contour interval is 10% for T_z, and 0.1°C for T_θ. Casts are vertical dashed lines. Isolines are very closely spaced at the chemocline temperature gradient.

Downlake temperature and specific conductivity variation in the monimolimnion along the ~10 km saltwater basin transect were extraordinarily low less than two weeks after the jökulhlaup ended (<88 µS/cm and <0.003°C).

Dissolved oxygen in the mixolimnion was ~1 mg/L higher in the cold stratum compared to casts from the same location earlier in the melt season. The monimolimnion was not significantly oxygenated by the jökulhlaup.

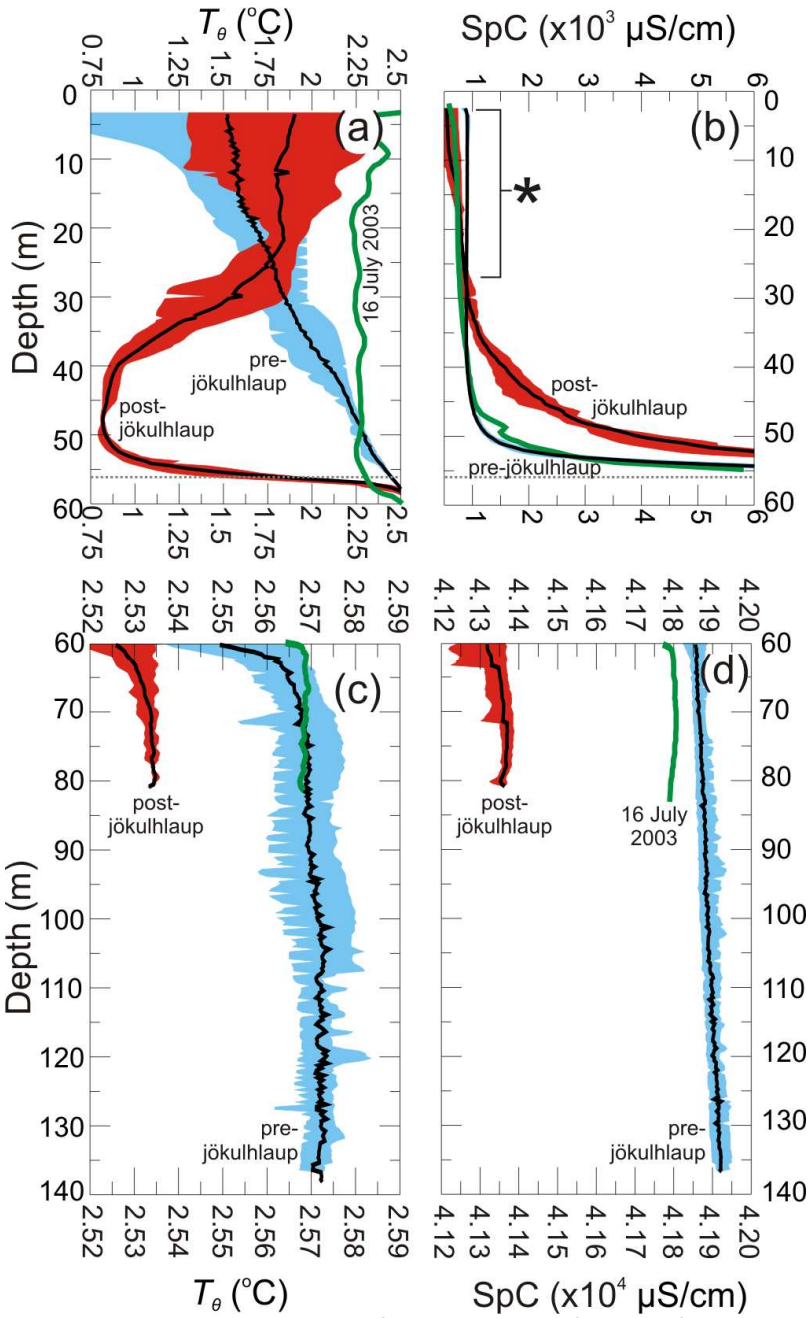

Figure 3.12. Temperature and specific conductivity before and after the jökulhlaup in the saltwater basin. Potential temperature (T_θ ; 'a', 'c') and specific conductivity (SpC; 'b', 'd') in the meromictic basin before (blue shading) and after (red shading) the jökulhlaup. Shaded regions encompass maximum and minimum values for each series; solid lines are means. The blue-shaded pre-jökulhlaup series consists of 24 casts from 8-24 June 2001, and the red-shaded post-jökulhlaup series consists of seven casts *(continued)*

(one from 7 August, and six from 9 August 2003). Post-jökulhlaup casts were completed after lake level regressed, and lake level was very similar in both series (Fig. 3.5). The green line is the last cast in the meromictic basin prior to the jökulhlaup, completed on 16 July 2003. Note that abscissa scales on sub-panels showing monimolimnion parameters ('c', 'd') are very different from abscissa scales showing mixolimnion parameters ('a', 'b') to better illustrate subtle post-jökulhlaup cooling and freshening of the monimolimnion.

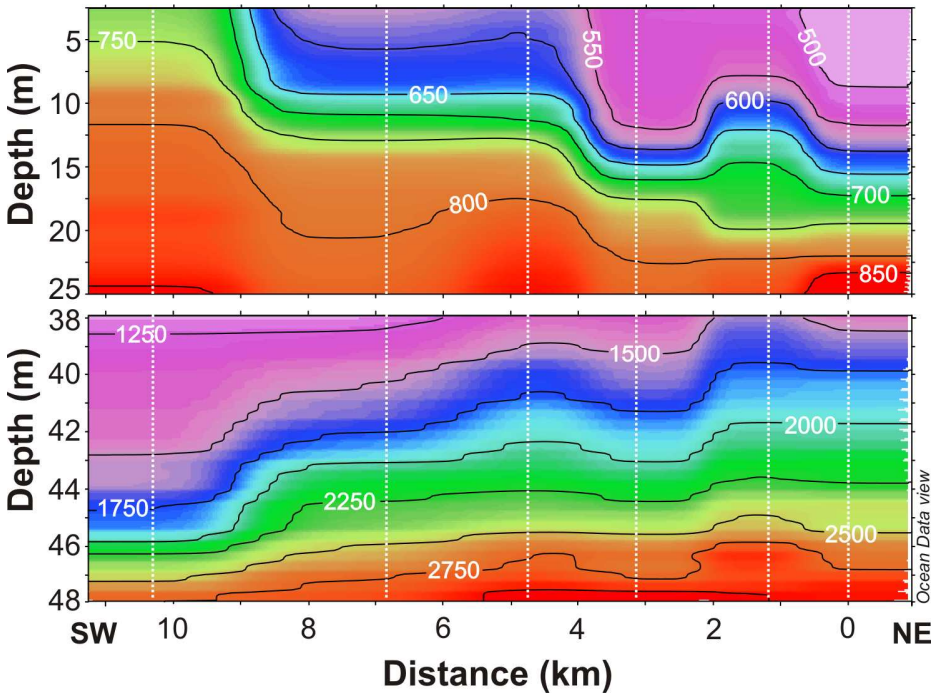

Figure 3.13. Specific conductivity (SpC) vertical sections from after the jökulhlaup on 9 August (Stations 9-14; dotted line in Fig. 3.1c) at two depth ranges. Contour interval is 50 µS/cm in 'a', and 250 µS/cm in 'b'. Note the greater vertical exaggeration for the lower section. Vertical dashed lines are CTD casts.

3.5.3.5 Near surface sediments

Before the jökulhlaup, at the end of the period when water was overflowing from the ice-dammed lake (21 July 2003), a surface core was obtained at Station 4 in the freshwater basin. At the base of the core, five centimeter-scale units with coarse bases grade upward (Fig. 3.14a '*V1-V5*'). Sediment above ~80 mm is somewhat coarser grained, and is less noticeably laminated than sediment below 80 mm. However, three units fine upward, and inter-unit grain size coarsens upwards (Fig. 3.14a '*F1-F3*').

After the jökulhlaup, on 5 August, another surface core was obtained at the same location (Fig. 3.14b). Laminae are distinctly angled below 95 mm, fine upward, and are relatively coarse. Several dark very fine-grained lenses are present below ~120 mm (Fig. 3.14b '*RU*'), and one has apparently folded internal structure (Fig. 3.14b '*RU-F*'). Sediment is nearly massive above ~95 mm, but very gradually fines upward.

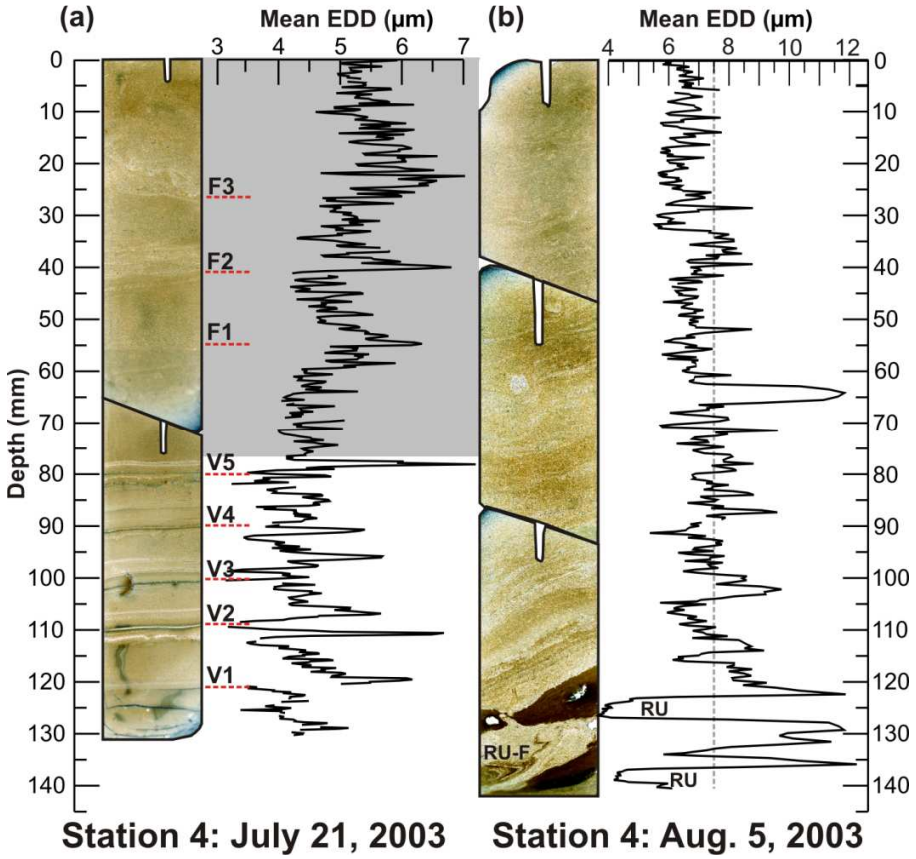

Figure 3.14. Ekman cores obtained from the same location before and after the jökulhlaup. Coring location is Station 4, depth is 74 m. (a) Thin sections and grain size from a core obtained on 21 July 2003. Sediment that was likely deposited during the period of ice dammed lake overflow is shaded. V; clay cap; F, bottom of fining upward cycle. (b) Thin sections and grain size from a core obtained on 5 August 2003. RU, rip-up; RU-F; folded rip-up. Images are flatbed scans of thin sections under cross-polarized light, with contrast and brightness enhanced to better illustrate structures. EDD is equivalent disk diameter (Francus, 1998).

Surface cores were also obtained on the freshwater and saltwater sides of the sill after the jökulhlaup (Fig. 3.15a, b; Stations 5 and 7). Both cores are from roughly the same water depth (62-63 m), and coring stations are 2 km apart. On the freshwater side, sediments are very fine grained and dense: repeated coring with a weighted Ekman dredge failed to recover more than

~33 mm (Fig. 3.15a). In the core from the saltwater side, there are laminae below ~85 mm, but no clay caps. Texture coarsens upward above 85 mm, but abruptly fines at about 30 mm, above which sediment is massive and slightly fines upward (Fig. 3.15b).

At a much more distal location, four cores were obtained within ~50 m of each other in 2003 in ~135 m water depth (Fig. 3.16, Station 12). All cores except 'K' were obtained before the jökulhlaup. The lowermost 60 mm of the stratigraphy (160-220 mm) is largely massive, fine-grained, and slightly fines upward. Sediments above about 160 mm are somewhat coarser, irregularly laminated, and of variable grain size and thickness. Midway through core 'K', there is a sharp contact, above which sediment are much more coarse, and fine upward.

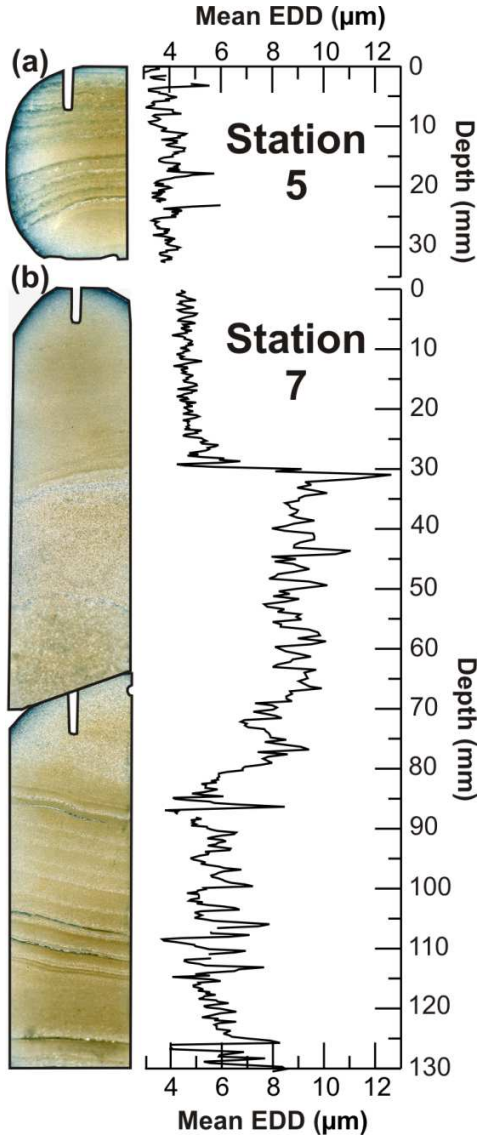

Figure 3.15. Ekman cores from both sides of the sill obtained after the jökulhlaup (11 August). Both cores were taken in 62-63 m water depth. (a) Thin sections and grain size of a surface core obtained on the freshwater side of the sill at Station 5. (b) Thin sections and grain size of a surface core obtained on the saltwater side of the sill at Station 7. Images are flatbed scans of thin sections under cross-polarized light, with contrast and brightness enhanced to better illustrate structures. EDD is equivalent disk diameter (Francus 1998).

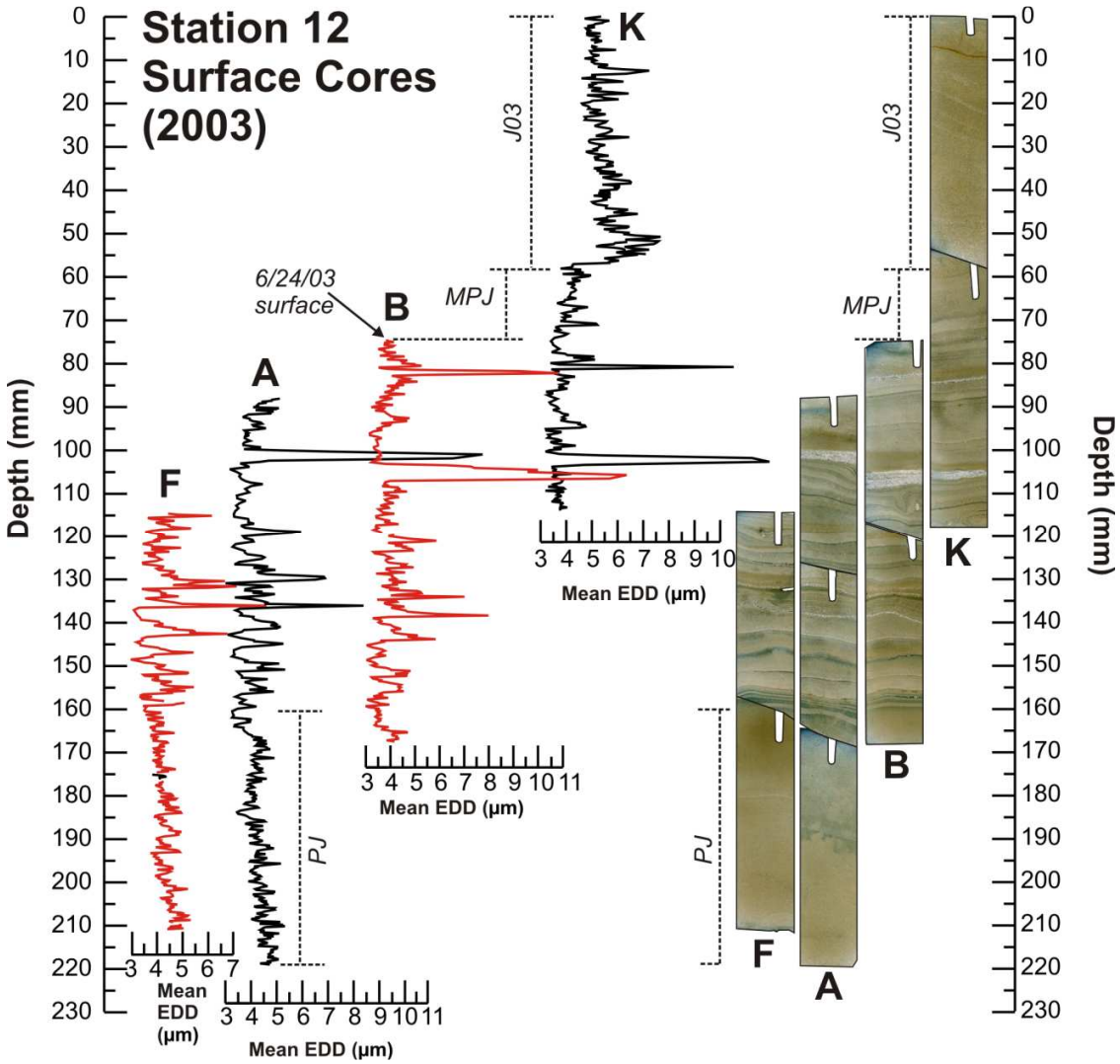

Figure 3.16. Stratigraphy of Ekman cores and grain size from a ~135 m deep, distal location in the meromictic basin (Station 12). All cores except 'K' were obtained before the jökulhlaup in 2003. *J03* is sedimentation from the 2003 jökulhlaup, *MPJ* is minimum 2003 sedimentation prior to the jökulhlaup, and *PJ* is likely the top of the previous jökulhlaup deposit. The sediment surface in 'A' and 'F' was purposely lost to retrieve cored sediments deeper than ~13 cm (the length of the subsampling tubes). The last core obtained prior to the jökulhlaup was 'B', on 24 June. Images are flatbed scans of thin sections under cross-polarized light, with contrast and brightness enhanced to better illustrate structures. EDD is equivalent disk diameter (Francus, 1998).

3.6 Discussion

3.6.1 Jökulhlaup hydrology

Overtopping of the ice-dammed lake likely contributed greatly to the anomalously high lake levels before the jökulhlaup in early to mid July 2003 (Fig. 3.5). The lake level decrease after mid July occurred after air temperature (Fig. 3.3) and glacial melt declined, so less overtopping of the ice-dammed lake likely occurred. In 2003, rainfall runoff did not significantly contribute to ice-dammed lake filling, overtopping, or trigger the jökulhlaup.

The jökulhlaup was likely triggered by ice-dam flotation, which theoretically occurs when ice-dammed lake depth exceeds 90% of the ice-dam height; however, dam overtopping occurred prior to the jökulhlaup, probably because of dry-based glacier bed adhesion (Roberts, 2005). The event likely ended when lake level fell below outlet conduits, the englacial tunnel system was sealed by mechanical blockage, or cryostatic pressure sealed the conduits (Roberts, 2005).

Of 125 ice-dammed lakes studied near Expedition Fiord, Axel Heiberg Island (Fig. 3.1a), most drained incompletely by overtopping their dams (Maag, 1969). The only other ice-dam flotation jökulhlaup observed in the High Arctic ended by ice dam resettling, and the lake did not completely drain (Blachut and McCann, 1981).

The jökulhlaup was the largest recorded in Canada since about 1947 (cf. Clague and Evans, 1994; Geertsema and Clague, 2005), and the actual volume drained was likely more than the two jökulhlaup volume estimates. Volume calculation using the level of Lake Tuborg does not account for discharge out of Lake Tuborg, which was extreme during the event. Discharge into Lake Tuborg from sources other than the jökulhlaup is also not accounted for. However, watershed snowpack was largely exhausted for about a month prior to the jökulhlaup, and air

temperature fell after 19 July, so discharge at *'i', 'iii',* and *'iv'* was very low. The morphologic volume estimate is also likely low, since large floating ice wedges (Maag, 1969; Blachut and McCann, 1981) exist at both ends of the ice-dammed lake, and its length was estimated conservatively (Fig. 3.4).

The depth of the ice-dammed lake is precise, since ice-rims on the empty lake walls clearly showed maximum lake level (Fig. 3.6d). Ice-rims likely formed as the lake drained, when ice was draped on wave- or ice-cut terraces created in ice-dammed lake filling cycles (Maag, 1969).

Underestimating the jökulhlaup volume would result in an underestimation of maximum discharge. However, if the glacier near the ice-dammed lake is cold based, the calculated maximum discharge might be too high, since the Clague-Mathews relationship was determined from warm based jökulhlaups (Walder and Costa, 1996).

3.6.2 Processes and deposits in the northeast, freshwater basin

Varves typically accumulate in the freshwater basin. In summer, heightened air temperature raises the Agassiz Ice Cap freezing level, increases glacial discharge and sediment flux to Lake Tuborg (Braun et al., 2000), and turbid sediment plumes disperse sediment through the lake, forming relatively thick and coarse laminae. In winter, fluvial input stops, and clay-sized particles settle very slowly out of suspension, forming a thin clay layer that defines an annual couplet. Water depth at the freshwater basin coring location is deeper than wave base (Håkanson and Jansson, 1983), and the temperature gradient between the hypolimnion and metalimnion typically resists mixing (Fig. 3.7, 30 May cast), allowing undisturbed accumulation of varve couplets. This interpretation is consistent with varve-like structures at the bottom of the pre-

jökulhlaup Station 4 core (Fig. 3.14a) and cesium-137 dated percussion cores from a similar location (Smith et al., 2004).

When water was overflowing from the ice-dammed lake in mid-July, the deepest parts of the northeast basin were filled with cold, fresh, and turbid water (Figs. 3.7, 3.8). Bottom water was mixed, removing the weak hypolimnion that was present in May (Fig. 3.7). This cold, fresh water could only have been from the overflowing ice-dammed lake, since no major streams besides *'ii'* enter the freshwater basin (Fig. 3.1b). Water in the ice-dammed lake was likely near 0^{o}C, since it is in contact with, and fed almost directly by, the Agassiz Ice Cap, is partially berg and ice-shelf covered, is perennially ice covered, and is about 300 m higher than Lake Tuborg (cf. Maag, 1969; Gilbert, 1971; Blachut and McCann, 1981). Dissolved load and conductivity were also likely low in the ice-dammed lake, since: (1) its largest watersheds are highly glacierized; (2) glacial meltwater reaching the lake is very briefly in contact with the ground, and; (3) it is above marine limit.

Underflows were present in the freshwater basin two weeks before the jökulhlaup. Their formation was facilitated by the removal of the thermocline. The 11 and 24 July casts are inversely thermally and salinity stratified, producing strong density inversions (Figs. 3.7, 3.8) that could only have been compensated for by suspended sediment. This interpretation is supported by highly turbid near bottom water samples from the freshwater basin while the ice-dammed lake was being overtopped.

Pre-jökulhlaup underflow deposition is recorded in the upper part of the freshwater basin surface core (Fig. 3.14a). Fining upward cycles above 80 mm reflect periods of waning sediment transport and deposition, and were possibly deposited diurnally. Inter-cycle coarsening upward reflects an increase in energy with time, as discharge from the overflowing ice-dammed lake likely increased in early to mid July (Fig. 3.5). Amazingly, more sediment was deposited in the deepest part of the freshwater basin in the days to weeks leading up to the jökulhlaup than was deposited in the four preceding years (Fig. 3.14a). Ice rafted debris rainout also occurred (Fig.

3.6a). Importantly, the sill separating the saltwater and freshwater basins confined underflows to the freshwater basin prior to the jökulhlaup (Fig. 3.8, Station 6 cast).

Underflows in the freshwater basin during and after the jökulhlaup may initially have been erosive, and an unknown amount of sediment separates the pre- and post-jökulhlaup cores at Station 4 (Fig. 3.14a, b). Fine-grained lenses at the base of the post-jökulhlaup core are likely rip-up of semi-consolidated sediment, angled laminae may be cross beds, and texture is coarser than pre-jökulhlaup sediment at the same site (Fig. 3.14) pointing towards deposition from bottom currents. Closer to the sill, jökulhlaup-derived erosive underflows exposed dense fine-grained sediments (Fig. 3.15a, Station 5), probably as flow was constricted, channelized, and accelerated near the southwest end of the freshwater basin (Gee et al., 2001).

3.6.3 Processes and deposits in the southwest, saltwater basin

The monimolimnion is warmed by small amounts of solar radiation that reaches the chemocline through the ice cover (Ludlam, 1996; Van Hove et al., 2006). The transmissivity decline at the chemocline (Figs. 3.9, 3.10b, 3.11a) is probably caused by dissolved sulfur associated with a microbial community or an iron-oxide precipitate (Belzile et al., 2001).

Varve formation would be promoted in the meromictic basin by the anoxic monimolimnion and the high N^2 at the pycnocline (Fig. 3.9). However, it is possible that all fine-grained sediment flocculates and is deposited before winter, preventing the regular formation of clay caps (Gilbert, 2000).

During and after the jökulhlaup, cold ice-dammed lake water flowed through the freshwater basin, overtopped the 34 m sill, then flowed along the chemocline and reached the southwest end of the lake (Figs. 3.11b, 3.12a). Flow on boundary layers promotes the development of internal waves that can eventually oversteepen, forming Kelvin-Helmholtz

billows. Billows form when the gradient Richardson number ($R_i=N^2/(du/dz)^2$) is less than 0.25 (*du/dz* is velocity shear; McCool and Parsons, 2004). Billows rapidly collapse due to internal instability, resulting in a thickened boundary layer (Geyer and Smith, 1987). This interpretation is consistent with the post-jökulhlaup chemocline thickening (Fig. 3.12b), and the decrease in conductivity with distance slightly above the chemocline (Fig. 3.13b). Flow at the chemocline would have waned with distance, and distal billows would have had smaller length scales. In the Fraser River Estuary, chemocline thickening has been recorded under similar physical conditions, and Kelvin-Helmholtz billow length scales decreased distally (Geyer and Smith, 1987).

In the meromictic basin, extremely high shear is required for R_i to drop below 0.25 because of the exceptionally high N^2 at the chemocline. This is why the chemocline thickening was subtle (Fig. 3.12b), and monimolimnion cooling and freshening was minimal (Fig. 3.12c, d).

The Lake Tuborg chemocline remains anomalously sharp compared to most other high arctic meromictic lakes (Ludlam, 1996; Van Hove et al., 2006) because flows along the chemocline during jökulhlaups disturb vertical diffusion by molecular diffusion and wind-generated mixing (Toth and Lerman, 1975, Van Hove et al., 2006).

The depth of the Lake Tuborg chemocline is also regionally anomalous, and was thought to be controlled by the ice-contact depth (Ludlam, 1996), but shallow bathymetry at both ends of the lake discounts this possibility (Fig. 3.1c). Rather, chemocline depth is a function of the sill depth, shear, N^2, and turbidity.

Interflows progressed much less far into the meromictic basin than overflows (Fig. 3.11a). Kelvin-Helmholtz billows would have mixed turbid fresh water with salt water, allowing fine grained particles to flocculate and drop from suspension.

Jökulhlaup-derived sedimentary processes near the sill in the meromictic basin are inferred from the Station 7 core (Fig. 3.15b). The bottom slope is relatively steep, and the

chemocline is only 7 m above the lake bottom at this site. Several processes could have deposited the thin, coarse laminae in the core: (1) Downward propagating internal waves could have redistributed sediment. Little energy is required to do this, since the monimolimnion has near zero N^2 (Fig. 3.9; Smyth, personal communication); (2) A slump could have been triggered either by internal waves on the chemocline hitting the sill (Rimoldi et al., 1996), or by freshly deposited sediment oversteepening the sill; (3) Settling-driven convection. Hyperpycnal flows could have been generated as particles accumulated at the chemocline until their concentration exceeded the density of the monimolimnion (Hoyal et al., 1999; Parsons et al., 2001; McCool and Parsons, 2004). It is noted that double-diffusive convection (Parsons et al., 2001) was not possible at the chemocline because the cold stratum was superimposed on the warm monimolimnion: a thermally stable situation at temperatures less than maximum water density; (4) 'River-generated' turbidity currents with interstitial fresh water. When turbidity currents were insufficiently thick to overtop the sill, they would have suddenly been restricted to the freshwater basin, and saltwater basin deposition would have been solely from interflows and overflows (Chikita et al., 1996). This is a plausible explanation for the abrupt decrease in grain size above 30 mm (Fig. 3.15b). However, classic river-generated turbidity currents with interstitial fresh water require extremely high SSC to overcome density deficits created by ambient salt water, and are globally very rare (Gilbert, 2000; Mulder et al., 2003). At Lake Tuborg, turbidity current SSC would have to exceed 20 000 mg/L for SSC to exceed this density deficit (Fig. 3.9). Although the most turbid near bottom water sample in the fresh water basin during the jökulhlaup only contained 1100 mg/L, fluvial SSC in jökulhlaups has exceeded 200 000 mg/L (Mulder et al., 2003).

The process(s) responsible for the laminae in the Station 7 core did not progress into the deep, distal parts of the saltwater basin. Interflows were not spatially extensive in the saltwater basin after the jökulhlaup (Fig. 3.11). The extent of underflows is unknown, but near bottom processes are inferred from surface core 'K' (Fig. 3.16). The coarse, mostly massive, fining

upward cap (Fig. 3.16 '*J03*') was deposited during and after the jökulhlaup, since it is not present in cores F, A, or B. The cap was deposited non-erosively, and underlying sediments were not disturbed (Fig. 3.16). The ~90 m between the chemocline and lake bottom would minimize the potential for erosion by downward propagating internal waves. Slump and hyperpycnal flow progression to the coring site is unlikely because of: (1) the great distances between the coring location, sill, and jökulhlaup inflow, (2) the 1^{o} average bed slope between the sill and saltwater basin, and (3) the high monimolimnion salinity and density.

The nearly massive structure of the 'K' cap points to deposition by sediment rainout from hypopycnal flow. Sediment was likely rapidly deposited at the site from the upper monimolimnion and lower mixolimnion by flocculated sediment that settled faster than rates predicted by Stokes Law.

3.6.4 Supraglacial lake drainings above *'iv'*

Repeated slush flow events are capable of very slightly freshening the monimolimnion during peak glacial melt in early July (Fig. 3.12d; 16 July 2003 cast). However, sediment plumes associated with these events are not as extensive as jökulhlaup-derived plumes (cf. Figs. 3.10, 3.11a). Supraglacially-derived plumes are not capable of producing the distinctly thick, nearly massive deposit in the post-jökulhlaup core at Station 12 (Fig. 3.16 '*J03*'), or of producing the distinct post-jökulhlaup freshening, cooling, and mixing that occurred after the jökulhlaup (Figs. 3.11, 3.12, 3.13).

Supraglacial lakes above *'iv'* are small compared to the ice-dammed lake. The water volume discharged in the entire 45-day 1995 monitoring season (Braun, 2000) was 60 and 105 times less than the two ice-dammed lake estimates of the jökulhlaup volume, but only about 20%

of the 1995 discharge occurred during slush flow events. Q_{max} in 1995 was ~16 m^3/s near '*iv*', compared to 2200-3150 m^3/s from the jökulhlaup.

3.6.5 Previous jökulhlaups

The ice-dammed lake drained in 1993 (R.M. Koerner, personal communication, 1996). Detailed measurements were next made at Lake Tuborg in 1995, when a cold stratum remained in the saltwater basin (Phelps, 1996). Observations in 1995 included kettle holes, a glacier portal near '*ii*', and a raised shoreline on marine mud terraces on the north shore of the freshwater basin (M.J. Retelle, personal communication, 2005). It is likely that the lower fining upward sequence in the stratigraphy (Fig. 3.16 '*PJ*') is the upper part a deposit from the 1993 jökulhlaup.

A jökulhlaup also occurred between 1960 and 1963. Air photos from August 1960 show a full, overflowing ice-dammed lake, and an ice-raft near *'ii'* (Fig. 3.4). Bergs were observed at Lake Tuborg in 1963 (Hattersley-Smith and Serson, 1964). There was no cold stratum in 1963 (Hattersley-Smith and Serson 1964), so the jökulhlaup likely occurred closer to 1960 than 1963.

3.7 Conclusions

A large and rare jökulhlaup drained into Lake Tuborg in July 2003, while a detailed lake process study was being conducted. The jökulhlaup drainage style, and the effects on the limnology and sedimentology of Lake Tuborg have been described.

Before the jökulhlaup, a weak thermally-derived hypolimnion was removed in Lake Tuborg's proximal freshwater basin. This facilitated the formation of hyperpycnal flows. During and after the jökulhlaup, underflows eroded the lake bottom in parts of the freshwater basin,

exposing dense, laminated sediments, and creating an unconformity. However, some areas of the freshwater basin experienced high sedimentation rates, and cross-beds and fine-grained rip-ups were deposited.

Alternatively, in the saltwater basin, underflows were limited to steep and proximal areas close to the sill. More distally, jökulhlaup-derived sedimentary processes were not erosive, and a unique thick, coarse, fining upward facies was deposited, probably because of the low bottom slope and the great depth between the chemocline and lake bottom. Underflow run-out distances were limited by rapid deposition from saltwater flocculation.

The monimolimnion has remained remarkably salty for ca. 3 ka, and through at least three jökulhlaups (1960-1963, 1993, 2003). Mixing of the monimolimnion has been limited by the extremely high N^2 at the chemocline.

Monitoring has also allowed the sedimentary signal and limnologic consequences of jökulhlaups to be disentangled from those of slush flows from supraglacial lakes (Braun et al., 2000). It should therefore be possible to unambiguously identify jökulhlaup deposits in the long core record, and produce a millennial-scale undisturbed reconstruction of jökulhlaup frequency, which would test long-term models of jökulhlaup frequency and magnitude (Clague and Evans, 1994).

3.8 Acknowledgments

National Science Foundation (NSF) grant ATM-9708071, NSF Doctoral Dissertation Research Improvement Award 0221376, Geological Society of America graduate student grants, an Artic Institute of North America grant-in-aid, and the Gloria A. Radke prize from the University of Massachusetts supported this research. The Polar Continental Shelf Project (PSCP) and VECO Polar Resources provided outstanding logistical support. PCSP was especially responsive to rapidly evolving conditions in the field during the jökulhlaup. Lesleigh Anderson, James Bradbury, David Mazzucchi, Joe Rogers, Anders Romundset, and Chloë Stuart provided assistance in the field. Robert Gilbert and Bill Smyth provided valuable advice on mixing processes. Comments by Garry Clarke and an anonymous reviewer are greatly appreciated.

CHAPTER 4

RECENT OCCURRENCE OF LARGE JÖKULHLAUPS AT LAKE TUBORG, ELLESMERE ISLAND, NUNAVUT

4.1 Abstract

The varved sediment record from glacially-fed Lake Tuborg, Ellesmere Island, Nunavut, shows that only three large jökulhlaups have occurred there in the last millennium: 2003, 1993, and 1960. Detailed analyses of sediment microstructure and particle size, combined with *in-situ* hydrometeorological and limnological process studies, allowed jökulhlaup facies identification and discrimination from deposits from other processes. Deposits from large jökulhlaups are anomalously thick, typically lack internal structure, have sharp bases, and fine upwards. The ice-dammed lake above Lake Tuborg (the source of the jökulhlaups) likely changed its drainage style in 1960, from ice-dam overtopping to ice-dam flotation and glacial tunnel enlargement by melt widening, which allowed the lake to drain completely and catastrophically.

Complete drainage of ice-dammed lakes by ice-dam flotation is rare in the region is due to the pervasiveness of cold-based ice. Twentieth century warming is likely responsible for some combination of dam thinning, lake expansion and deepening, and changing the thermal regime at the base of the dam.

Anomalously thick individual varves were periodically deposited beginning in the 19th century, and their thickness increased with time. This likely reflects a combination of increased ice-dam overtopping, subaqueous slope failures, sediment availability and rising air temperature.

The varve record presented here significantly correlates with a previous, shorter record from Lake Tuborg. However, generally weak correlations are found between the new varve time series, regional records of air temperature, and glacial melt from ice cores on the Agassiz Ice Cap.

It is hypothesized that on short timescales, sedimentation at the coring location reflects a complex and varying integration of multiple hydroclimatic, geomorphic and limnologic influences.

4.2 Introduction

Most ice-dammed lakes studied in the Canadian High Arctic drain incompletely by overtopping their ice dams (Maag, 1969). However, in July 2003, a large ice-dammed lake on Ellesmere Island (Fig. 4.1B) drained subglacially by floating its ice dam. An englacial or subglacial conduit system developed, and the ice-dammed lake drained completely (Lewis et al., 2007).

The ice-dammed lake drained into Lake Tuborg (Fig. 4.1), a large lake with trapped sea water in one of its basins, and annual laminae (varves) in portions of its lake bottom (Smith et al., 2004). Monitoring of the 2003 *jökulhlaup* (Icelandic for glacier-burst), and examination of the resulting sedimentary deposits in Lake Tuborg, suggested that a characteristic thick, fining upward jökulhlaup-derived facies was deposited without eroding underlying sediments in a deep site far from the jökulhlaup inflow (Lewis et al., 2007).

Little was known about the frequency, magnitude, and drainage style of similar events in the past. This paper presents an overlapping 515 cm sequence of varved sediment that was obtained from this deep, distal location, providing a unique opportunity to evaluate jökulhlaup activity for the last 1060 years.

Few high-resolution reconstructions of jökulhlaup history have been attempted (Atwater, 1984; Waitt, 1984; Gilbert et al., 1997; Blais-Stevens et al., 2003), probably because of the potential for erosion of underlying sediments by hyperpycnal flows in proximal locations, and the potential for bypassing in distal locations, especially in the marine environment (Maria et al., 2000). At Lake Tuborg, a shallow sill protects distal locations from erosive hyperpycnal flows, as does an extremely dense and deep saltwater layer. The long, straight shape of the lake ensures

that turbid jökulhlaup-generated overflow plumes are distributed through the lake, making sediment bypassing unlikely (Lewis et al., 2007; see Discussion).

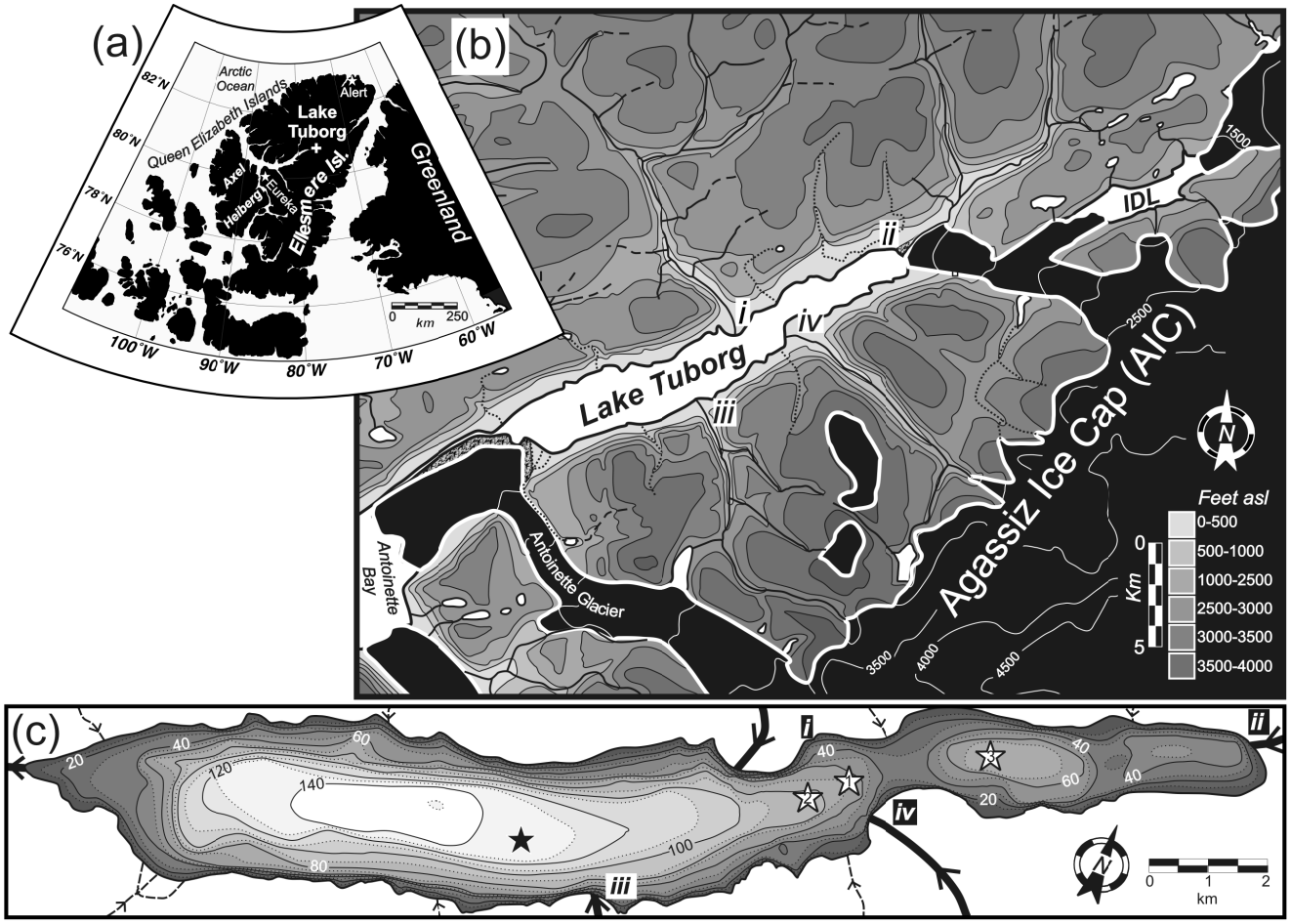

Figure 4.1. (A) Location of Lake Tuborg on Ellesmere Island in the Canadian High Arctic. (B) Physiography and topography near Lake Tuborg and the ice-dammed lake (IDL). Contour interval is 500 feet; shading is feet asl. 'i' through 'iv' mark the mouths of the major rivers that feed Lake Tuborg. (C) Lake Tuborg bathymetry and coring locations. The black star is the location of the core sequence described here, and is at 80.95°N, 75.764°W. The white numbered stars are the locations of cores from Smith et al. (2004). Solid bathymetric contours are every 20 m.

This paper builds upon previous varve studies at Lake Tuborg by using multi-annual lake and hydrometeorologic process studies to pinpoint an ideal coring location, and evaluate potential hydroclimatic forcings for sedimentary structures in the core record. *In-situ* process studies have been particularly informative, since Lake Tuborg has complex bathymetry, chemical and thermal stratification, and multiple sediment inputs. This work also triples the length of a previously published Lake Tuborg varve record (Smith et al., 2004). In addition, only two other glacially fed lakes in the Arctic have had the paleoenvironmental significance of their sediments studied (Lamoureux and Gilbert, 2004; Chutko and Lamoureux, 2008).

4.3 Site description and previous work

Lake Tuborg is located on north-central Ellesmere Island (Fig. 4.1A). Eureka is the closest Meteorological Service of Canada weather station (Fig. 4.1A; 220 km southwest; 10 m above sea level (ASL)), where mean annual air temperature from 1948-2003 was -20 ^{o}C, and the only months with average temperatures above freezing were June (2.3 ^{o}C), July (5.6 ^{o}C), and August (3.1 ^{o}C). On average, 32 mm of precipitation (snow and rain) fell at Eureka from June to August. The largest precipitation event lasted four days in mid-August, 1953, when 50.1 mm fell. On average, the largest June to August precipitation event is 10.8 mm (σ=7.8 mm). Air temperatures at Lake Tuborg and Eureka are very similar, though it is typically, but not always, slightly warmer at Lake Tuborg (Table 4.1). In four summers of monitoring at Lake Tuborg, the lake generally received more precipitation than Eureka (Table 4.1).

Table 4.1 Comparison of air temperature and precipitation at Eureka and Lake Tuborg*

	Temperature (°C)			Precipitation (mm)	
	Eureka	Lake Tuborg	r	Eureka	Lake Tuborg
1995	3.2	4.1	0.94	6.5	10.9
2001	4.2	3.8	0.90	31.2	97.1
2002	3.7	4.1	0.84	91.5	52.3
2003	4.7	5.1	0.92	23.4	27.7

*1995 data (Braun et al. 2000a) are for June only. 2001-2003 data are from May 28 to August 10. All records are from about 10 m ASL.

Lake Tuborg is at 11 m ASL, and is separated from the sea at its outlet by sediments from a grounded arm of the Antoinette Glacier (Fig. 4.1B). Marine isolation occurred at approximately 3000 yr BP, based on ^{14}C measurements from bicarbonate in the trapped saltwater in the southwest basin (Long, 1967). Watersheds surrounding Lake Tuborg are largely unvegetated and unmodified by humans, and are underlain by Lower Silurian to Lower Devonian Danish River Formation calcareous-dolomitic sandstone (Trettin, 1996).

A large watershed feeding Lake Tuborg from the north is unglacierized at present, and sediment and water are transported during a brief period of peak nival melt in mid-to-late June (Fig. 4.1B, location i). After the supply of snow is exhausted in July, nival-fed streams largely dry up. However, two glacially-fed tributaries drain into Lake Tuborg at its south shore (Fig. 4.1B, locations iii and iv), and these are fed by the cold based Agassiz Ice Cap, which parallels the shoreline at 900 m ASL, and has an equilibrium line altitude of about 1260 m ASL (Braun, 1997). Hydrometeorologic monitoring at location iv showed that sediment transport responds in a complex, nonlinear way to weather and climate. As the freezing line moves up the ice cap during mid-to-late July, meltwater is temporarily stored in relatively small ephemeral supraglacial lakes. These lakes periodically drain into Lake Tuborg in discrete slush flow events, and transport large volumes of sediment over a period of days (Braun et al., 2000). Based on aerial photographs and

field observations, this supraglacial meltwater ponding does not seem to occur in the watershed above location iii (Fig. 4.1B).

An extremely large ice-dammed lake exists above the northeast corner of Lake Tuborg (Fig. 4.1B). The surface elevation of the full lake was 342 m ASL in February, 2003 (Zwally et al., 2003, updated 2007), and the lake dimensions are 6 x 1.5 km. The lake captures supraglacial meltwater from the Agassiz Ice Cap, and is normally completely isolated from Lake Tuborg. However, in 2003, the level of the lake rose enough to begin draining by overspilling its ice dam in early to mid July. Overspilling ended abruptly on July 25, when the lake catastrophically and entirely drained into Lake Tuborg. Between 3.2 and 5.5 x 10^8 m^3 of water drained, making the jökulhlaup the largest observed in Canada since 1947. It was triggered by ice-dam flotation, an extremely rare drainage style for Canadian High Arctic ice-dammed lakes. The 2003 event is described in detail in Lewis et al. (2007), and results pertinent to this study are summarized in the Discussion section.

Lake Tuborg has two basins separated by a shallow 34 m sill: a large 145 m deep saltwater basin to the southwest, and a smaller 74 m freshwater basin to the northeast (Fig. 4.1C). The saltwater basin has an extremely sharp and strong chemocline at 56 m depth that separates fresh water from dense underlying saltwater with a salinity of about 25 practical salinity units (PSU).

Lake-level varies by about one meter in typical summers. In 2003, lake-level increased by two meters while the ice-dammed lake was overspilling, and eight meters during the jökulhlaup.

Several factors promote undisturbed deposition of clastic varves in the saltwater basin. The severe climate only allows for river flow and sediment transport during a brief period during summer (Braun et al., 2000), when relatively coarse particles are transported throughout the lake and deposited (Lewis et al., 2007). Over the long winter, clay-sized particles should slowly settle and form a clay cap on the summer deposits (Smith and Ashley, 1985). The great depth of the

basin (145 m) and the nearly perennial lake ice cover prevent wind-generated mixing of lake bottom deposits (Håkanson and Jansson, 1983; Lewis et al., 2007). Physical mixing between the saltwater and freshwater layers is inhibited by the sharp and strong density difference, equivalent to 20,000 mg/L (Lewis et al., 2007). By contrast, hydrologic monitoring of the largest glacially-fed stream showed that hourly fluvial suspended sediment concentration was always less than 5.3 mg/L, even during slush flows (Braun, 1997; Braun et al., 2000). Therefore, hyperpycnal flows should rarely – if ever – plunge below the chemocline and erode underlying sediments. Finally, anoxic conditions inhibit disturbance by bioturbation in the saltwater basin (Lewis et al., 2007).

Previous paleoenvironmental work on Lake Tuborg sediments was based on two percussion cores from the saltwater basin near the sill, and one from the freshwater basin (Fig. 4.1C; Smith et al., 2004). Sediments were interpreted as varves, and the available record was 300 years long. Distinctly thick often sand-rich deposits were interpreted as the result of high-magnitude catastrophic discharge events, and these events increased in frequency from the beginning of the 19th century until 1962. In addition, significant correlations were found between the varve thickness record and the record of melt layers on the Agassiz Ice Cap (Fisher et al., 1995), and 900 mB air temperatures at Eureka (Smith et al., 2004). However, Smith et al. (2004) were unable to discriminate between slush flow deposits, jökulhlaup deposits, and other processes capable of producing thick coarse-grained deposits.

4.4 Methods

Sediment cores were obtained from Lake Tuborg in the central part of the saltwater basin, in 135 m of water (Fig. 4.1C). Three coring techniques were used to ensure continuous and undisturbed recovery of sediment. Two vibracores (475 and 387 cm) were obtained in 2001 using a Rossfelder VT-1 submersible vibracorer. Long cores were obtained with the vibracorer in extremely deep water without disturbing laminae through core barrel friction. An Ekman dredge was also used repeatedly before and after the 2003 jökulhlaup to obtain a continuous 22 cm stratigraphy of short cores (<13 cm each) of highly unconsolidated near-surface sediments (Lewis et al., 2007). Square polycarbonate tubing was used to carefully subsample dredged sediment, and sediment-filled tubes were shipped vertically. Finally, the coring location was revisited in June 2006, when an Aquatic Research percussion corer was used to obtain the uppermost 184 cm of sediment. This was needed because the jökulhlaup-derived deposit had not fully formed when the last Ekman core was obtained, due to a thick jökulhlaup-derived overflow plume over the coring location in August 2003 (Lewis et al., 2007). In addition, the upper 8-22 cm of the vibracores were disturbed during the coring process, and it was unclear whether the Ekman stratigraphy overlapped with the undisturbed section of the vibracores. The 2005 percussion core provided the necessary undisturbed overlap.

Cores were split lengthwise in the lab using a circular saw, Dremel tool, and carbide-tipped tile-scoring knife. Split halves were photographed at the Limnological Research Center LacCore facility at the University of Minnesota-Twin Cities. Digital linescan images were obtained with a Geotek Corescan-V at 20 pixels/mm resolution.

Undisturbed overlapping sediment slabs were removed from split core faces, epoxy impregnated, mounted on 7.6 x 2.5 cm glass slides, and ground to 30 µm thickness (Francus and Asikainen, 2001). Impregnated and polished slabs were prepared from both vibracores, which allowed the identification of small-scale unconformities, and strengthened the varve-based

chronology. An Epson V750-M Pro flatbed scanner was used at 2400 dpi to image polished slabs and thin sections under plain and cross-polarized light using normally-oriented polarizing filters above and below the thin section (Lamoureux and Bollmann, 2004). Discrete sand-rich layers, subannual laminae, and clay layers were counted, and their thicknesses were measured using the Export to Illustrator feature of Photoshop (Francus et al., 2002). Where laminae boundaries remained unclear, a Zeiss EVO scanning electron microscope (SEM) was used in backscattered mode to obtain images of individual silt- and sand-sized particles under high magnification (Francus, 1998).

Two varve counts were performed. The first was completed using only polished slabs; 831 varves were counted to a composite depth of 320 cm. Thin sections and SEM images were used in the second count, in addition to polished slabs; 990 varves were counted to the same depth. A much more accurate count was performed with the additional imagery, so only the second count is presented here.

Dry bulk density was measured every centimeter on Ekman cores and the percussion core, and every five centimeters on the vibracores using a 1 cm^3 constant volume subsampler (Håkanson and Jansson, 1983). Dry bulk density between sampling points was modeled with a series of best-fit equations, and annual mass accumulation rate was calculated as the product of modeled dry bulk density and varve thickness (Schiefer, 2006). Calculation of annual mass accumulation theoretically compensates for changes in dry bulk density near the sediment/water interface, compaction due to core barrel friction, and textural differences. However, changes in dry bulk density were relatively small in relation to changes in varve thickness, and the mass accumulation record is very similar to the unmodified varve record (Fig. 4.2).

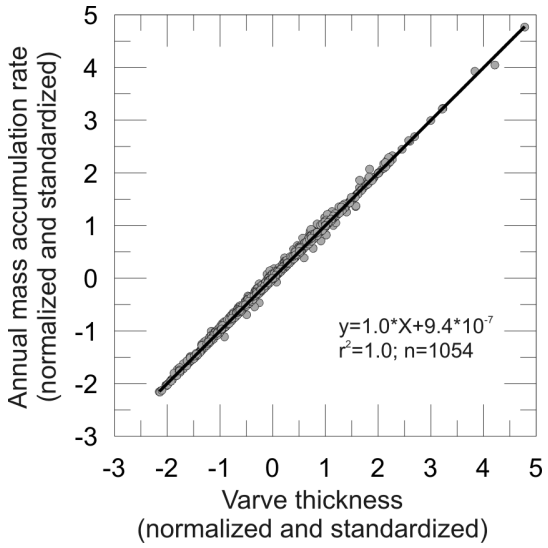

Figure 4.2. Comparison of varve thickness with calculated annual mass accumulation rates. Varve thickness (originally in centimeters) and annual mass accumulation rate (originally in g/cm2/a) time series have been log-normalized and standardized. Black line is the best-fit linear regression.

To permit the use of parametric statistics, the annual mass accumulation time series was log-transformed to normally distribute the dataset, then standardized to a mean of zero and standard deviation of one (Ohlendorf et al., 1997; Rittenour et al., 2000). This process was also applied to the three varve thickness records in the Smith et al. (2004) dataset.

Particle size was measured with a Coulter LS-200 laser diffraction particle size analyzer. Subsamples were obtained every 0.5 cm in the core sequence, and were pretreated with hydrogen peroxide to remove organic particles, and a mixture of sodium hexametaphosphate and sodium carbonate to disperse aggregates (Head, 1992). Slurries were shaken and sonicated before they were analyzed. Statistics were calculated by the moment method.

X-ray fluorescence (XRF) for determination of elemental composition was performed every millimeter on split cores on an ITRAX core scanner at the Institut national de la recherche scientifique. Exposure time was 10 s, voltage was 55 kV, and current was 45 mA.

X-ray diffraction (XRD) was performed for determination of mineralogy on seven samples using a Scintag XDS2000 in the Smith College Geology Department. Powdered samples

were progressively scanned at 45 kV and 40 mA, from 2^{o} to 62^{o}, and the resulting diffraction patterns were compared with reference cards in the software DMSNT v.2.83.

Independent dating of sediment was attempted using ^{137}Cs, ^{210}Pb and ^{14}C. Alpha spectroscopy of ^{210}Pb, and gamma spectroscopy of ^{137}Cs and ^{226}Ra was performed on nine subsamples at the Environmental Radiochemistry Laboratory, University of Manitoba. Woody fragments were exceedingly rare in the highly-clastic, organic-poor sediment; however, one sample from near the base of the varve sequence (Fig. 4.3D) was dated at the National Ocean Sciences Accelerator Mass Spectrometry Laboratory (NOSAMS) in Woods Hole, Massachusetts (NOSAMS accession #OS- 60427).

4.5 Results

4.5.1 Facies Description

Depth in the sediment column is expressed as a composite of an overlapping stratigraphy of the vibracores, percussion core, and Ekman cores. A composite core log is presented in Figure 3A. Sediments are divided into five distinct facies based on grain size and internal structure (Fig. 4.3A; Table 4.2). Particle-size distributions for all facies except #4 have moderate peakedness, and are strongly skewed towards fine particle size. XRD results from each of the facies shows that all sediments are composed of quartz and calcite, with chlorite and muscovite also present; however, the proportions of each vary.

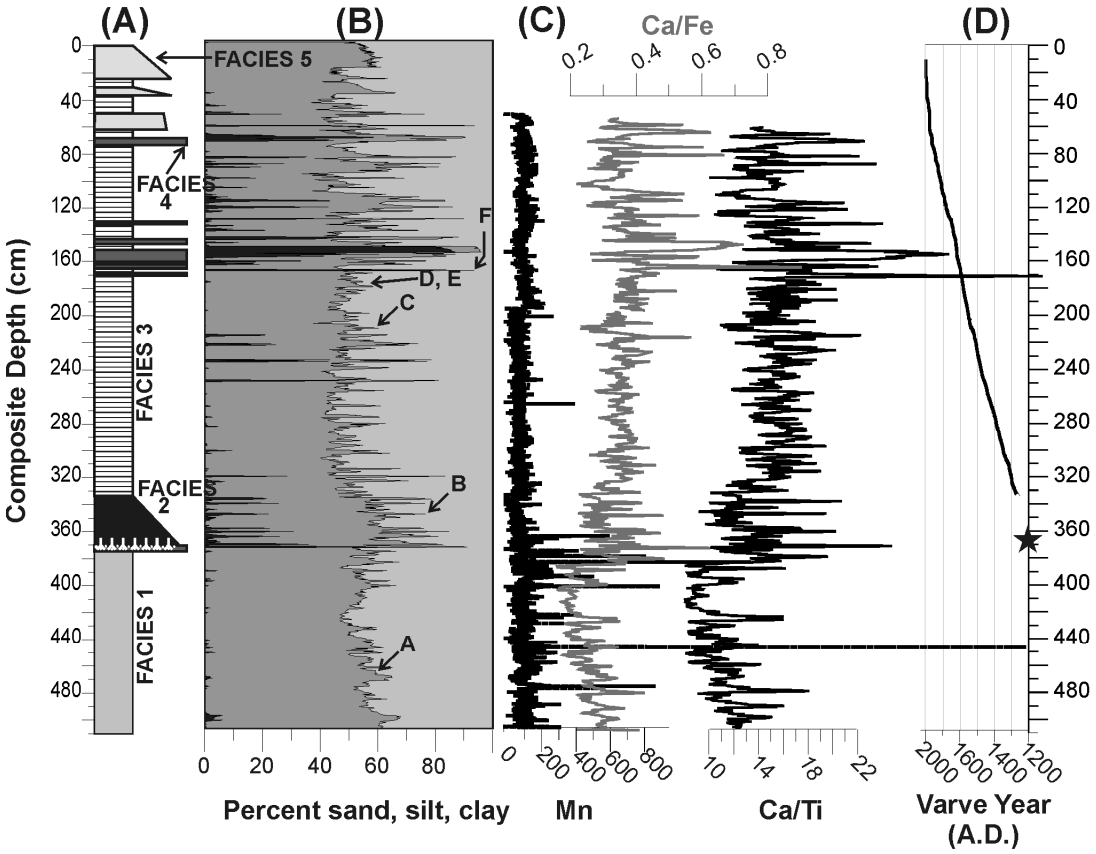

Figure 4.3. (A) Core log, (B) grain size, (C) X-ray fluorescence (XRF) results, and (D) an age/depth plot. Symbols at the base of facies 2 in the core log represent sand, gravel, and woody fragments macrofossils. The grain size plot shows percent sand (black), silt (dark gray), and clay (light gray), and the labels correspond to subpanels in Fig. 4.4. XRF units are peak area element integrals. XRF sample resolution is 1 mm; Mn data are not smoothed, Ca/Fe and Ca/Ti are 9-sample running averages. The star on the age/depth plot shows the location of the 84-389 A.D. 2 σ calibrated radiocarbon date, which was significantly older than predicted by varve counts.

Table 4.2 Mean grain size statistics for facies 1 (largely structureless, basal muds), facies 2 (thick fining-upward microlaminated deposit with iron oxide bands and sands and wood fragments at its base), facies 3 (thin clay-capped laminae that typically fine upward), facies 4 (discrete sand beds), and facies 5 (fine-grained, largely massive deposits).

Facies	n	% of core sequence	Thickness (cm)	Thickness standard deviation	Grain size ($\bar{X}$; µm)	Sorting (σ)	$\sigma/\bar{X}$	Skewness	Kurtosis
1	1	24.5	n/a	n/a	10.2	10.9	1.08	1.74	3.60
2	1	6.5	n/a	n/a	17.4	19.4	1.11	1.54	2.14
3	1058	59.0	0.22	0.22	11.3	13.2	1.16	1.95	4.58
4	6	1.5	1.3	1.6	244.1	210.6	0.86	1.20	2.60
5	3	8.5	13.5	n/a	8.8	9.2	1.04	1.59	2.53

Facies 1, found in the lowermost 140 cm of the core sequence, is relatively structureless and low in sand content (Figs. 4.3A, 4.4A). It is geochemically unique compared to the rest of the cores sequence, as it contains high iron, titanium, and isolated manganese nodules (Fig. 4.3C). Facies 2 directly overlies facies 1, and is a 40 cm thick fining upward sequence with diffuse orange laminae (Figs. 4.3A, 4.4B). Laminae containing matrix-supported gravel, sand, and woody fragments are particularly common near the base of facies 2. Facies 3 is a long sequence of thin laminae with light coloured coarse bases that fine and darken upward to clay caps (Fig. 4.4C). On average, these are classified as fine to medium silt. Facies 4 are sand beds, and are defined as samples with more than half their particle size exceeding 62.5 µm (Fig. 4.4F). The sand beds interrupt facies 3, and consist of very coarse grained sandy deposits with sharp bases and tops, and very low coefficients of variance (standard deviation, σ, divided by the mean, $\bar{X}$; Table 4.2). Facies 4 particle size distributions are the least finely skewed, and are strongly peaked. Facies 5 also interrupts facies 3, but only three examples of these deposits were found, all within the upper 63 cm of the core sequence (Fig. 4.5). Two of these three deposits have sharp bases that fine upward (Fig. 4.5). Facies 5 is typically fine grained, although discrete, thin, coarse-grained beds are sometimes found within otherwise structureless sediment.

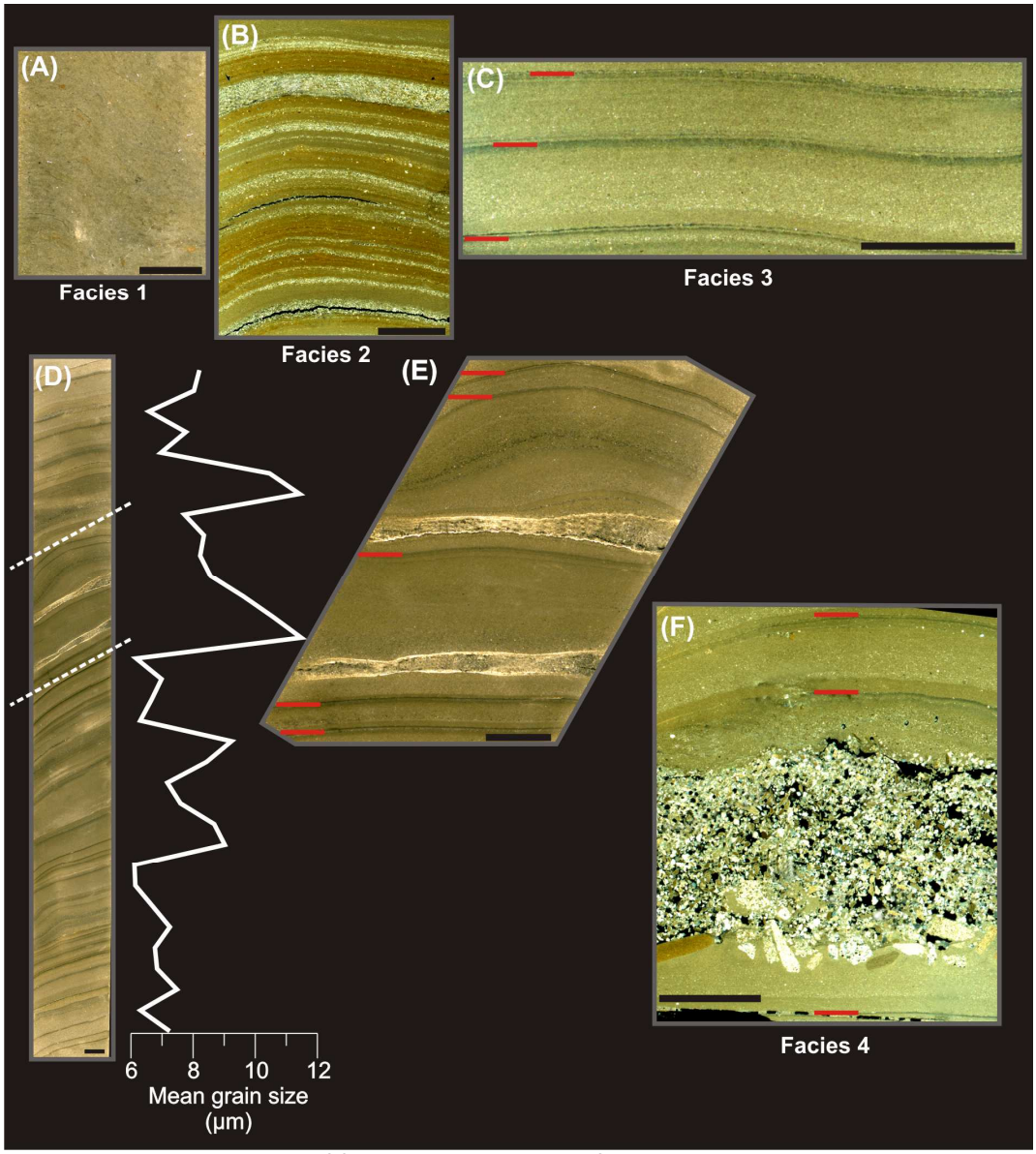

Figure 4.4. Typical examples of facies 1-4. The location of each panel within the core sequence is shown on Fig. 3B. The black bar near the bottom of each image represents 0.5 cm. (A) Facies 1: massive sediments, (B) facies 2: a turbidite with iron oxide staining and microlaminated sands alternating with silty/sand layers, (C) facies 3; varves with dark clay caps (marked with red hashes), (D) A varve sequence with mean grain size, showing a fining upward unit between the white dotted lines. (E) A close up of the area between the white dotted lines in 'D', showing that two thin sand beds at the base of two varves were responsible for the fining upward sequence. (F) facies 4: a sand-rich, grain supported layer in the middle of a varve (clay caps are marked with red hashes). 'A', 'D', and 'E' are flatbed scans of polished, epoxy impregnated slabs of sediment. 'B', 'C', and 'F' are flatbed scans of thin sections under cross-polarized light.

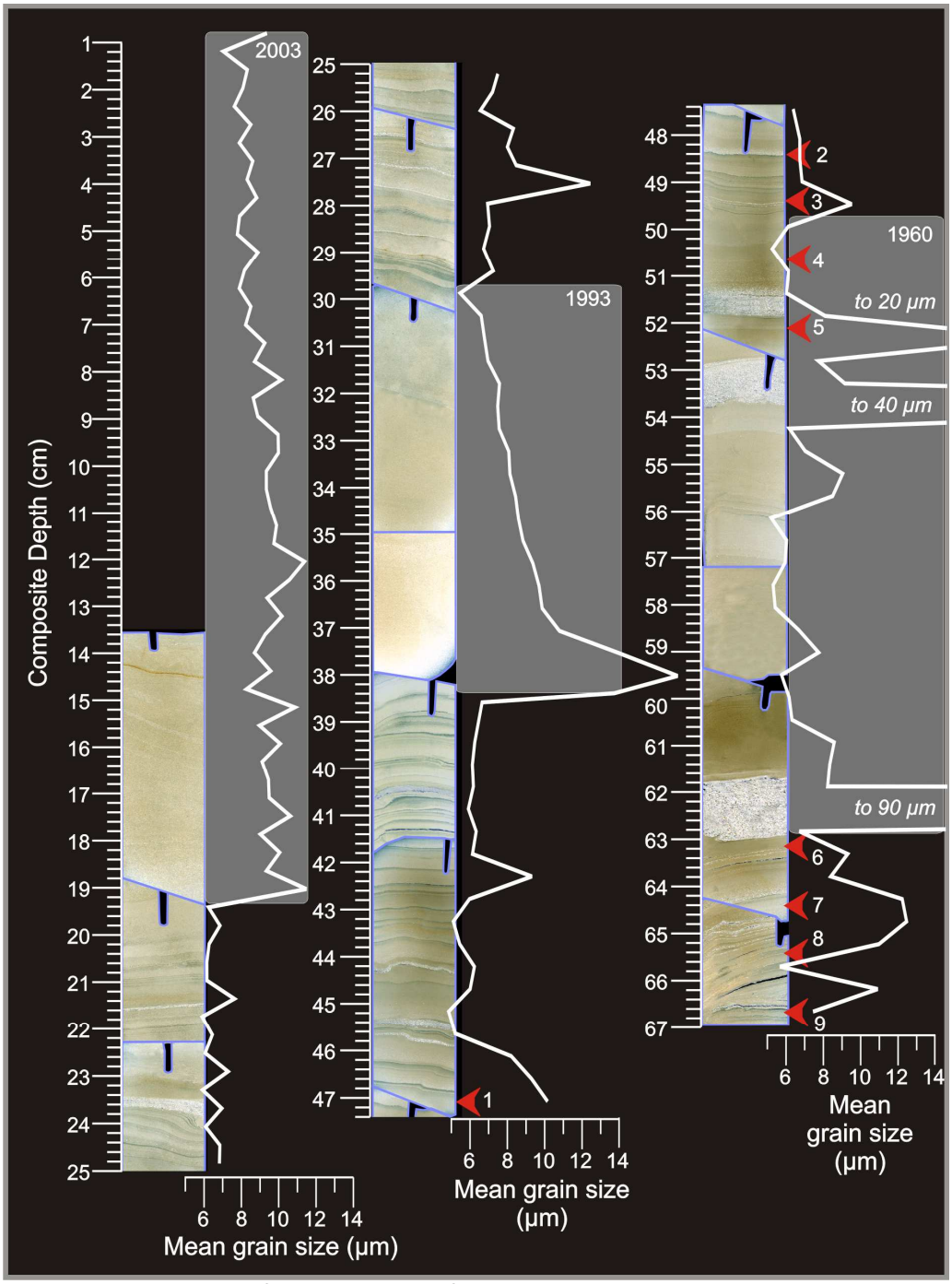

Figure 4.5. Photomosaic of the upper 67 cm of the core sequence. Graphs show mean grain size. The 2003, 1993, and 1960 jökulhlaup deposits are highlighted in gray. The locations of ^{137}Cs and ^{210}Pb subsamples are the numbered red arrows, with the 1963 ^{137}Cs activity peak found at sample 3 (see Fig. **4.**6). Images are flatbed scans of thin sections under cross-polarized light. Individual thin sections are outlined in blue, and notches at the top of sections are orientation marks. Cuts were made at an angle so the saw blade did not completely destroy any laminae. No thin sections are shown from the upper 13.5 cm of the sediment sequence because epoxy did not cure in clay-rich sediment that was saturated with saline water.

4.5.2 Dating

Peak ^{137}Cs activity occurs at 49.5 cm composite depth within facies 3 sediments (Figs. 4.5, 4.6, sample 3). Clay layers were counted and measured, and compared with the depth of the ^{137}Cs maximum. If the clay layers represent winter deposition, the 1963 layer should correspond to the peak of atmospheric nuclear bomb testing in that year. The correspondence is well within the margin of error from the thickness of the sediment slice (Fig. 4.6). In addition, the magnitude of the peak is consistent with peak ^{137}Cs activity previously measured in sediment from the saltwater basin of Lake Tuborg (Smith et al., 2004). Above the ^{137}Cs peak, activity is less than 2 Bq/g x 10^{-3} (Fig. 4.6, samples 1 and 2), which is consistent with the sharp decrease in atmospheric ^{137}Cs input after the Partial Test Ban Treaty was enacted (Wolfe et al., 2004). Directly below the ^{137}Cs activity peak is a 12.5 cm thick facies 5 deposit (Figs. 4.5, 4.6; see Discussion). Its position relative to the ^{137}Cs peak and its lack of internal structure (except occasional sand beds) implies that it was deposited rapidly, and lamination counting suggests that this occurred around 1960. ^{137}Cs activity within this deposit is relatively high (Fig. 4.6, samples 4, 5), which is consistent with deposition after bomb testing began, but before it was banned. ^{137}Cs activity was also measured in four samples below the thick massive deposit (between 63-67 composite depth; Fig. 4.5), and these had zero activity. This is consistent with sediment deposited before the late 1950's, which is supported by laminae counting, and the timing of the first appearance of ^{137}Cs in other arctic lakes (ex. Stewart et al., 2007). Based on these results, and the classic varve-like structure of the sediments described here (Fig. 4.4C), we conclude that facies 3 are varves.

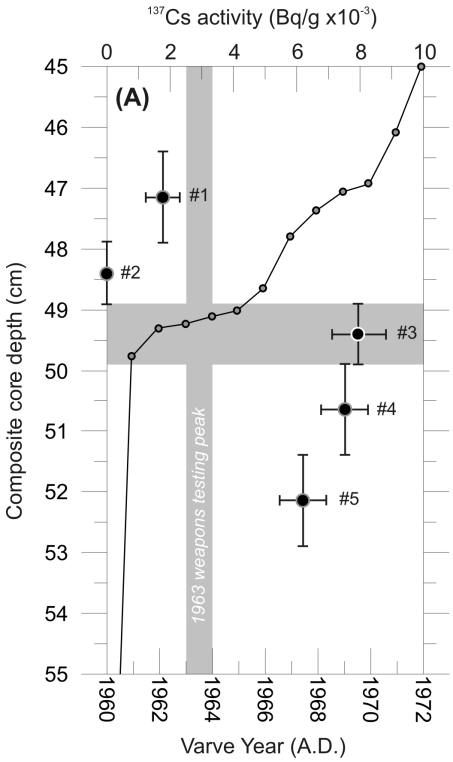

Figure 4.6. Cesium-137 activity (symbols with error bars) and an age/depth plot (line) based on laminae counting. Below sample 3 is a 12.5 cm thick facies 5 deposit (Fig. 4.5). Horizontal error bars are 2 σ, vertical bars represent the thickness of the subsampled slice. Four additional samples below sample 5 have zero activity between 63 and 67 cm composite depth (Fig. 4.5).

Results from analyses of ^{210}Pb and ^{226}Ra show that ^{210}Pb cannot be used as a dating tool, both for the sediment sequence discussed here, and for previously studied sediments from the saltwater basin of Lake Tuborg (Appendix A; Smith et al., 2004). There is no consistent downcore trend in ^{210}Pb activity both with respect to depth and age. Furthermore, ^{226}Ra activity frequently exceeds ^{210}Pb activity, making it impossible to separate ^{210}Pb produced *in-situ* from atmospherically derived ^{210}Pb. However, excess ^{210}Pb was found at 65.5 cm composite depth, which implies that sediments at this depth are younger than 150 years old (Appendix A; Wolfe et al., 2004). Lamina counting suggests that sediment at this depth was deposited around the mid 20th century.

A woody fragment from 365 cm depth (Fig. 4.3D) yielded a ^{14}C age of 1790 BP ± 65 (2 σ calibrated age = 84-389 cal AD; Stuiver and Reimer, 2005). The woody fragment was found in

facies 2 sediment, but if the mean annual sedimentation rate was the same as for facies 3, the woody fragment is 360 years older than expected (Fig. 4.3D).

4.5.3 Identification and occurrence of facies 5 deposits

Deposition at the coring location during the 2003 jökulhlaup was described in Lewis et al. (2007) as a 6 cm nearly massive deposit with a sharp, relatively coarse grained base that fined upward. However, a thick overflow plume was present at the time of coring in August, 2003 so the deposit had not yet fully formed. The percussion core subsequently obtained in 2006 also clearly shows the fining upward sequence, but the jökulhlaup deposit had thickened to 19.5 cm (Fig. 4.5). Unfortunately, epoxy impregnation of the saltwater-saturated, very fine-grained, near-surface sediments in the percussion core was not successful, and thin sections from this zone could not be made. Nevertheless, incompletely cured slabs and core photographs revealed no laminations.

Facies 5 sediments are identified based on their nearly massive texture and anomalous thickness. Only three similar instances are found in the entire 1060 year core record: in 2003, 1993, and 1960. The 2003 and 1993 deposits also have sharp bases that fine upward. The 1960 deposit contains three discrete centimeter-scale sand-rich beds, which fine and thin upward (Fig. 4.5; see Discussion).

The 2003 jökulhlaup deposit is extremely thick compared to all other laminae in the 1060 year record, and compared to the other two facies 5 deposits. It is 4.8 standard deviations greater than the mass accumulation time series mean (Fig. 4.7A, C). The three facies 5 deposits are a major source of the pronounced rise in interannual variance in the late 20th century, which has been more subtly increasing since about 1700 (Fig. 4.7E, F).

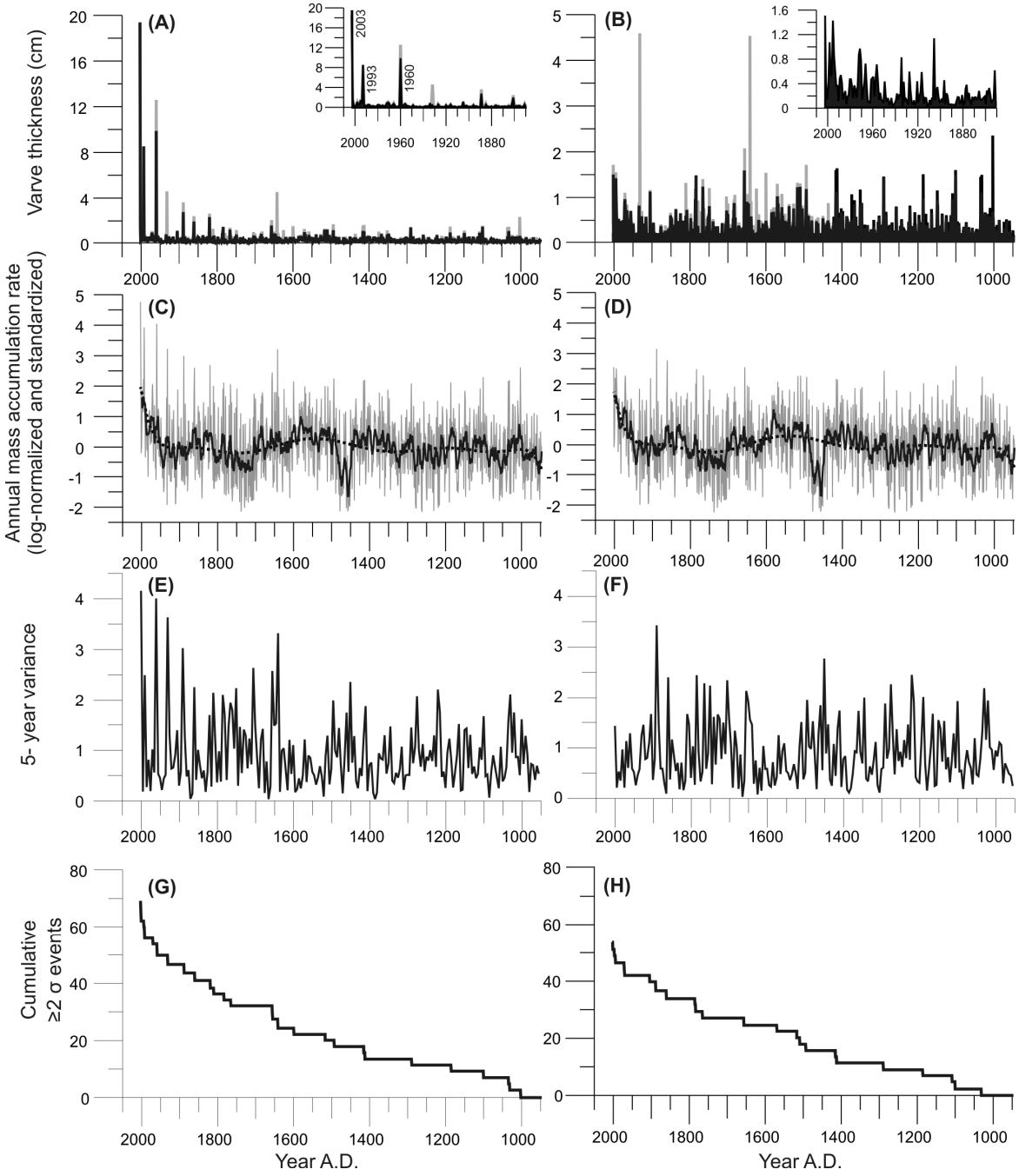

Figure 4.7. Lake Tuborg varve thickness and annual mass accumulation rate. Panels on the left are time series that include jökulhlaup deposits, and panels on the right are with jökulhlaup deposits removed. Inset graphs on the topmost series show varve thicknesses since 1850. Gray plots in 'A' and 'B' represent the contribution from sand layers within each varve. Panels 'C' and 'D' show mass accumulation rate; the gray line is a plot with annual resolution, the black line is a 9-year running average, and the dashed line is a polynomial best-fit curve. Panels 'E' and 'F' show interannual variance with a five year window. Panels 'G' and 'H' are the cumulative sums of annual accumulation rates ≥2 σ above the mean.

4.5.4 Comparisons with the Smith et al. (2004) time series and the Eureka climate record

The new Lake Tuborg varve records significantly correlate with the 300-year Smith et al. (2004) time series. The highest correlations generally occur with 9-year averages that are not adjusted by removing coarse grained deposits and jökulhlaup deposits (Table 4.3).

Table 4.3 Correlation coefficients (r) comparing the Lewis et al. (this manuscript) time series with the Smith et al. (2004) record.

			Smith et al. (2004)			
			All Cores		Saltwater basin cores only	
			5-year	9-year	5-year	9-year
Lewis et al.	Unadjusted	5-year	0.21		0.3	
		9-year		0.47		0.44
	No jökulhlaups	5-year	0.18		0.25	
		9-year		0.42		0.39
	No jökulhlaups, no coarse deposits	5-year	0.22		0.26	
		9-year		0.42		0.39

Notes: The Lewis et al. (this manuscript) time series is presented in an unmodified form, with jökulhlaup deposits removed, and with coarse grained deposits removed. The Smith et al. (2004) time series is presented using all three of their cores, and only the two that were obtained in the saltwater basin. Annual data were smoothed using five- and nine-year running averages. All correlation coefficients are significant at $p<0.05$.

Smith et al. (2004) noted significant correlations between their varve series and the melt record on the Agassiz Ice Cap (r=0.58, $p<0.01$). The new varve series is poorly correlated with the Agassiz melt record (r=0.19, $p=0.308$ for the last 300 years, and r=0.03, $p=0.661$ for the entire record). It is also poorly correlated with air temperature records from Eureka, both at the surface and aloft. For example, 1260 m is roughly the equilibrium line altitude of the Agassiz Ice Cap near Lake Tuborg, and interpolated temperatures at this elevation are poorly correlated to the new varve record (r=0.08, $p=0.308$; See *Discussion*).

4.6 Discussion

We hypothesize that large catastrophic jökulhlaups triggered by ice-dam flotation drained via subglacial and englacial conduits, that they produced facies 5 sediments, and that they began only in 1960. To support this argument, we will review the monitoring of the processes and deposits of the 2003 jökulhlaup (Lewis et al., 2007). Next, we will demonstrate that large jökulhlaup deposits (facies 5) are unique compared with all other sediments. The likelihood of either not recognizing a jökulhlaup deposit, or of incorrectly attributing a facies 5 deposit to another process will be assessed. We will compare the varve record to records of glacial activity in the region and the results from Smith et al. (2004). Lastly, we will argue that the chronology presented here is sufficiently robust to support our conclusions.

4.6.1 The 2003 jökulhlaup

Discharge from the jökulhlaup entered the freshwater basin at its northeast end via a subglacial portal ('A'; letters are labeled on Fig. 4.8). This basin completely filled with extremely turbid, cold, low-conductivity water derived from the ice-dammed lake. Evidence of lake-bottom erosion and hyperpycnal flows was found here ('B'). Hyperpycnal flows in the saltwater basin were limited to areas close to the sill ('C') for several reasons. First, the sill effectively blocked the strongest and most erosive bottom flows. Also, in the saltwater basin, the abrupt and strong density difference between the underlying saltwater layer and the overlying freshwater ensured that the two water bodies remained largely isolated. Small Kelvin-Helmholtz billows formed as extremely cold, sediment-laden water from the ice-dammed lake flowed just above the chemocline ('D'). This allowed sediment laden interflows to mix with saltwater, flocculate, and quickly deposit their sediment close to the sill ('E'). Finally, the long distance (15 km) between jökulhlaup inflow and the saltwater basin coring location ('F'), and the shallow slope between the

sill and coring location (1^{o} average) also ensured that gravity-driven currents did not reach the coring site. Sediments at the coring site were largely delivered by a thick and extensive overflow plume ('G'). This produced a thick, largely massive deposit with a sharp base that fined upward, which was distinct from the laminated sediments underlying the jökulhlaup deposit ('F'; Lewis et al., 2007).

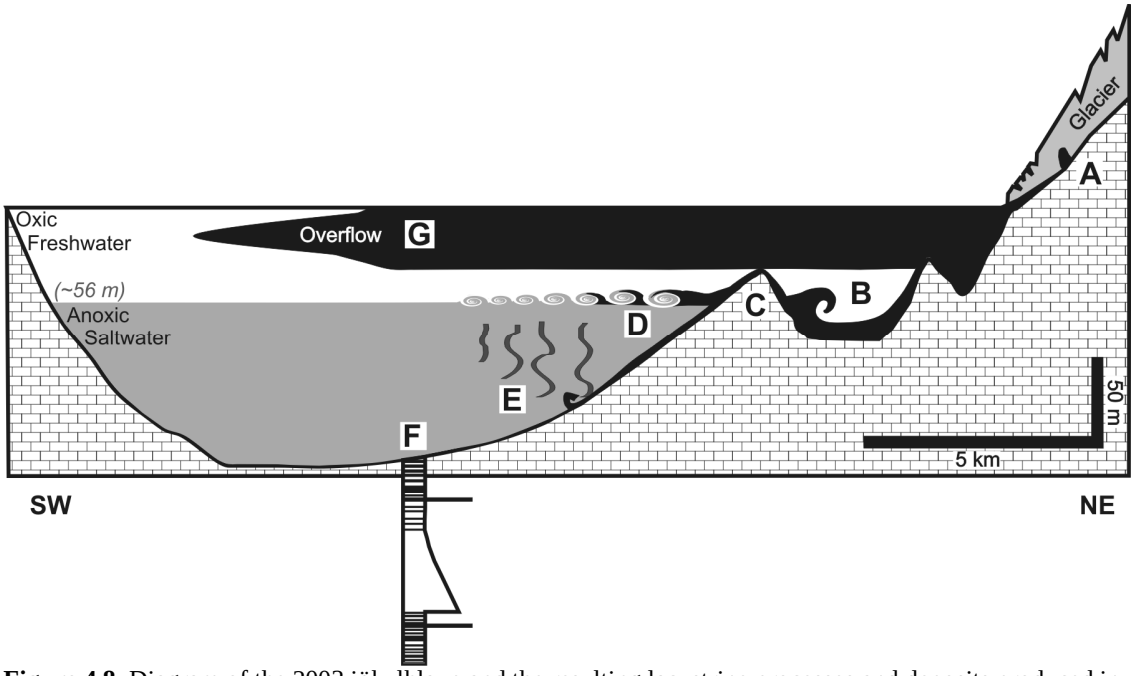

Figure 4.8. Diagram of the 2003 jökulhlaup and the resulting lacustrine processes and deposits produced in Lake Tuborg (summarized from Lewis et al., 2007). Jökulhlaup inflow arrived from a portal at the northeast end of the northeast basin. The large saltwater basin is to the left of the figure, and the saltwater layer is shaded. The log is a representation of the 2003 jökulhlaup deposit overlain and underlain by thin varves and sandy layers. Labels A-G are explained in the Discussion section. Drawn to scale with a 100x vertical exaggeration.

4.6.2 The unique character of large jökulhlaup deposits

Facies 1 is largely structureless (Fig. 4.4A), and could be described as fining upward, and in this sense facies 1 is similar to large jökulhlaup deposits (facies 5; Fig. 4.3B). However, facies 1 is geochemically unique from all overlying sediments, as shown by the XRF data in Fig. 4.3C. While we remain unsure of the process that deposited facies 1, these sediments clearly have different provenance than overlying sediments, and were likely deposited under oxic conditions.

Facies 2 is thick and fines upward (Fig. 4.3 A, B). However, unlike facies 5, terrestrial macrofossils, sand, and gravel are found at its base, and iron-stained silt and clay layers alternate with sandy laminae. This strongly suggests that the source of this deposit is the rivers or slopes surrounding the saltwater basin. It is unlikely that sand, gravel, and woody fragments were transported from the northeast basin. The fining upward character, orange staining, and coarse laminae suggest deposition from a pulsating underflow that delivered oxidized water to the lake bottom (Weirich, 1986; Scranton et al., 2001; Best et al., 2005).

Sands might be transported into the saltwater basin during jökulhlaups either directly in strong hyperpycnal flows that manage to overtop the sill, or indirectly from subaqueous slope failures triggered by rapidly rising and falling lake-levels or oversteepening of the sill. These are likely sources of the three relatively thin sand beds in the 1960 facies 5 deposit (Fig. 4.5). By contrast, the sand-rich facies 4 sediments are much coarser grained, and the tops and bottoms of these deposits are sharp; resumption of varve-like rhythmic laminations is immediate (Fig. 4.4F). It is therefore unlikely that facies 4 sediments were deposited by large jökulhlaups, since a strong overflow would be produced, and a thick fining upward sequence would be deposited on top of the sand beds (Fig. 4.8). Rather, facies 4 sand beds could have been deposited by subaqueous slope failures and melt-out of niveo-aeolian material deposited on the lake ice (Lewis et al., 2002). Hyperpycnal flows are less likely given the chemical stratification of the saltwater basin, but could potentially be generated by extremely turbid runoff associated with rare but intense precipitation events (Gilbert et al., 2006), slush flows (Braun et al., 2000), exceptional glacial melt, and peak nival melt. All of these processes would necessarily have their sources in the saltwater basin and the tributaries and watersheds that drain into it.

Finally, it is unlikely that an overflow plume derived from a large jökulhlaup could bypass the coring location, given the long, straight shape of Lake Tuborg, and the extensiveness of the 2003 plume.

4.6.3 Other potential origins for facies 5 deposits

If a process other than a jökulhlaup could deposit units with all the characteristics of facies 5, then it has not happened more than twice (1993 and 1960). Slush flows (Braun et al., 2000) are an unlikely source of the deposits, based on results from monitoring and core lamination thicknesses. The 1995 varve, which was presumably influenced by the 1995 slush flow events (Braun et al., 2000), has the 14th highest annual mass accumulation of the 1060 year time series (it is 1.5 cm thick, and is 2.4 σ above the time series mean). However, it is 80% thinner (7 cm thinner or 11 g/cm^2 less mass accumulation) than the thinnest facies 5 deposit. It is therefore clearly distinguishable from the deposits identified as large jökulhlaups. Maximum discharge and volume of the 1995 slush flow events was several orders of magnitude less than the 2003 jökulhlaup. Slush flows also occurred in 2003 prior to the jökulhlaup that year. CTD casts showed that lacustrine sediment plumes from these events were strongly attenuated with distance. As a consequence, the 2003 slush flow deposit at the coring location was less than 1.5 cm thick (Lewis et al., 2007).

Another process capable of producing anomalously thick deposits is intense rainfall (Lamoureux et al., 2001; Gilbert et al., 2006). In 2001, June to August rainfall at Lake Tuborg was extremely high, both compared to previous seasons of *in-situ* monitoring, and compared to the long-term precipitation record from Eureka (Table 4.1). From early June until August 10, 97 mm of rain fell at Lake Tuborg, which slightly exceeds the wettest summer in the 56 year Eureka precipitation record (2002; Table 4.1). Interestingly, only 50 mm of precipitation fell over the same period at Eureka in 2001. One eight day period of continuous rainfall at Lake Tuborg produced 47 mm of precipitation in late July 2001; rainfall on two of these days was quite intense, totaling 18 and 15 mm. Discharge and sediment flux at the major deltas increased greatly. However, the coring location was not sensitive to this extreme precipitation; the 2001 varve is in the 43rd percentile for mass accumulation.

Finally, the massive structure of facies 5 sediments are unlikely to have been caused by bioturbation given that the saltwater layer is anoxic. Dissolved oxygen below the 56 m chemocline was <1 mg/L in 2003 (Lewis et al., 2007).

4.6.4 Ice-dammed lake drainage style, volume, and jökulhlaup magnitude

The 1960 deposit is anomalously thick compared to any annual layer before it. Its abrupt occurrence strongly suggests that the ice-dammed lake began draining completely by ice-dam flotation and tunnel development at this point. Prior to 1960, the ice-dammed lake likely drained incompletely by overtopping its dam. The ice-dammed lake drained this way for several weeks in July 2003, before a glacial conduit system developed, allowing catastrophic and complete drainage. The most common style of drainage in the region is ice-dam overtopping, at least prior to 1963 (Maag, 1969).

An abrupt change in drainage style and/or jökulhlaup volume is also consistent with the anomalous microstructure of the 1960 deposit compared to the facies 5 deposits from 1993 and 2003. The 1960 deposit contains three centimeter-scale well sorted sand beds with discrete tops and bottoms, and the thickness and grain size of these beds decreases upwards (Fig. 4.5). Observations made during the 2003 jökulhlaup help explain these discrete sand beds. The ice-dammed lake drained extremely quickly, raising and lowering the level of Lake Tuborg by eight meters in eight days (Lewis et al., 2007). Such rapid changes in lake-level might cause extensive subaqueous slope failures. During the first large jökulhlaup in the history of the lake, nearshore sediments would be particularly prone to mobilization, since they would have been accumulating on the nearshore subaqueous and subareal slopes for at least a millennium under presumably much more stable lake-level conditions.

The thickness (and mass accumulation) of a jökulhlaup deposit is likely related in a complex way to the volume of water drained, hydrograph shape (Rushmer et al., 2002; Old et al.,

2005), sediment availability, and the proportion of sediments transported by hyperpycnal vs. hypopycnal flows. This, and the small number of deposits, makes it very difficult to attribute causes for the observed differences in facies 5 thickness.

4.6.5 The varve record and local and regional records of glacier activity and climate

It is hypothesized that warm air temperatures in the 20th century caused the depth of the ice-dammed lake to increase, or its dam to thin, which allowed the lake to drain by ice-dam flotation beginning in 1960. This is consistent with the progressive but episodic increase in varve thickness (and annual mass accumulation) after 1900 A.D. (Fig. 4.7D). It is also consistent with records of glacier activity in the region that show widespread recent negative mass balance, glacier retreat, and calving. Ice cores from the Agassiz Ice Cap, taken 55 km southeast of Lake Tuborg, show that twentieth century melt is unprecedented in the last 3000 years (Fisher et al., 1995). This record does not continue after 1960; however, the Drambuie Glacier, an outlet glacier on the northeast side of the Agassiz Ice Cap, 110 km southeast of Lake Tuborg, has experienced almost wholly negative melt-driven mass balance since 1977, and the rate of loss is increasing (Koerner, 2005). Shorter term, but more widespread, laser altimetry measurements on Ellesmere Island show extensive and rapid ice-cap thinning, mostly at lower elevations near their margins, below 1600 m ASL. For example, between 1995 and 2000, ice elevations were reduced by >40 mm/yr at the head of Otto fiord, 140 km west-northwest of Lake Tuborg. The thinning occurred when air temperatures at Eureka were 0.7 ^{o}C warmer than the record as a whole, and occurred despite an increase in accumulation (Abdalati et al., 2004).

While there is general agreement between our varve record and regional glacier activity on decadal to centennial scales, weak correlations are found on shorter intervals (ex. using 5 and 9 year running averages). Although the varve thickness and accumulation rate time series likely contain additional paleoenvironmental information, previous studies from proglacial lakes show

that varve thickness is often related in a very complex way to climatic variables (Lamoureux and Gilbert, 2004; Tomkins and Lamoureux, 2005; Menounos, 2006; Hodder et al., 2007; Chutko and Lamoureux, 2008). At the Lake Tuborg coring location, sedimentation is likely an integration of multiple interacting processes, including sediment flux from snowmelt, glacial melt, precipitation, and episodic slush flows; disentangling these influences on the varve record is beyond the scope of this paper. The coring location was chosen to minimize the potential for unconformities and maximize the potential for recording and preserving jökulhlaup-derived sedimentation. By contrast, the cores analyzed by Smith et al. (2004) are much closer to the largest glacially-fed stream that enters Lake Tuborg (Fig. 4.1C; location iv), which likely explains why they found stronger links between varve thickness, Agassiz Ice Cap melt, and air temperature.

The highest correlation coefficients between the varve record presented here and previous records from the lake (Smith et al., 2004) generally occur for accumulation rate time series that have not been adjusted by removing coarse beds and jökulhlaup deposits (Table 4.3). This is reasonable since these deposits were not removed from the Smith et al. (2004) time series. Correlation coefficients are surprisingly high given the likelihood of localized sedimentation controlled by multiple hydroclimatic, geomorphic and lacustrine processes (Hodder et al., 2007).

4.6.6 Chronology

The chronology from 2003 to 1963 is robust considering the correspondence between peak ^{137}Cs activity and laminae counting (Fig. 4.6). Field observations and remote sensing imagery also show that the latest part of the chronology is accurate. The 1993 jökulhlaup was inferred from CTD casts in the lake and observation of kettle holes, raised shorelines, and a portal in 1995 (Phelps, 1996; Lewis et al., 2007). Also, aerial photographs and field observations suggest a jökulhlaup occurred sometime between 1960 and 1963 (Hattersley-Smith and Serson, 1964; Lewis et al., 2007). The chronology beyond 1960 is only based on varve counting. While

the varve counting technique employed here minimizes the effects of localized and coring induced unconformities, it is possible that chronological errors are a source of residuals in correlations to local and regional climate and proxy records. If the ^{14}C date is accurate, then the record is much longer than suggested from varve counts, and recent jökulhlaup deposits are even more anomalous. However, we consider this unlikely. In arctic watersheds, terrestrial organic material, particularly wood, frequently resides on land for long periods of time before being transported to lakes, and ^{14}C dates from lake sediments are very often hundreds of years too old (Abbott and Stafford, 1996; Child and Werner, 1999; Zolitschka, 1996; Wolfe et al., 2004; Oswald et al., 2005; Besonen et al., 2008).

4.7 Conclusions

A threshold was passed in 1960, when the ice-dammed lake above Lake Tuborg suddenly changed its drainage style from ice-dam overspilling to complete drainage by ice-dam flotation and tunnel development. Only three large jökulhlaups have occurred: 1960, 1993, and 2003. The change in drainage style was likely caused by thinning of the ice-dam or deepening of the ice-dammed lake, which is consistent with long term and recent records of glacier ice cap thinning and retreat in the region. Continued warming will likely increase expansion of the ice-dammed lake and its filling rate, and thin its dam, leading to increased jökulhlaup frequency and decreased magnitude. Another threshold may be reached when meltwater can no longer be stored in the ice-dammed lake, either because of retreat of the glacier dam, or thinning of the dam prevents resealing of the tunnel system (Clague and Evans, 1994; Tweed and Russell, 1999; Marren, 2005). This threshold has not yet been reached, since the conduit system closed after the 2003 event, and the lake is currently refilling.

4.8 Acknowledgments

This research was supported by National Science Foundation (NSF) grant ATM-9708071, ATM-0402421, ARC-0454959, NSF Doctoral Dissertation Research Improvement Award 0221376, Geological Society of America graduate student grants, an Arctic Institute of North America grant-in-aid, and the Gloria A. Radke prize from the University of Massachusetts. The Polar Continental Shelf Project (PCSP) and VECO Polar Resources provided outstanding logistical support. Mark Abbott, Whit Patridge, and Joe Stoner expertly retrieved the vibracores. Lesleigh Anderson, James Bradbury, David Mazzucchi, Joe Rogers, Anders Romundset, and Chloë Stuart also provided field assistance. Cores were photographed at the Limnological Research Center, Department of Geology and Geophysics, University of Minnesota-Twin Cities. John Brady kindly provided instruction and time on the Smith College Geology Department XRD. This is PCSP contribution number 03708.

CHAPTER 5

AN AUTOMATED SYSTEM FOR THE STATISTICAL ANALYSIS OF SEDIMENT TEXTURE AND STRUCTURE AT THE MICRO SCALE

5.1 Abstract

A macro has been developed that allows for automated statistical analyses of particles in backscattered electron images (BSEI). The macro code is freely available, and runs on open-source software. It has been specially designed to accommodate very small regions of interest relative to particle size, and to produce continuous downcore stratigraphies. The macro runs quickly and requires no user-intervention, allowing rapid analyses of relatively long sedimentary sequences. Examples of output from three sites are shown. A website has been created that contains the macro code, instructions, and examples of input and output (http://www.geo.umass.edu/climate/lewis/analysis/).

5.2 Introduction

High-resolution records of particle texture and structure are useful for interpreting sub-annual paleoenvironmental data, and for deciphering short-term sedimentary processes from cores and sediment traps. Properly processed backscattered electron images (BSEI) from scanning electron microscopes (SEM) can be used to obtain these records. Image analysis of BSEI is also useful since it is non-destructive (beyond acquiring the thin-section), repeatable, and can be used to find trends in sediment that appear massive to the naked eye (Naruse and Masuda, 2006). Techniques have been developed to obtain undisturbed thin sections from core faces (Francus and Asikainen, 2001), and acquire and process BSEI (Lamoureux and Bollmmann,

2004; Nederbragt et al., 2004). BSEI only image the surface of a thin section, which eliminates 'cutting and hiding' problems inherent in analysis of transmitted microscope images (Seelos and Sirocko, 2005). Also, very small particles, as low as 2 µm, can be counted and measured using BSEI (Soreghan and Francus, 2004).

In the past, researchers have typically focused on image analyses of core subsections (Francus, 1998; Francus and Karabanov, 2000; Francus, 2001; Francus et al., 2002; Naruse and Masuda, 2006; Lewis et al., 2007), longer, relatively easily measured indices such as grayscale (Ojala and Francus, 2001), or longer qualitative analyses (Dean et al., 1999). To avoid the tedious and potentially error-prone nature of manually statistically processing images, an automated process is needed (Soreghan and Francus, 2004).

We present a macro called '*binary_traverser*' that calculates a suite of statistics that describe the texture and structure of sediment for a series of user-defined regions of interest (ROI) within BSEI. The macro can be used with lacustrine, marine and aeolian sediments. Parameters that can be measured from the particles include area, major and minor axes, aspect ratio, circularity, and angle. It currently contains over 600 lines of code.

The system described here has several unique advantages. Specific particle counting rules are implemented that allow each particle to be counted once, allowing small ROI with touching edges to be analyzed (Russ, 2002). The system can also run in a mode that quantifies the area of disturbed sections of ROI. When disturbance in an ROI exceeds a user-defined threshold, statistics from that ROI can be rejected. Finally, the macro and code are freely available under a

Creative Commons License[1]. It runs in ImageJ (Rasband, 2008), which is available for Windows, Macintosh, and Unix-based operating systems (requires ImageJ version 1.41o or greater), with no additional hardware requirements.

The first part of this manuscript is a general description of the system. The second section presents examples of data it produces. The Discussion section briefly describes previous automated image analysis systems, highlighting the unique features of '*binary_traverser*'. As '*binary_traverser*' allows extremely small ROI to be analyzed, issues related to small sample sizes are also discussed.

Detailed step-by-step instructions for running the macro are included in Appendix B. A description of the input files required, and the output files produced, is included in Appendix C. Four additional macros written in the ImageJ programming language are also included in Appendix D. These macros help the user construct images suitable for analyses. All of this material, including the macro source code and examples of input files, images and output, is available at http://www.geo.umass.edu/climate/lewis/analysis/.

5.3 General description

ImageJ (Rasband, 2008) is an image analysis package that is open, free, widely used, multi-platform, well-documented, and well-supported. ImageJ can be downloaded at http://rsb.info.nih.gov/ij/download.html. Five ImageJ macros are available at

[1] An automated system for the statistical analysis of sediment at the micro scale' is licensed under a Creative Commons Attribution-Noncommercial-Share Alike 3.0 Unported License.

http://www.geo.umass.edu/climate/lewis/analysis/. The macros are small uncompiled ASCII text files, and users with minimal programming experience can rapidly make their own modifications, verify the algorithms, and run them. Four of the macros, '*enhancement*', '*threshold_pause*', '*watershed_fillholes*', and '*ROI_imager'* (http://www.geo.umass.edu/climate/lewis/analysis/other_macros/other_macros.html) are small tools for efficiently preparing images for analysis by the main macro, '*binary_traverser*' (Fig. 5.1).

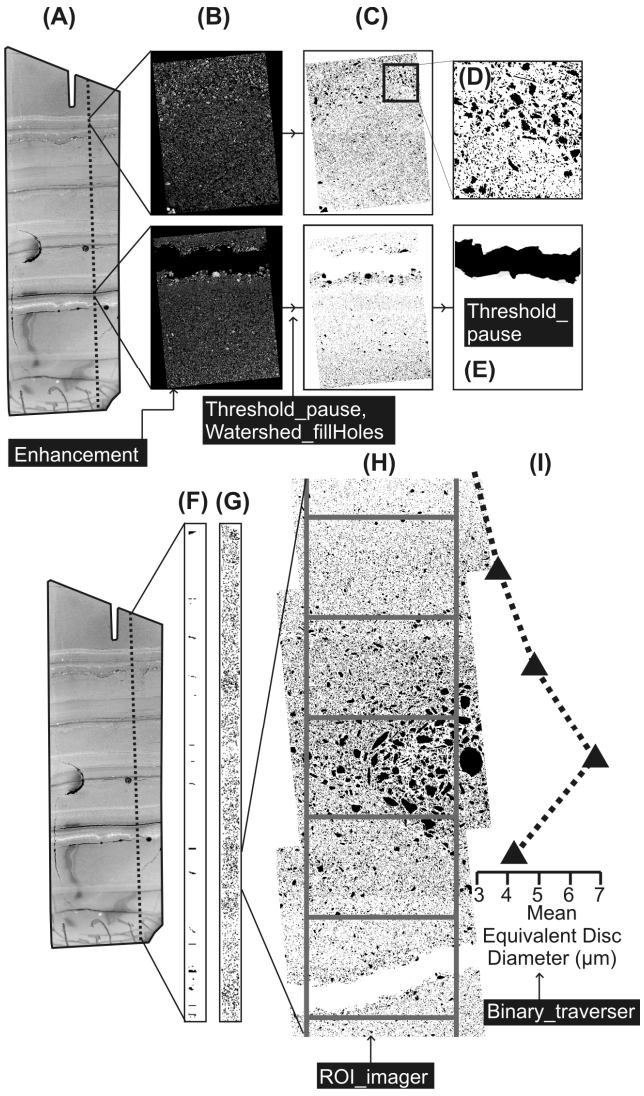

Figure 5.1. Steps for producing results from '*binary_traverser*'. (A) Flatbed scan of a thin section under cross polarized light containing a sequence of varves from Lake Tuborg, Ellesmere Island. (*continued*)

The image is 6.4 cm long along its left edge. Fifty four BSEI were obtained in a continuous transect, with overlapping tops and bottoms (dotted line). (B) Examples of BSEI from two locations of the thin section. The upper image is a typical image of light gray clastic grains surrounded by dark gray and black matrix. The lower image shows where a crack formed near a clay cap. Images are 1.4 mm high. The '*enhancement*' macro ran the ImageJ 'enhance contrast', 'sharpen', and 'median filter' algorithms on the BSEI (C) Binary images from the BSEI in 'B'. '*Threshold_pause*' and '*watershed_fillholes*' were used to produce the binary images. (D) A close-up of clastic grains in a binary image. The image is 315 µm high. (E) A binary image of a crack, produced with the '*threshold_pause*' macro, suitable for analysis by '*binary_traverser*' (see the left branch of Fig. 5.2). The image is 1.4 mm high. (F) Mosaic of 54 binary 'crack' images and (G) mosaic of clastic grains. (H) An image of five ROI produced with '*ROI_imager*'. ROI are 75 µm high, and the coordinates were carefully chosen to not extend beyond the border of BSEI. (I) Results from '*binary_traverser*' for the ROI shown here. Statistics from the bottommost ROI were excluded because of disturbance associated with the crack. The equivalent disc diameter is the calculated diameter of a particle using its cross-sectional area, assuming the particle is a perfect sphere (Francus, 1998). See Fig. 5.5 for the complete results from this thin section.

The macro '*enhancement*' prepares images for thresholding by running median filters, enhancing contrast, and the ImageJ 'sharpen' algorithm (Nederbragt et al, 2004; Rasband, 2008). '*Threshold_pause'* opens a BSEI image, pauses while the user selects appropriate upper and lower graylevel histogram limits (Nederbragt et al, 2004), automatically creates a binary image based on the chosen histogram limits, and saves the binary image. This sequence is repeated for all files in a directory. It produces uncompressed binary (1-bit) images, with particles as black (graylevel=255), and matrix and background as white (graylevel=0; Fig. 5.1 C, D, H). '*Watershed_fillholes*' sequentially opens all files in a directory (images must be binary), separates touching particles using the ImageJ watershedding algorithm, and fills in holes in particles (white pixels completely surrounded by black pixels; Nederbragt et al, 2004). Finally, '*ROI_imager*' opens a binary image and a text file containing ROI coordinates, and draws the ROI on the image. This is useful when preparing a ROI coordinate file for '*binary_traverser*' (Fig. 5.1 H).

The rest of this manuscript provides a description and examples of 'binary_*traverser*'. The macro produces a suite of statistics for several parameters that describe sediment texture and structure for user-defined ROI. A step-by-step description of '*binary_traverser*' is shown in Fig. 5.2. For input, the macro uses a binary image of particles (Fig. 5.1 G, H) and a text file containing a sequence of coordinates of box-shaped areas on the image. These are the ROI, and subsequent

analyses are performed on particles that fall within the ROI. In its normal running mode, the macro can produce two types of output. The first type is a single file containing summary statistics, with each row containing statistics for each ROI in its columns. The second output type is a series of text files, one for each ROI. Each text file contains the 'raw' measurements for each particle within that ROI. '*Binary_traverser*' can also run in a mode that quantifies the disturbed areas of binary images (described at the end of this section).

'*Binary_traverser*' is designed to be run on long mosaics of BSEI. BSEI are sometimes continuously acquired along the long axis of a thin section, perpendicular to stratigraphy, with short overlaps at the image tops and bottoms. These images can be stitched together to form a long mosaic in image editing software (Fig. 5.1 F, G, H). '*Binary_traverser*' can calculate continuous measurements long the long axis of an image mosaic (Fig. 5.1 H, I).

Hundreds of ROI can be automatically analyzed by the macro. ROI can have touching edges for a continuous stratigraphy (Fig. 5.1 H), or can be non-continuous. Non-continuous ROI may be advantageous where disturbances need to be bypassed, where biogenic laminae exist, where diagenetic alteration has occurred, or where continuous stratigraphic information is not required (e.g. from a homogenized sediment trap; see the Discussion section for a caveat).

A major strength of the macro is its ability to accept ROI that are very small relative to the particle size, which allows for extremely high resolution sampling. Special particle counting boundary rules are implemented that allow particles to be counted only once (Fig. 5.3; Russ, 2002). A particle is counted and measured if its center of gravity is within the top or left ROI edges. It is not counted or measured if its center of gravity is below the bottom ROI boundary, or if the particle touches the right ROI boundary. Therefore, if a particle straddles two ROI with a common boundary, it is counted only once (Fig. 5.3).

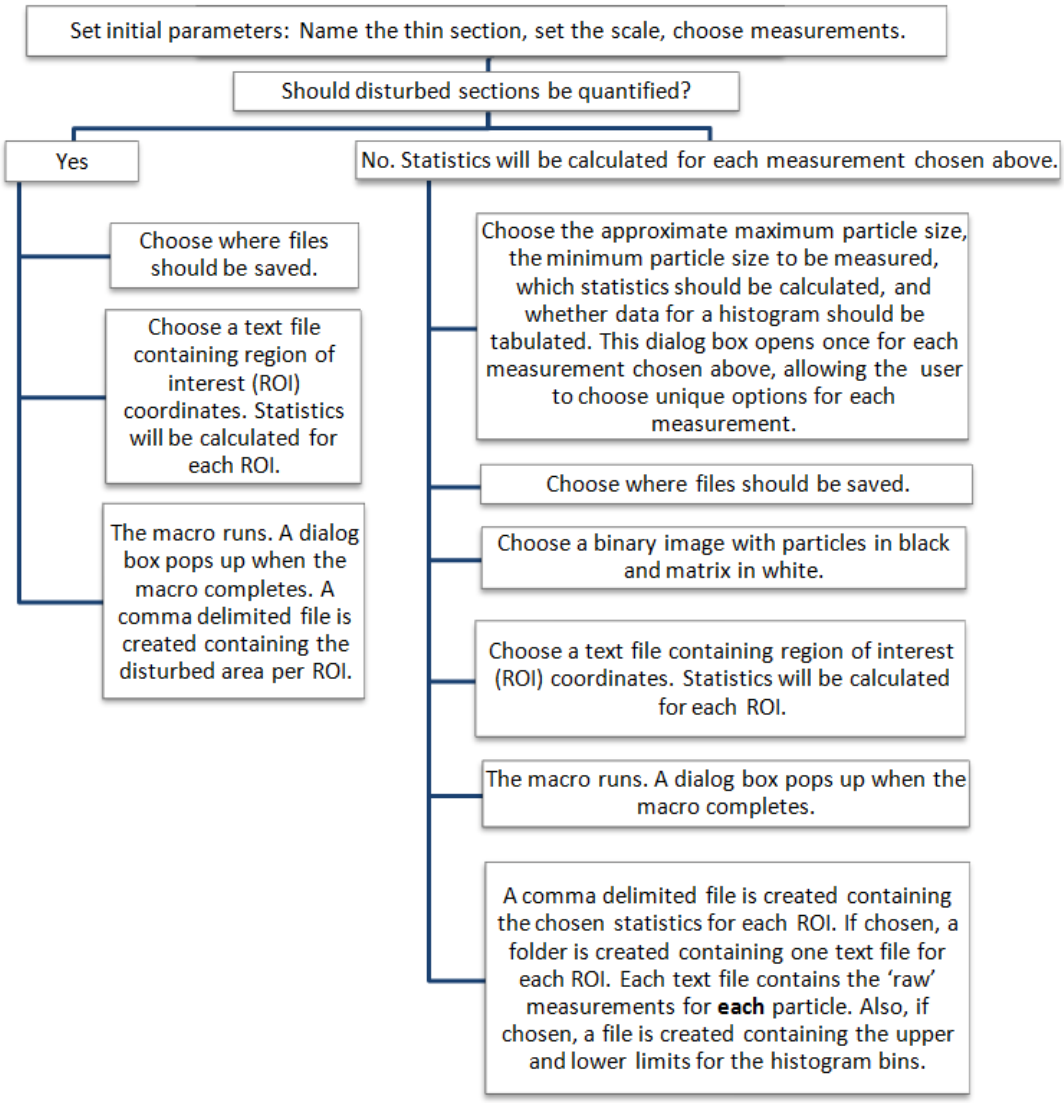

Figure 5.2. Flowchart summarizing the input and output of '*binary_traverser*'. The macro runs in a mode that quantifies disturbed areas of a thin section, and in a mode that calculates user-defined statistics for regions of interest. The output from both branches can be merged, and statistics calculated from disturbed sections can be discarded or flagged.

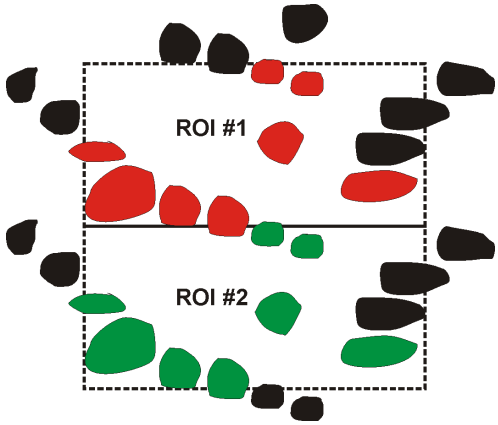

Figure 5.3. Particle counting rules implemented in '*binary_traverser*' (Russ, 2002). Red particles are counted and measured in ROI #1, green particles are counted and measured in ROI #2, and black particles are not counted or measured.

Statistics can be calculated for particle area, major and minor axes, aspect ratio, circularity, and angle. The desired parameters are chosen during an initial setup procedure (Fig. 5.2). The circularity parameter should be used cautiously, since it is strongly affected by pixilation and is sensitive to magnification (Francus and Pirard, 2004). Aspect ratio may give a more robust estimate of the roundness of a particle.

After the setup procedure, the macro loops automatically through the chosen parameters, and no further user-interaction is required. One statistics file is output for each chosen parameter, and each file contains statistics for all ROI.

The statistics in these files are user-definable, but can include number of particles, cumulative area, mean, median, mode, maximum, minimum, standard deviation, skewness, and kurtosis. Statistics are based on the method of moments technique. Five percentiles can be defined by the user, and to facilitate the construction of histograms, particles are counted in 'bins' with user-defined boundaries. Statistics files are comma delimited, and are easily opened in a spreadsheet. If statistics other than those provided by the macro are required, the user can also have measurements for each particle within each ROI saved in individual files.

Finally, the macro can also be run in a mode that quantifies disturbed sections of images. In this mode, the ROI coordinate file is accepted as input, and the area of disturbances per ROI is produced in a text file (Fig. 5.2, left branch). In this mode, the macro should be run on BSEI that have been thresholded and edited to produce black pixels for matrix and cracks, and white pixels for particles (Fig. 5.1 E, F).

5.4 Examples

Results are presented from Lake Tuborg and South Sawtooth Lake on Ellesmere Island in the Canadian High Arctic, and Saanich Inlet, a silled fiord on southern Vancouver Island. Sediments in both lakes are dominated by clastic grains, but the texture and structure of the resulting deposits are quite different. Sediments from Saanich Inlet consist of diatomaceous laminae alternating with clastic-rich laminae.

5.4.1 Methods

Cores were split and subsampled, and thin sections were made according to methods in Francus and Asikainen (2001; Table 5.1). Eight-bit grayscale images were enhanced with the following algorithms: increase contrast, median filter, and 'sharpen' (Francus, 1998, Soreghan and Francus 2004, Rasband, 2008). Images were then individually thresholded to produce binary images using the '*threshold_pause*' macro. Mosaics of overlapping images were produced in Adobe Photoshop® CS2 (Fig. 5.1).

Table 5.1. Metadata related to coring, imaging, and measuring.

	Lake Tuborg	S. Sawtooth Lake	Saanich Inlet
Coring technique	Ekman dredge	Vibracore	Piston Core
Coring depth (m)	74	82	224
SEM	JEOL JSM-5410	JEOL JSM-5410	Zeiss Evo 50
Working distance (mm)	20	20	17.5
Beam strength (kV)	20	20	15
Image Size (pixels; wxh)	1923x2650	2048x1536	1506x2048

5.4.2 Lake Tuborg

5.4.2.1 Site Description

Lake Tuborg, on Ellesmere Island, is a large glacially fed lake with an area of about 42 km^2 (Fig. 5.4A). The lake receives hydrologic and suspended sediment inputs from snowmelt and glacially fed streams. Relatively coarse suspended sediments are transported by overflows, interflows, and underflows, while finer clay-sized particles are deposited slowly over winter, forming a clay cap that marks the upper boundary of a varve, and hence defines the annual cycle of deposition in the lake (Smith et al., 2004; Lewis et al., 2008). Abnormally thick varves and a group of high energy sedimentary deposits are deposited by at least two processes: jökulhlaups and supraglacial lake drainage (Braun et al., 2000; Lewis et al., 2007). These deposits have been extensively studied; however, in this paper we focus on the characteristics the annual sedimentary cycle, which is the more typical style of sedimentation in the lake.

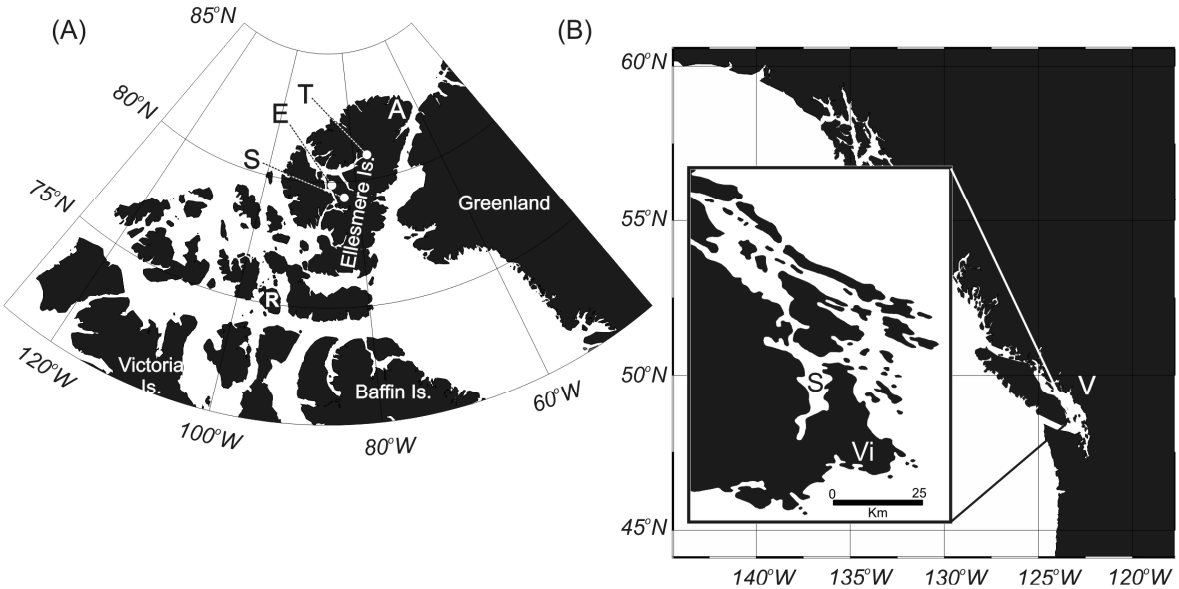

Figure 5.4. (A) Map of the Canadian High Arctic, showing Lake Tuborg 'T' and South Sawtooth Lake 'S' on Ellesmere Island. Also shown are the military bases at Eureka 'E' and Alert 'A', and the hamlet at Resolute Bay 'R', Cornwallis Island. Resolute Bay and Eureka are 630 km apart. (B) Saanich Inlet 'S', southern Vancouver Island. Victoria 'Vi' and Vancouver 'V' are marked.

5.4.2.2 Results

The images on Fig. 5.5 are flatbed scans of a thin section under cross-polarized light. Dark laminae are either layers of clay-sized particles or cracks. '*Binary_traverser*' was first run in the mode that quantifies disturbed sections (Fig. 5.1 E, F; Fig. 5.2, left branch), and data were excluded if an ROI contained more than 20% cracks. The equivalent disc diameter (EDD) is the calculated diameter of a particle using its cross-sectional area, assuming the particle is a perfect sphere (Francus, 1998).

The EDD record and thin section image shows a sequence of five varves (Fig. 5.5a). Several of these varves generally have classic fining upward internal structure. This fining upward could record energetic coarse-grained deposition at the beginning of each melt season, followed by a progressive decrease in grain size as flow wanes and competence decreases. This fining upward ends at clay caps, representing slow settling of clay-sized particles over winter.

Additional paleoenvironmental information is gained by examining divergences from this idealized pattern. Coarse deposits near the base of a varve (ex. V1, V5) could represent deposition during early season nival-generated peak flow, or before peak flow, when coarse grained sediment is flushed (Hodder et al., 2006). Coarse deposits in the middle of a varve (ex. V3) could represent a summer rainfall event (Hambley and Lamoureux, 2005). Coarse deposits at the top of a varve (ex. V1) could represent melt-out of niveo-aeolian material through lake ice (Lewis et al., 2002). Lewis et al. (2007) showed that annual and interannual variations in particle size determined by image analysis were consistent across multiple cores at Lake Tuborg, which aided stratigraphic correlations.

Results from an extremely high resolution transect of ROI through a single varve are presented in Figure 5.5b. At the base of the varve, a brief coarsening upward section is evident at about 51 mm depth. Above this, there is a long fining upward sequence, until a coarse-grained layer is encountered at about 42.5 mm depth. The particle size of clay caps are not well quantified

using BSEI. Clay particles form amorphous mats, and individual particles cannot be discriminated.

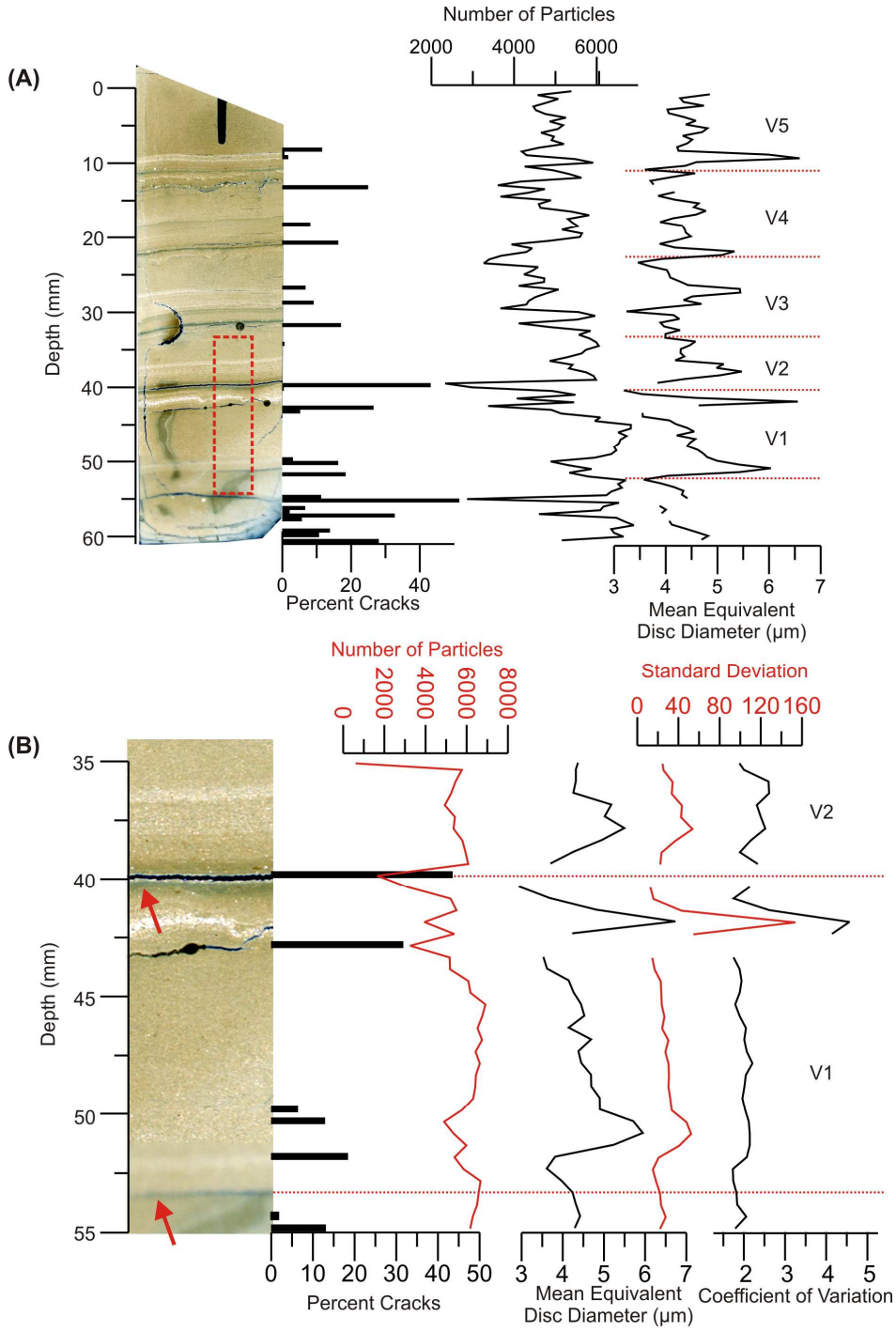

Figure 5.5. Varves from the freshwater basin of Lake Tuborg. (A) A 60 mm section showing five varves (V1-V5). The image is a flatbed scan of a thin section under cross polarized light. A series of (*continued*)

54 BSEI images were stitched together to produce a mosaic (Fig. 5.1 G), and the macro performed measurements on 121 ROI. Measurements were obtained every 750 microns, and there are 122 measurements over the 61 mm sequences. Red lines mark clay caps. Equivalent disc diameter measurements from ROI containing greater than 20% cracks were excluded. The red dashed box in the thin section image is expanded in 'B'. (B) A 20 mm close up of one varve. Measurements were obtained every 75 microns, and ROI were 3.75×10^4 μm^2. There are 41 measurements over the 20 mm sequence. Dashed lines and red arrows mark clay caps.

'*Binary_traverser*' was able to produce statistics at a higher spatial resolution than is possible with laser diffraction, X-ray, or hydrometer techniques, and with less effort than manually interpreting BSEI. This allowed the annual sedimentary cycle to be interpreted, and allowed interannual events to be inferred.

5.4.3 South Sawtooth Lake

5.4.3.1 Site Description

South Sawtooth Lake is a small snowmelt-fed lake on the Fosheim Peninsula of Ellesmere Island, 85 km southeast of Eureka (Fig. 5.4A). At its widest and longest, the lake is 4.2 x 1 km, and its watershed is 47 km^2. The stream that feeds the lake follows a typical nival regime (Prowse, 1990). The majority of annual sediment transfer occurs during a brief period of peak snowmelt (Lewis et al. 2005). The annual nival sediment pulse, followed by a long period of fluvial quiescence, produces annually laminated sediment at the lake bottom (Francus et al., 2008). However, rare events episodically transport large volumes of sediment, and a graded deposit from one of these events is analyzed here. Graded deposits at South Sawtooth Lake could be produced by mass movements (Lewis et al., 2005) or pluvial events (Francus et al., 2008).

5.4.3.2 Results

Data presented in Figure 5.6 are based on measurements of particle area. This sequence likely records deposition from a hyperpycnal flow, perhaps generated by a precipitation event. Beginning at the bottom of the sequence, above the crack, a 0.5 mm sequence of fine grained sediment grades upward. This reverse grading could represent a brief period of waxing flow on the rising limb of a storm hydrograph (cf. Francus et al., 2008). Next, particle size increases abruptly, and grading becomes normal. Three coarse grained laminae are found within the coarsest particles at the base of the normally graded sequence, between about 6.5 and 5.5 mm depth. These pulses are particularly well represented by the particle weight distribution histogram (Beierle et al., 2002), and are also visible as discrete kurtosis peaks. These could represent underflow pulses (Best et al., 2005). Above these laminae, the standard deviation and coefficient of variation decrease upward, indicating better sorting. These grading and sorting trends are typical of turbidite deposits, where poorly sorted coarse bases are deposited in the head and body of the flow, and deposits fine and become better sorted when flow wanes and deposition occurs through particle settling (Reading, 1996).

The number of particles within each ROI falls sharply between 3.5 and 2 mm depth; each 75 x 3000 µm ROI only contains 10-20 particles above this transition. The majority of particles in this zone are too fine to be discretely imaged using a SEM, and cannot be measured (Francus and Pirard, 2004). One coarse grained particle in this zone creates a coarse spike at 2 mm depth. This particle is marked with a white arrow on the SEM image on Figure 5.6. It is perhaps a small dropstone from the overlying lake ice. This particle is extremely evident in the data because of the low number of imaged fine-grained particles within its ROI. Caution is needed in the interpretation of single statistical descriptors of particle size, particularly where sample size is low and distributions are polymodal (see Discussion; Beierle et al., 2002).

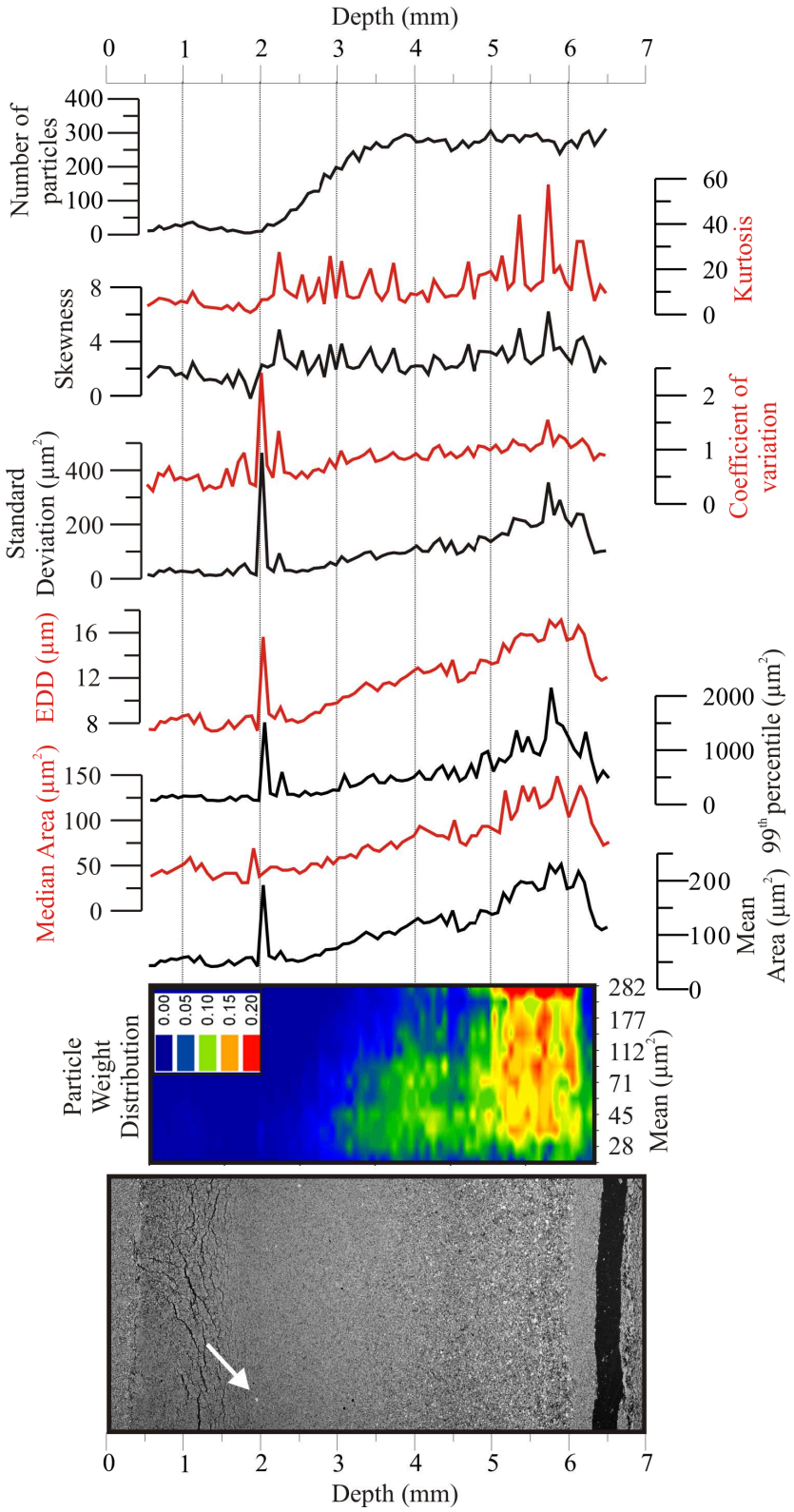

Figure 5.6. A graded sequence from a vibracore obtained in the distal basin of South Sawtooth Lake, showing statistics based on particle area. The image is a mosaic of backscattered scanning electron microscope images, with a crack introduced by the freeze drying process at around 6.5 mm depth. Measurements were obtained every 75 microns, ROI were 2.3 x 10^5 µm^2, and there are 81 ROI over the 6.5 mm long sequence. EDD is equivalent disc diameter (Francus, 1998). The surface plot shows histograms for each sample (Beierle et al., 2002). The Z-scale is weight per histogram bin, calculated using the density of quartz and EDD. Histogram bin spacing progresses $\log_{10}$. The white arrow on the image points to an isolated large grain separated by fine-grained matrix.

The advantages of using '*binary_traverser*' in this case were the ability to quantify extremely high resolution changes in the direction of grading, and to detect thin laminae that are not visually apparent. The suite of statistics produced also allowed outliers in particle distributions to be identified.

5.4.4 Saanich Inlet

5.4.4.1 Site Description

Saanich Inlet is a 25 km long, 250 m deep fiord off south Vancouver Island, British Columbia (Fig. 5.4B). Bottom water anoxia is promoted by a 70 m sill at its outlet and decomposition of organic matter that settles from the photic zone. This anoxia allows the deposition and preservation of annual laminae consisting of a winter layer rich in fluvially-generated clastic sediments, and a summer diatomaceous layer. Under cross-polarized light, the biogenic-rich winter layers are a dark olive green, and the clastic-rich summer layers are a lighter tan color (Fig. 5.7).

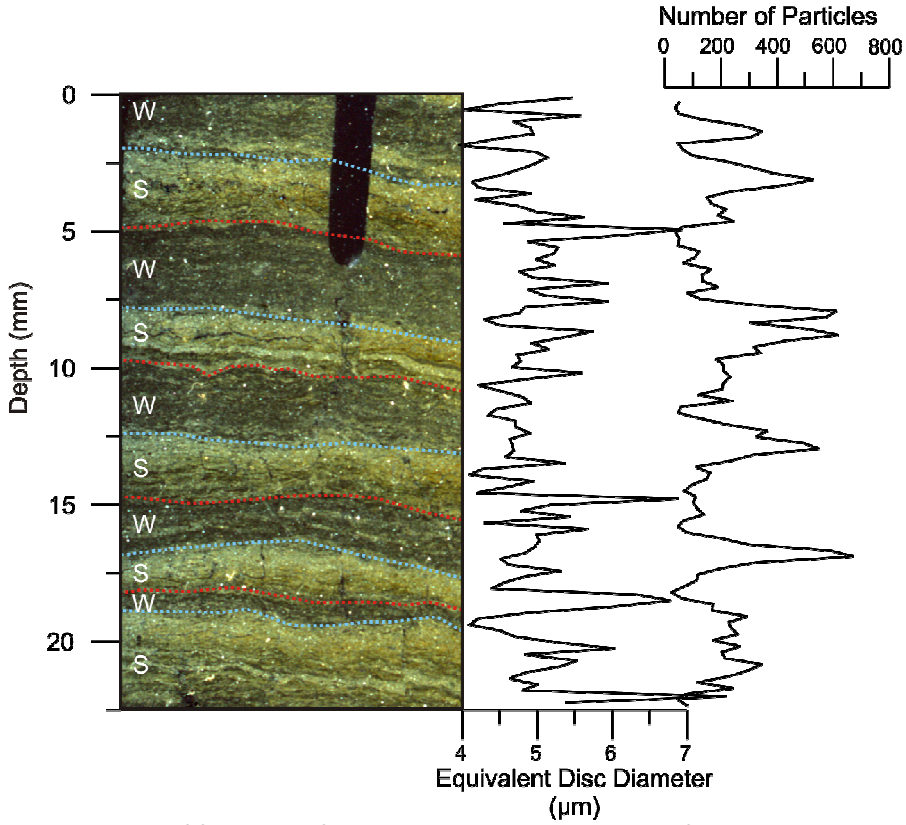

Figure 5.7. A sequence of five varves from Saanich Inlet. The image is a flatbed scan under cross-polarized light. Winter (W) and summer (S) deposits are marked. Blue lines mark the boundaries between underlying terrigenous-dominated laminae and overlying biogenic-dominated laminae. Red lines mark the boundaries between underlying biogenic-dominated laminae and overlying terrigenous-dominated laminae. Measurements are every 220 µm, ROI area is 3.8 x 10^5 µm^2, and there are 102 measurements over the 2.3 mm sequence.

5.4.4.2 Results

The biogenic fraction was removed from analyses, as the objective is to investigate hydroclimatic influences on clastic sedimentation. Biogenic-rich material appear darker on BSEI images than clastic grains, because of its lower atomic number (Soreghan and Francus, 2004), allowing biogenic material to be automatically segregated based on its grayscale value using the '*threshold_pause*' macro.

While summer laminae are dominated by biogenic material, they do contain a large number of clastic grains. However, summer clastic material tends to be finer grained than winter

clastic material (Fig. 5.7). Precipitation at Victoria, British Columbia, is highest during winter, resulting in annual discharge peaks to the rivers feeding Saanich Inlet (Hydat, 2005). This produces the thick, relatively coarse grained clastic-dominated winter layer. Figure 5.7 also shows a general inverse relationship between particle size and number of particles, reflecting the dominance of numerous fine grained clastic particles in summer deposits (Fig. 5.7).

5.5 Discussion

Several systems for the automated statistical analyses of images have been published (e.g. Peach and Perrie, 1975; Van Den Berg et al., 2003; Seelos and Sirocko, 2005). The Peach and Perrie (1975) method involves obtaining a sediment sample, suspending it, and physically and chemically disaggregating it. The sample is then mounted on a gelatin coated microscope slide, and a computer counts and measures grains on the microscope slide. The Van Den Berg et al. (2003) and Seelos and Sirocko (2005) methods use images obtained with transmitted light microscopes to acquire particle measurements. Although thin section mounts are typically ground to about 30 µm thickness, images from transmitted light microscopes show particles that vertically overlap, and special statistical techniques are required to overcome this. In addition, the lowest measureable particle size with transmitted light microscopy is 20-30 µm (Van Den Berg et al., 2003; Seelos and Sirocko, 2005). This is problematic for lacustrine particle size distributions, where silts are commonly the modal class.

Despite the automation of '*binary_traverser'*, the user should take caution regarding the number of particles in ROI. Several authors have cited minimum numbers of particles that should be present. For example, Cheetham et al. (2008) cite 300 grains, Naruse and Masuda (2006) indicate 250 to 1100 grains, and Van Den Berg et al. (2003) cite 1000 to 1200 grains. We see no statistical reason for a constant minimum number of grains, so long as two caveats are met.

First, a given measurement of a small area cannot be scaled up to describe an area larger than itself. This is called a sample support problem (Anguy et al., 1994). If '*binary_traverser*' is used to produce continuous stratigraphies, with the goal of obtaining high resolution paleoenvironmental information, then this is not an issue. However, if it is used to provide point measurements, for example from a sediment trap, then sample support issues should be considered. The sample support problem could be assessed with '*Binary_traverser'* by constructing a text file containing coordinates of multiple adjacent ROI with varying scales, and the variability of the produced statistics could be assessed (Anguy et al., 1994).

Second, the distribution of a measurement must be normal, which allows the use of parametric statistics. As the sample size decreases, the tendency towards normality may increase if the ROI height is less than lamina height (Van Den Berg et al., 2003). Alternatively the tendency may decrease if the ROI contains outliers (Section 5.4.3.2). '*Binary_traverser*' outputs the number of particles per ROI, and includes an option where measurements for each particle within an ROI can be output to a text file. This allows the Shapiro-Wilk test, the Kolmogorov–Smirnov test, or any other normality test to be run.

5.6 Conclusion

A system has been presented that can produce extremely high resolution records of particle texture. Results have been shown from clastic and biogenic dominated sedimentary environments, and from inter- and intra-annual sedimentary sequences. Its key advantages are its ability to produce accurate results on very small ROI, to quantify the silt-sized fraction, to run unattended, and its open and free source code and parent program, ImageJ.

5.7 Acknowledgements

Wayne Rasband and the National Institute of Health maintain and support ImageJ. Mark Besonen selflessly provided expertise on scanning electron microscopy and the ImageJ macro language. Kinuyo Kanamaru provided sediment imagery and guidance on Saanich Inlet sediments. The Polar Continental Shelf project provided the logistics that made collecting sediments at South Sawtooth Lake and Lake Tuborg possible. This research was supported by National Science Foundation (NSF) grant ATM-9708071, ATM-0402421, ARC-0454959, NSF Doctoral Dissertation Research Improvement Award 0221376, Geological Society of America graduate student grants, an Arctic Institute of North America grant-in-aid, and the Gloria A. Radke prize from the University of Massachusetts.

CHAPTER 6

CONCLUSIONS

This research has aided the discipline by documenting the annual sedimentary cycle at Lake Tuborg, Ellesmere Island, Nunavut. It has also demonstrated the benefits of limnologic process studies. Lacustrine monitoring before, during, and after the 2003 jökulhlaup allowed the type and extent of jökulhlaup-derived processes and deposits to be identified in Lake Tuborg. Equally importantly, it allowed processes and deposits to be characterized from events such as the drainage of supraglacial lakes.

This work culminated in the identification of a characteristically thick fining upward deposit far from the point of jökulhlaup inflow in Lake Tuborg. The combination of the distance from inflow, the sill separating the freshwater from saltwater basins, the shallow bottom slope in the saltwater basin, and the density of the saltwater layer relative to the overlying freshwater meant that potentially erosive hyperpycnal flows did not progress into distal portions of Lake Tuborg. However, the long, straight shape of Lake Tuborg, the availability of sediment, and the large volume of the lake drainage, meant that even distal portions of Lake Tuborg received extreme amounts of sediment by overflow and interflow. It was also remarkable that the salinity and temperature of the bottom waters of Lake Tuborg were only subtly (but measurably) freshened and cooled. This work allowed a site to be identified where a conformable and distinctive jökulhlaup deposit formed, it allowed characterization of deposits at the site before and after the jökulhlaup, and allowed the processes responsible for these deposits to be documented.

Results from the limnologic process study allowed a long sediment core from the distal portion of Lake Tuborg to be examined for similar deposits. The sediment core was found to contain varve-like deposits, and the annual nature of the laminae was confirmed with 137-Cesium dating. The varves at the site are typically millimetre-scale and fine grained. Over a thousand varves were counted in the core sequence. Varves are interrupted by occasional very coarse

grained sand beds with sharp bases and tops. These cannot be jökulhlaup-derived deposits because any large jökulhlaup would create an overflow which would produce a thick fining upward sequence. They are more likely deposits from wind-blown sand that melts through the lake ice, slumps, or extreme fluvial discharge events.

Only three deposits in the thousand year sequence could be definitively identified as being jökulhlaup-derived. The first was in 1960, the second in 1993, and the third in 2003. This led to the conclusion that large jökulhlaups have only been occurring in the ice-dammed lake above Lake Tuborg since 1960. Before that time, the ice-dammed lake was likely draining exclusively by overtopping its ice dam. After that time, it has been draining catastrophically by englacial and subglacial conduits. Jökulhlaups have likely been triggered when lake level sufficiently rises to float the ice dam. Recent catastrophic drainages are likely a response to a combination of recent warming and ice-dam thinning.

This work has also aided the identification of lacustrine and marine processes at a subannual timescale using high resolution records of particle size. Previously developed techniques of the analysis of backscattered electron microscope imagery were implemented in a macro. The unique aspect of the macro is that it is capable of analysing stratigraphies at the micron-scale by implementing special particle counting rules, and it does this automatically, with minimal user-intervention. The macro should have broad applicability to lacustrine, marine, and aeolian sedimentary research, where extremely high resolution particle size records are necessary.

A growing body of research in the Canadian High Arctic shows that glaciers are receding and thinning (ex. Abdalati et al, 2004; Koerner, 2005). It therefore appears that jökulhlaups at Lake Tuborg will occur with increased frequency in the future. A visit to Lake Tuborg and the ice-dammed lake in 2006 showed that the glacial portal system had resealed, and the ice-dammed lake was refilling. The unexpected occurrence of the 2003 jökulhlaups meant that many of the jökulhlaup-derived glacial, hydrologic, and limnologic processes had to be inferred. Future work could involve placing a network of sensors in and around the ice-dammed lake and Lake Tuborg.

Precisely measuring the lake-level drawdown would yield accurate measurements of jökulhlaup discharge. Flow meters and moored CTD's above, below, and in the chemocline would yield an impressive dataset of the fluid dynamics of high energy processes propagating along density gradients. Above all, it would produce new information on the anticipated effects of near-future climate change in the Canadian High Arctic, both for glacier systems and for the expected evolution of lakes.

APPENDIX A

CESIUM, RADIUM, AND LEAD RESULTS

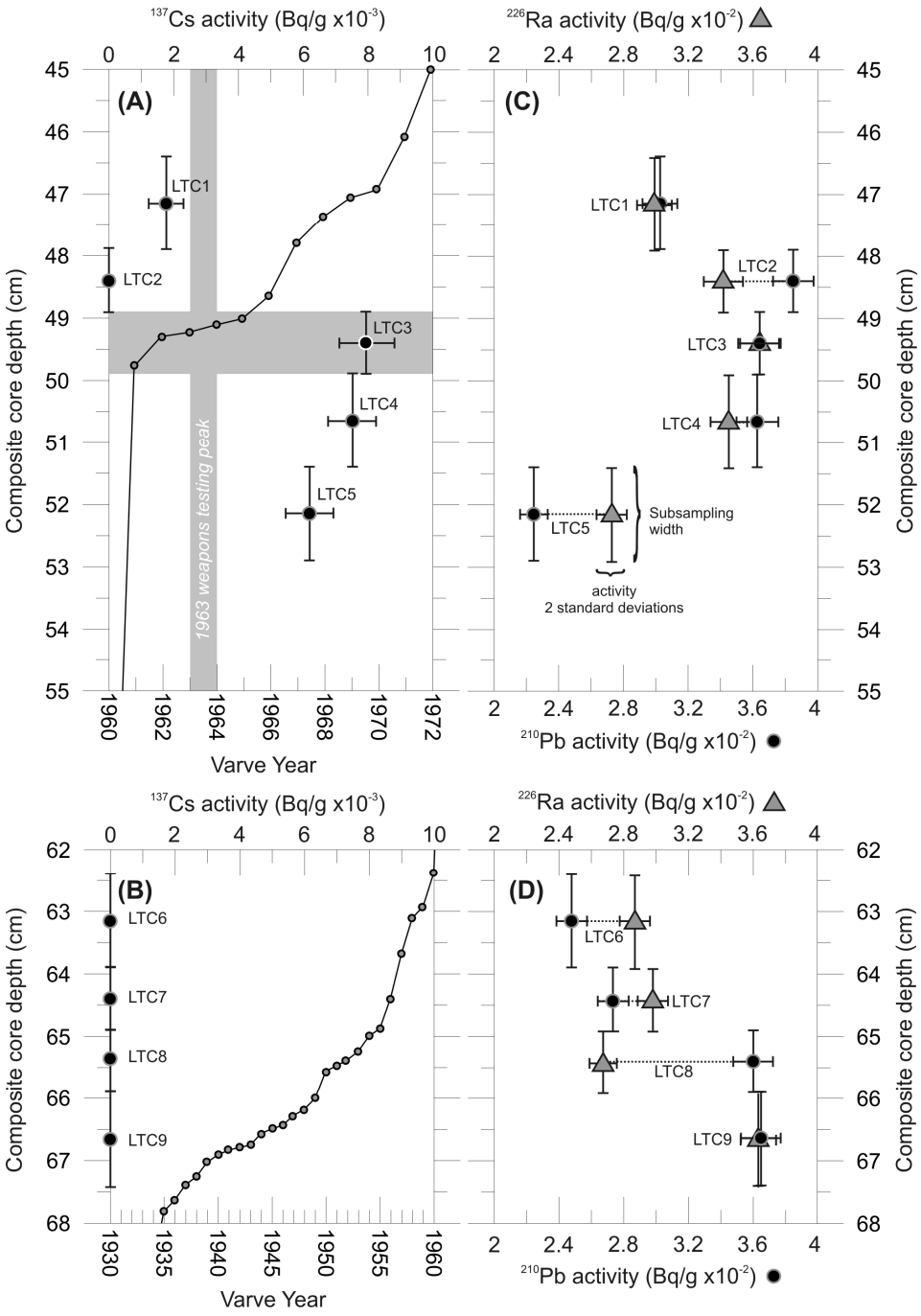

Figure A1. Cesium-137, Radium-226, and lead-210 results for all nine samples from the core sequence presented in chapter four.

APPENDIX B

DETAILED INSTRUCTIONS FOR RUNNING '*BINARY_TRAVERSER*'

- These instructions are also available at http://www.geo.umass.edu/climate/lewis/analysis/
- Install ImageJ from http://rsb.info.nih.gov/ij/download.html. The macro requires version 1.41o or greater.
- Load the macro in ImageJ by clicking Plugins > Macros > Install (or CTRL+SHIFT+M). The macro is called 'binary_traverser_v4.txt'.
- Run the macro by clicking Plugins > Macro, then choose the current version of the macro at the bottom of the menu (Fig. B1).

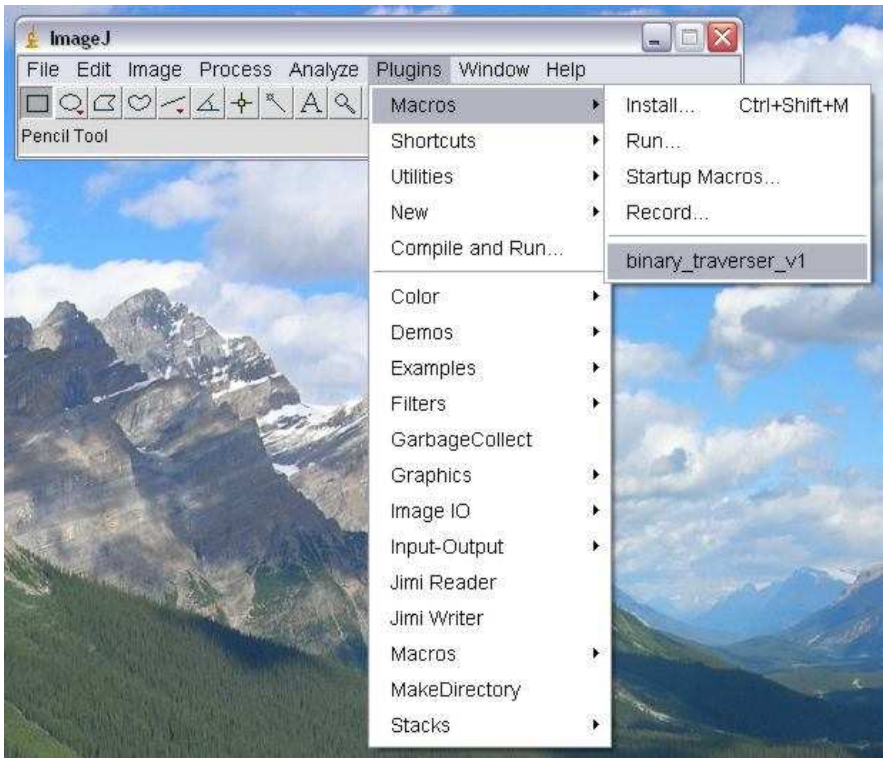

Figure B1. Loading the *binary_traverser* macro.

- You are presented with the following control panel (Fig. B2):

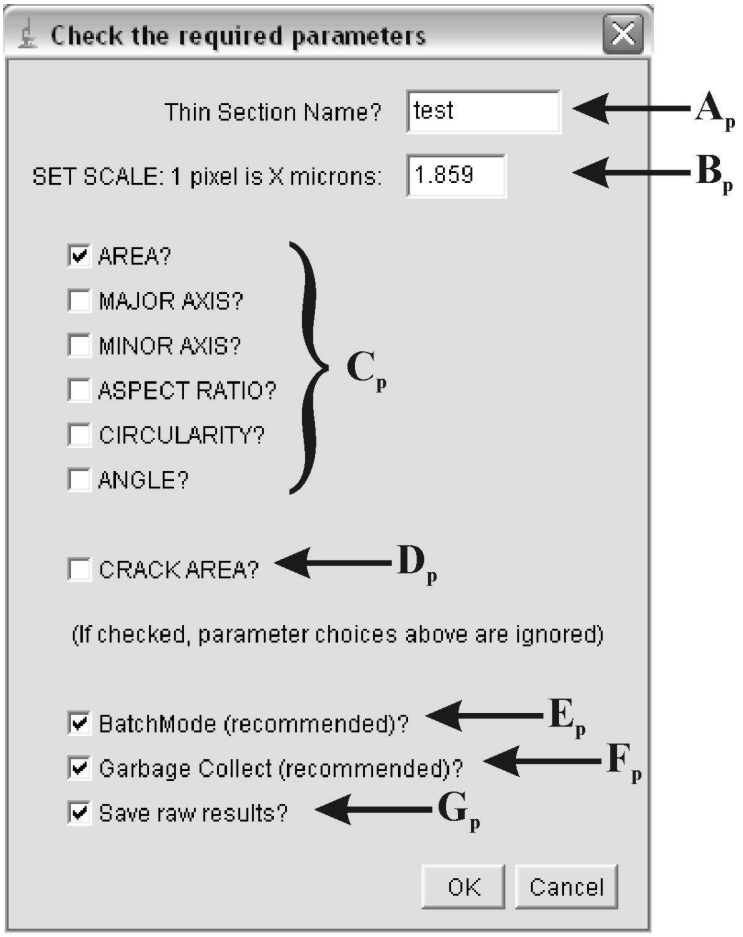

Figure B2. The parameter Control Panel

PARAMETER CONTROL PANEL:

All settings applied for each parameter: area, major axis, minor axis, aspect ratio, circularity and angle. This dialog is displayed once regardless of the number of parameters chosen.

A_p **– Thin Section Name:**

This is the name that will be used for naming output files and directories (Appendix C, parts 1-5). The macro quits if nothing is input into A_p.

B_p- **Set Scale:**

1 pixel represents this many microns. All output files use this scale.

C_p- Parameters

Possibilities include area, major axis, minor axis, aspect ratio, circularity, and angle.

Area: the particle area; output is in microns-squared;

Major axis: the primary axis of the best fitting ellipse, output is in microns.

Minor axis: the secondary axis of the best fitting ellipse, output is in microns.

Aspect ratio: 1-(MinorAxis/MajorAxis). Aspect ratio is 0 for a perfect circle (or square), and approaches one with increasing particle elongation.

Circularity: 4pi(area/perimeter^2). "A value of 1.0 indicates a perfect circle. As the value approaches 0.0, it indicates an increasingly elongated polygon." (from http://rsb.info.nih.gov/ij/docs/menus/analyze.html).

Angle: "the angle between the primary axis and a line parallel to the x-axis of the image." (from http://rsb.info.nih.gov/ij/docs/menus/analyze.html).

D_p- **Crack Area?**

Checking this box allows the area of disturbed areas on binary images to be quantified. Disturbed areas are typically cracks, but other disturbances can be quantified as well. The macro will ask for a 'binary crack image'. One way to construct such an image is to trace disturbances in black on a new layer in an image editing software package, then save only the traced image as a new file. Another way is to use the '*threshold_pause*' macro (Appendix D) and image editing software. If D_p is checked, then measurements chosen in C_p are ignored. The macro will also ask for an input file containing ROI coordinates. The input file should be the same structure as described in Appendix C, part 1. Only one output file is produced when the macro runs in this mode, and the file structure is described in Appendix C, part 5.

E_p**- Batch Mode?**

When this is chosen, the binary particle image is not shown on screen. If 'raw results (G_p) was chosen, then measurements are also not shown on the screen. The macro will complete in substantially less time when this is checked, particularly if G_p was chosen, and ImageJ will use substantially less memory.

F_p**- Garbage collect?**

If checked, this reduced the accumulation of leaked memory. This function is called at several strategic points in the macro. (Calls "java.lang.System.gc")

G_p **– Save Raw Results?**

Saves the 'raw' measurement data for each ROI in individual text files (Appendix C, part 4). By saving the raw results, the user can double check that the statistics are being calculated correctly, or additional statistics can be calculated. However, choosing this option makes a 'Log' window open on screen for each ROI while the particles are being measured. This increases the amount of time the macro needs to run.

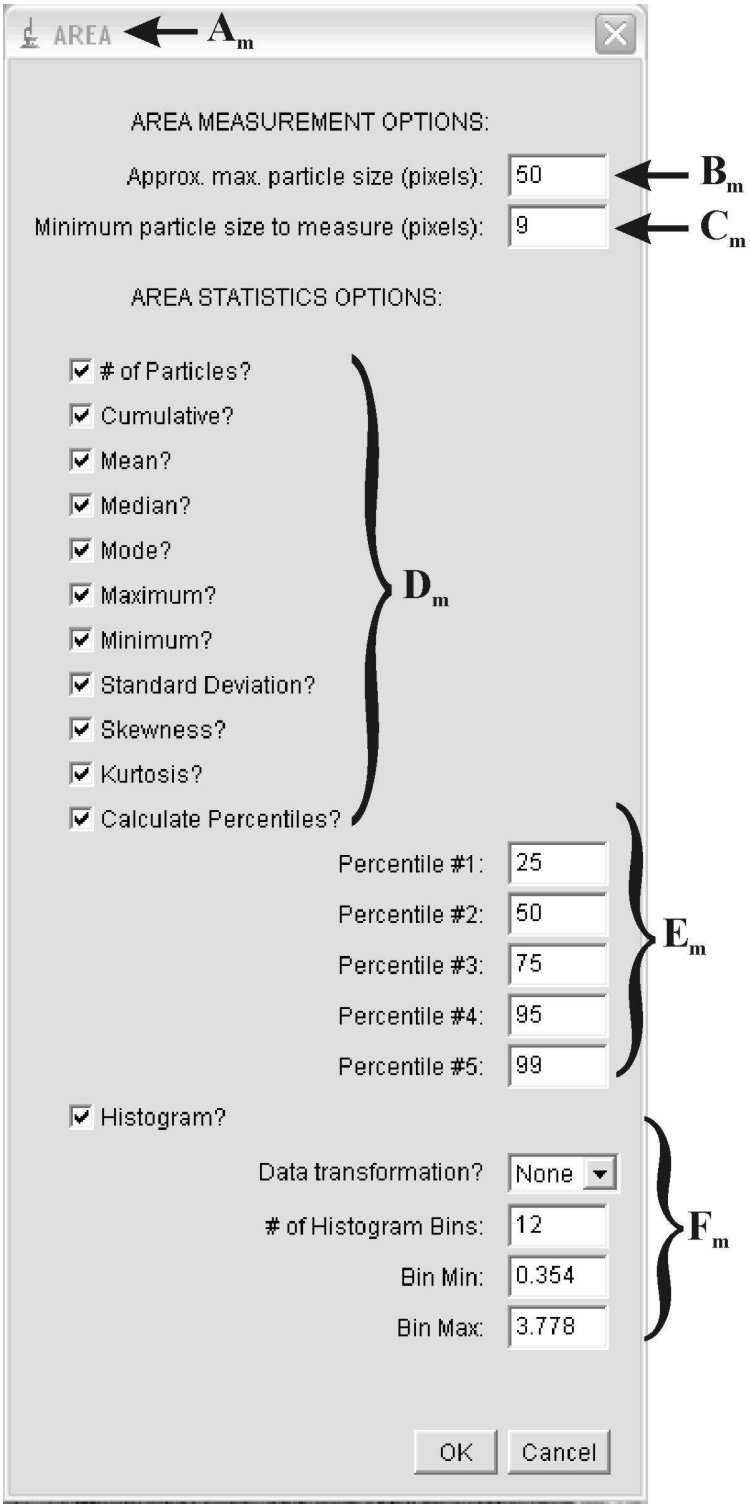

Figure B3. The measurement Control Panel

MEASUREMENT CONTROL PANEL:

This dialog box will appear once for each chosen parameter (area, major and minor axes, aspect ratio, circularity, or angle).

$A_{m=}$ **Measurement**

Area, major and minor axes, aspect ratio, circularity, or angle.

B_m**= Approx. Max Particle Size (pixels):**

Particle counting criteria are described in Chapter 5 (Fig. 5.3). Testing these boundary criteria for all the particles in a thin section would be very time consuming. Therefore, to save time, the macro builds a 'fat' ROI around the user-defined ROI, and only implements the boundary criteria within the fat ROI. The macro triples B_m, so, the user does not have to accurately estimate the largest particle; tripling B_m ensures that unless the user was very wrong, the big box will encompass all necessary particles (Fig. B4).

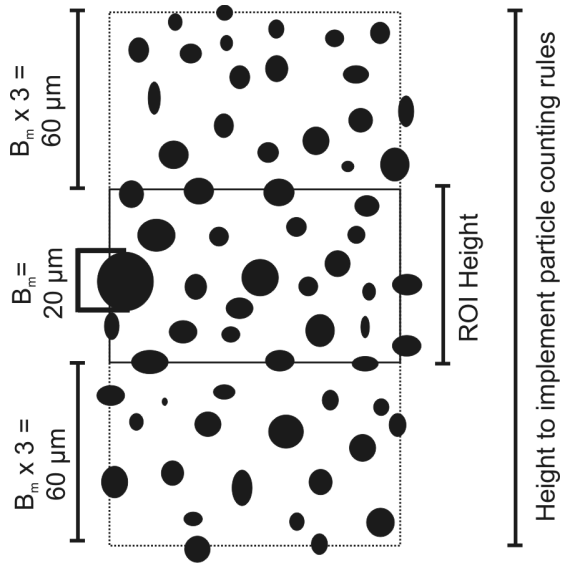

Figure B4. An illustration of how particle counting rules are implemented over a 'fat' ROI. The ROI height is increased by (B_m x3) x 2.

The advantage of using these boundary criteria is that ROI area can be very small in relation to particle area.

C_m**= Minimum particle size to measure (pixels):**

Enter an appropriate minimum number of pixels for the parameter being measured. Appropriate C_m varies for different parameters (*cf.* Francus and Pirard, 2004), and as such, it can be individually set for each parameter in each measurement box.

D_m**= Statistics Options:**

The checked statistics will be calculated. If unchecked, the appropriate column in CORENAME_PARAMETER_STATISTICS.txt (Appendix C, part 2) will contain 'NA'. Unchecking a statistic will only marginally speed up processing, so as a default, all statistics are checked.

E_m= **Calculate Percentiles?**

Input five desired percentiles here. For a description of the percentiles output, see Appendix C, part 2.

F_m = **Histogram?**

The user defines the upper and lower histogram bin boundaries (in pixels), the number of bins, whether the bin boundaries scale linearly or on a log scale.

Data transformation: Determines how data are manipulated before being placed in histogram bins. If 'None' is chosen, the data are not manipulated at all. If $\log_{10}$ is chosen, each measurement is log transformed before being placed in a bin. For 'phi', measurements are transformed to $-\log_2$ (Boggs, 1987). Phi or $\log_{10}$ transformation is recommended when dealing with negatively skewed distributions. Bin boundaries (see below) apply to the transformed data.

# of Histogram Bins: the number of bins between 'bin min' and 'bin max'.

Bin Min: The lowermost threshold to begin counting (explained in more detail in the histogram section of Appendix C, Part 2). If data transformation was chosen, then 'Bin Min' must reflect this.

Bin Max: The lowermost threshold to begin counting (explained in more detail in the histogram section of Appendix C, Part 2). If data transformation was chosen, then 'Bin Max' must reflect this**.**

CHOOSING FILE LOCATIONS:

After clicking 'OK' on the Measurement Control Panel, the user is asked where output files should be placed. This includes:

- a folder for raw data (Appendix C, part 4) if G_p was checked
- a file describing the upper and lower bin limits if the checkbox in F_m was selected (Appendix C, part 2).
- statistics files for each chosen parameter (Appendix C, part 2)

Next, the user is asked for the following input files:

1. A binary particle image.

   Tips:

   - All pixels should be black (grayscale value=255 or white (grayscale value=0). The image must be binary; there should be no gray pixels (grayscale values between 0 and 255).
   - The image must have no scale set (Fig. B5). If there is a scale set, go to the ImageJ menu Analyze > Set Scale. Choose 'Reset'. When done, 'Save As' the image, close then and reopen it.

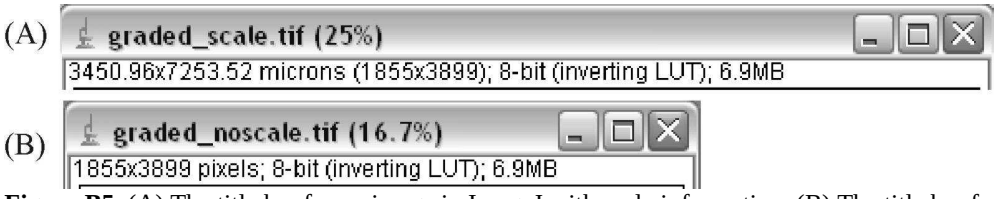

Figure B5. (A) The title bar for an image in ImageJ with scale information. (B) The title bar for an image in ImageJ without scale information.

2. A coordinate file containing the coordinates of each ROI (Appendix C, part 1).

Finally, the macro will run. A Log window indicating the length of time the macro took to run will pop up when finished.

APPENDIX C

INPUT AND OUTPUT FILES FOR THE IMAGE ANALYSIS MACRO

These instructions are also available at http://www.geo.umass.edu/climate/lewis/analysis/

Note:

X_p refer to 'parameters'. They are chosen in the parameter control panel (Appendix B, Fig. B2).

X_m refer to measurements. They are chosen in the measurement control panel (Appendix B, Fig. B3).

1– ROI coordinate input file:

EXPLANATION: The coordinates, in pixels, of the ROI.

Tips:

- this file can be created in, and exported from, a spreadsheet program.
- be sure there are no leading or trailing blank lines (Fig. C1).
- be sure that no ROI have no particles in them.
- To test your ROI coordinate input file, it would be a good idea to visualize your ROI before running the macro. This will help the user determine whether any ROI have no particles, and to be sure all ROI are properly positioned. A tool called '*ROI_imager*' is included to help you do this (Appendix D).

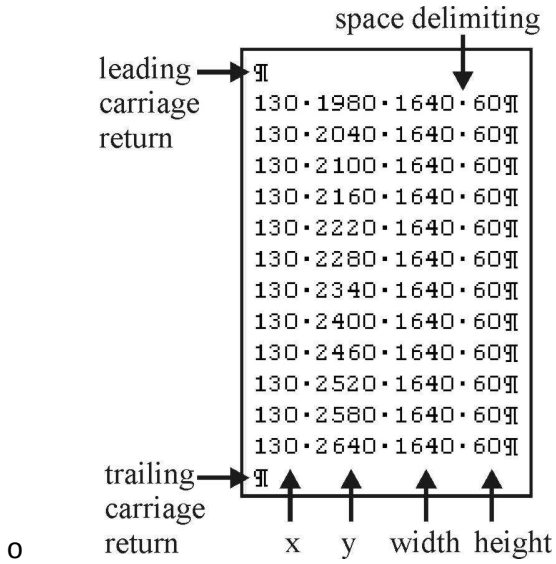

o

Figure C1. Coordinate file structure. The file should have no leading or trailing carriage returns or newlines.

FILE STRUCTURE:

Column 1: left edge of the measuring box x-coordinate

Column 2: top edge of the measuring box y-coordinate

Column 3: measuring box width

Column 4: measuring box height

2 - CORENAME_PARAMETER_STATISTICS.txt:

(e.g 3eg-1_AREA_STATISTICS.txt)

EXPLANATION: A comma separated file that is output by the macro after it runs. It contains the chosen statistics for each ROI. If applicable, units are in microns, or microns squared for area, as set in B_p.

FILE STRUCTURE:

X: left edge of the measuring box x-coordinate

Y: top edge of the measuring box y-coordinate

Width: measuring box width

Height: measuring box height

Area: measuring box area

Mid_Y: y-coordinate of the midpoint of the measuring box

Number_Parts: the number of particles within the ROI that satisfy the boundary criteria

Cumulative: the sum of all measurements of a parameter for an ROI. This only really makes sense for area, where you want to calculate % black pixels.

Mean: mean

Median: median (if the number of measurements is odd, then this is m_{50}. If the number of measurements is even, then the median is the average of the two middlemost measurements).

Mode: the most frequently occurring measurement. Numbers are rounded to the nearest integer for all parameters except aspect ratio and circularity. For aspect ratio and circularity, mode may not be useful, since numbers are reported to 4 decimal places.

Max: maximum number

Min: minimum number

StDev: standard deviation, where:

$$s = \sqrt{\frac{\sum (X_i - \overline{X})^2}{n-1}}$$

Skewness: where:

$$s = \frac{\sum (X_i - \overline{X})^3}{ns^3}$$

Kurtosis: where:

$$s = \frac{\sum (X_i - \overline{X})^4}{ns^4}$$

Perc#Value: The value of the percentile specified in E_m (# is 1 to 5 corresponding to the percentile number.

Perc#Closest: The closest possible percentile to the percentile specified in E_m. (Perc#Closest will be very close to the percentile specified in E_m when n is larger than a few hundred; # is 1 to 5 corresponding to the percentile number.).

Histogram: All bin counts less than the lower limit of the first bin value are counted in the first histogram column (directly under the 'histogram' column header). A number of unlabeled columns follow after the 'histogram' column header: these contain the counts for each histogram bin. A particle is counted in a bin if it is greater than the lower bin limit and is less than or equal to the upper bin limit as defined in F_m, and described in CORENAME_PARAMETER_HISTOGRAM_LIMITS.txt (Appendix C, part 3). On the first bin (the column immediately to the right of the column labeled 'histogram'), a particle is counted if it is greater than *or equal to* the lower bin limit. The number of columns is the same as the number of

histogram bins *plus one*. *Plus one* because the last column is the number of particles greater than the upper bin limit set in F_m. Bin boundaries can increase linearly, can increase on the phi scale, or $\log_{10}$ scale. This is explained in the Measurement Dialog section that describes F_m.

3 - CORENAME_PARAMETER_HISTOGRAM_LIMITS.txt

(3eg-1_AREA_HISTOGRAM_LIMITS.txt)

EXPLANATION: The upper and lower limits of each histogram bin. The number of rows equals the number of bins specified in F_m.

4- CORENAME_PARAMETER_RAWDATA_#.txt

These data files contain the 'raw data' for each particle within a ROI. The data are one column wide, and are for the parameter written in the file name (i.e. area, circularity, etc.). The files are numbered with 1 being measurements from the topmost ROI. Data are scale-transformed where appropriate (i.e. for area, major axis and minor axis, but not for circularity or angle).

5- CORENAME_CRACKAREA.txt

This comma delimited file is produced if D_p is chosen. The file lists the total area of disturbances within a binary crack image for each ROI.

Units are in microns, except for 'Area' and 'Crack Area', which are in microns squared.

FILE STRUCTURE:

X: left edge of the measuring box x-coordinate

Y: top edge of the measuring box y-coordinate

Width: measuring box width

Height: measuring box height

Area: measuring box area

Mid_Y: y-coordinate of the midpoint of the measuring box

Crack_Area: the black area for each measuring box, representing cracks or other disturbances.

The percentage of cracks per ROI can be calculated using *Area* and *Crack_Area*.

APPENDIX D

ADDITIONAL IMAGEJ MACROS:

CODE AND DESCRIPTION FOR

ENHANCEMENT, THRESHOLD_PAUSE, AND *WATERSHED_FILLHOLES*

These macros are also available at http://www.geo.umass.edu/climate/lewis/analysis/

Enhancement

- Performs image enhancement, which helps bright objects to be separated from the background.
- Runs: Enhance contrast, median filter, sharpen algorithms.
- This improves the success rate of watershedding, and filling holes.

```
macro 'Image Enhancement [4]' {
	dir = getDirectory("Choose a Directory ");
	list = getFileList(dir);
	start = getTime();
	for (i=0; i<list.length; i++) {
		path = dir+list[i];
		open(path);
		title = getTitle();
		run("Enhance Contrast", "saturated=2 normalize");
		run("Median...", "radius=2"); // median filter replaces pixel with median
of neighbors - removes noise
		run("Sharpen");
		run("Median...", "radius=2");
		run("Subtract...", "value=1"); // so white (255) is thresholded
		run("Tiff...", "save=["+path+"]");
		num= i+1;
		tot= list.length;
		print ("image= "+title+"... "+num+" of "+tot+"");
		selectImage(title);
		run("Close");
	}
print("The macro took this many seconds...")
print((getTime()-start)/1000);
}
```

Threshold_Pause

- A time saving tool for thresholding large numbers of greyscale images.
- Operates on all images in a directory (there should not be any files in the directory that you don't want to threshold).
- The user sets the desired upper and lower greylevel values, then presses 'b', which performs the thresholding, and saves the binary image as a binary .gif (also adds a -bin extension to the filename).

```
var dirout;
var abort;

macro 'RUN FIRST [9]' {
	abort=false;
	dir = getDirectory("Choose an Input Directory ");
	dirout = getDirectory("Choose Output (Save To) Directory");
	list = getFileList(dir);
	for (i=0; i<list.length; i++) {
		name = list[i];
		path = dir+name;
		open(path);
		setThreshold(95, 255);
		run("Threshold...");
		while (isOpen(name)) {
			wait(10);
			if (abort) {print("Aborted"); exit();}
		}
	}
}

macro 'Binary and Save [b]' {
	title = getTitle();
	pathout = dirout+title;
	getThreshold(lower, upper);
	run("Apply LUT");
	print(""+title+", "+lower+", "+upper+"");
	dotIndex = lastIndexOf(pathout, ".");
	if (dotIndex!=-1) {
		pathsave = substring(pathout, 0, dotIndex); // remove extension
		save(pathsave+"-bin.gif");
	}
	selectImage(1);
	close();
}

macro "Abort" {
```

```
        abort = true;
}
```

Watershed_FillHoles

- Separates particles using the 'watershed' algorithm, then runs 'fill holes' to enclose white pixels that are completely enclosed by black pixels.

```
macro 'Fill Holes & Waterhshed [4]' {
    dir = getDirectory("Choose a Directory ");
    list = getFileList(dir);
    setBatchMode(true);
    for (i=0; i<list.length; i++) {
            showProgress(i+1, list.length);
            path = dir+list[i];
            open(path);
            title = getTitle();
            run("Fill Holes");
            run("Watershed");
            dotIndex = lastIndexOf(path, ".");
            if (dotIndex!=-1) {;
                    path = substring(path, 0, dotIndex); // remove extension
                    save(path+".gif");
            }
            run("Close");
    }
}
```

ROI Imager

- Draws ROI on an image. Requires a space delimited input file with x,y, width, height coordinates.
- This macro is useflu for checking that your ROI coordinate file is constructed properly.

```
showMessage("Open a space delimited coordinate file\nmake sure there are no empty lines at the file's beginning or end"); open("");
arraySplit = split(getInfo(),'\n');
run ("Close");

arrayWidth = newArray(2);
Dialog.create("Set ROI Parameters");
    Dialog.addNumber("ROI Line Width:", 10);
    Dialog.addNumber("ROI Line Grayscale Value (0-255):", 150);
    Dialog.show();
    arrayWidth[0] = Dialog.getNumber();
```

```
    arrayWidth[1] = Dialog.getNumber();

showMessage("Open image \nmake sure no scale is set"); open("");

setLineWidth(arrayWidth[0]);
setColor(arrayWidth[1]);

for (m=0; m<arraySplit.length; m++) {
    arraySubSplit = split(arraySplit[m]);
    tx = parseInt(arraySubSplit[0]);
    ty = parseInt(arraySubSplit[1]);
    tw = parseInt(arraySubSplit[2]);
    th = parseInt(arraySubSplit[3]);
    drawRect(tx, ty, tw, th);
}
```

BIBLIOGRAPHY

Abbott MB., Stafford TW., Jr (1996) Radiocarbon geochemistry of modern and ancient Arctic lake systems, Baffin Island, Canada. Quaternary Research 45: 300-311

Abdalati W, Krabill W, Frederick E, Manizade S, Martin C, Sonntag J, Swift R, Thomas R, Yungel J and Koerner RM (2004) Elevation changes of ice caps in the Canadian Arctic Archipelago. Journal of Geophysical Research. DOI:10.1029/2003JF000045

Alley RB, Marotzke J, Nordhaus WD, Overpeck JT, Peteet DM, Pielke RA, Jr, Pierrehumbert RT, Rhines PB, Stocker TF, Talley LD and Wallace JM (2003) Abrupt Climate Change. Science 299: 2005-2010

Anguy Y, Ehrlich R, Prince CM, Riggert VL and Bernard D (1994) The sample support problem for permeability assessment is sandstone reservoirs. In: J. M. Yarus and R. L. Chambers (eds), Stochastic modelling and geostatistics; principles, methods and case studies: Computer Applications in Geology. American Association of Petroleum Geologists, Tusla, pp. 37-54

Atwater BF (1984) Periodic floods from glacial Lake Missoula into the Sanpoil arm of glacial Lake Columbia, northeastern Washington. Geology 12: 464-467

Atwater BF (1986) Pleistocene glacial-lake deposits of the Sanpoil River valley, northeastern Washington. United States Government Printing Office, Washington, 36 pp

Beierle BD, Lamoureux SF, Cockburm JMH and Spooner I (2002) A new method for visualizing sediment particle size distributions. Journal of Paleolimnology 27: 279-283

Belzile C, Vincent WF, Gibson JAE and Van Hove P (2001) Bio-optical characteristics of the snow, ice, and water column of a perennially ice-covered lake in the High Arctic. Canadian Journal of Fisheries and Aquatic Science 58: 2405-2418

Benn DI and Evans DJA (1998) Glaciers & glaciation. Hodder Arnold, London, 734 pp

Besonen M, Patridge W, Bradley RS, Francus P, Stoner JS and Abbott MB (2008) A record of climate over the last millennium based on varved lake sediments from the Canadian High Arctic. The Holocene 18: 169-180

Best JL, Kostaschuk RA, Peakall J, Villard PV and Franklin M (2005) Whole flow field dynamics and velocity pulsing within natural sediment-laden underflows. Geology 33: 765-768

Björnsson H (2002) Subglacial lakes and jökulhlaups in Iceland. Global and Planetary Change 35: 255-271

Blachut SP and McCann SB (1981) The behavior of a polar ice-dammed lake, Ellesmere Island, NWT., Canada. Arctic and Alpine Research 13: 63-74

Blais-Stevens A, Clague JJ, Mathewes RW, Hebda RJ and Bornhold BD (2003) Record of large, Late Pleistocene outburst floods preserved in Saanich Inlet sediments, Vancouver Island, Canada. Quaternary Science Reviews 22: 2327-2334

Boehrer B and Schultze M (2008) Stratification of lakes. Review of geophysics 46: 27 pp. DOI: DOI:10.1029/2002GL015082

Boggs SJ (1987) Principles of sedimentology and stratigraphy. Macmillan Publishing, New York, NY, 784 pp

Bowman TE and Long A (1968) Relict Populations of *Drepanopus bungei* and *Limnocalanus macrurus grimaldii* (Copepoda: Calanoida) from Ellesmere Island, N.W.T. Arctic 21: 172-180

Bradley RS, Retelle MJ, Ludlam SD, Hardy DR, Zolitschka B, Lamoureux SF and Douglas MSV (1996) The Taconite Inlet Lakes Project; a systems approach to paleoclimatic reconstruction. Journal of Paleolimnology 16: 97-110

Braun C (1997) Streamflow and sediment transport prediction in two High Arctic watersheds, Nunavut, Canada. Geosciences, University of Massachusetts, Amherst, MA, p. 167

Braun C, Hardy DR and Bradley RS (2000a) Hydrological and meteorological observations at Lake Tuborg, Ellesmere Island, Nunavut, Canada. Polar Geography 24: 83-97

Braun C, Hardy DR, Bradley RS and Retelle MJ (2000b) Streamflow and suspended sediment transfer to Lake Sophia, Cornwallis Island, Nunavut, Canada. Arctic, Antarctic, and Alpine Research 32: 456-465

Carmack EC (1979) Combined influence of inflow and lake temperatures on spring circulation in a riverine lake. Journal of Physical Oceanography 9: 422-434

Carmack EC, Gray, CBJ, Pharo, CH, Daley, RJ (1979) Importance of lake-river interaction on seasonal patterns in the general circulation of Kamloops Lake, British Columbia. Limnology and Oceanography 24: 634-644

Chapman R (2006) A sea water equation of state calculator. http://ioc.unesco.org/Oceanteacher/oceanteacher2/01_GlobOcToday/02_CollDta/02_OcDtaFunda/02_OcMeasUnits/SWequationofstatecalculator.htm [last accessed August. 6, 2007]

Chikita KA, Smith ND, Yonemitsu N and Perez Arlucea M (1996) Dynamics of sediment-laden underflows passing over a subaqueous sill; glacier-fed Peyto Lake, Alberta, Canada. Sedimentology 43: 865-875

Child JK, Werner A (1999) Evidence for a hardwater radiocarbon dating effect, Wonder Lake, Denali National Park and Preserve, Alaska. Géographie physique et Quaternaire 53: 407-411

Church M (1972) Baffin Island sandurs; a study of arctic fluvial processes. Bulletin - Geological Survey of Canada 216: 208

Church M (1988) Floods in cold climates. In: V R Baker, R C Kochel and P C Patton (eds), Flood Geomorphology. Wiley, New York, pp. 205-229

Chutko KJ and Lamoureux SF (2008) Identification of coherent links between interannual sedimentary structures and daily meteorological observations in Arctic proglacial lacustrine varves: potentials and limitations. Canadian Journal of Earth Sciences 45: 1-13

Clague JJ and Mathews WH (1973) The magnitude of jökulhlaups. Journal of Glaciology 12: 501-504

Clague JJ and Evans SG (1994) Formation and failure of natural dams in the Canadian Cordillera, 35

Clague JJ, Barendregt R, Enkin RJ and Foit FFJ (2003) Paleomagnetic and tephra evidence for tens of Missoula floods in southern Washington. Geology 31: 247-250

Cockburn JMH and Lamoureux SF (2008) Hydroclimate controls over seasonal sediment yield in two adjacent High Arctic watersheds. Hydrological Processes 22: 2013-2027

Cogley JG and McCann SB (1976) An exceptional storm and its effects in the Canadian High Arctic. Arctic and Alpine Research 8: 111-114

Colman SM (2002) A Fresh Look at Glacial Floods. Science 296: 1251-1252

Dean JM, Kemp AES, Bull D, Pike J, Patterson G and Zolitschka B (1999) Taking varves to bits: Scanning electron microscopy in the study of laminated sediments and varves. Journal of Paleolimnology 22: 121-136

Doran PT, Wharton RA, Jr and Lyons WB (1994) Paleolimnology of the McMurdo Dry Valleys, Antarctica. Journal of Paleolimnology 10: 85-114

Engstrom DR and Wright HE (1984) Chemical stratigraphy of lake sediments as a record of environmental change. In: Y Haworth and WG Lund (eds), Lake sediments and environmental history. Leicester University Press, Bath, pp. 11-68

Evans SG and Clague JJ (1994) Recent climatic change and catastrophic geomorphic processes in mountain environments. Geomorphology 10: 107-128

Fisher DA, Koerner RM and Reeh N (1995). Holocene climatic records from Agassiz Ice Cap, Ellesmere Island, NWT, Canada. The Holocene 5: 19-24

Francus P (1998) An image analysis technique to measure grain-size variation in thin sections of soft clastic sediments. Sedimentary Geology 121: 289-298

Francus P and Karabanov E (2000) A computer-assisted thin-section study of Lake Baikal sediments: a tool for understanding sedimentary processed and deciphering their climatic signal International. Journal of Earth Sciences 89: 260-267

Francus P and Asikainen CA (2001) Sub-sampling unconsolidated sediments: A solution for the preparation of undisturbed thin-sections from clay-rich sediments. Journal of Paleolimnology 26: 323-326

Francus P and Pirard E (2004) Testing for sources of errors in quantitative image analysis. In: P. Francus (ed), Image analysis, sediments and paleoenvironments. Springer, Dordrecht, pp. 87-104

Francus P, Bradley RS, Abbott MB, Patridge W and Keimig F (2002) Paleoclimate studies of minerogenic sediments using annually resolved textural patterns. Geophysical Research Letters. DOI:10.1029/2002GL015082

Francus P, Keimig F and Besonen M (2002) An algorithm to aid varve counting and measurement from thin-sections. Journal of Paleolimnology 28: 283-286

Francus P, Bradley RS, Lewis T, Abbott MB, Retelle MJ and Stoner JS (2008) Limnological and sedimentary processes at Sawtooth Lake, Canadian High Arctic, and their influence on varve formation. Journal of Paleolimnology. DOI: 10.1007/s10933-008-9210-x

Gee MJR Masson, DG Watts AB and Mitchell NC (2001) Passage of debris flows and turbidity currents through a topographic constriction: Seafloor erosion and deflection of flow pathways. Sedimentology 48: 1389-1409

Geertsema M and Clague JJ (2005) Jökulhlaups at Tulsequah Glacier, northwestern British Columbia, Canada. The Holocene 15: 310-316

Geyer WR and Smith JD (1987) Shear instability in a highly stratified estuary. Journal of Physical Oceanography 17: 1668-1679

Gilbert R (1971) Observations on ice-dammed Summit Lake, British Columbia. Journal of Glaciology 10: 351-356

Gilbert R (1975) Sedimentation in Lillooet Lake, British Columbia. Canadian Journal of Earth Sciences 12: 1697-1711

Gilbert R (2000) Environmental assessment from the sedimentary record of high-latitude fiords. Geomorphology 32: 295-314

Gilbert R and Shaw J (1981) Sedimentation in proglacial Sunwapta Lake, Alberta. Canadian Journal of Earth Sciences 18: 81-93

Gilbert R, Desloges JR and Clague JJ (1997) The glacilacustrine sedimentary environment of Bowser Lake in the northern Coast Mountains of British Columbia, Canada. Journal of Paleolimnology 17: 331-346

Gilbert R, Crookshanks S, Hodder KR, Spagnol J and Stull RB (2006) The record of an extreme flood in the sediments of montane Lillooet Lake, British Columbia: implications for paleoenvironmental assessment. Journal of Paleolimnology 35: 737-745

Håkanson L and Jansson M (1983) Principles of lake sedimentology. Springer-Verlag, New York, NY

Hambley GW and Lamoureux SF (2006) Recent summer climate recorded in complex varved sediments, Nicolay Lake, Cornwall Island, Nunavut. Journal of Paleolimnology 35: 629-640

Hardy DR (1996) Climatic influences on streamflow and sediment flux into Lake C2, northern Ellesmere Island, Canada. Journal of Paleolimnology 16: 133-149

Hardy DR, Bradley RS and Zolitschka B (1996) The climatic signal in varved sediments from Lake C2, northern Ellesmere Island, Canada. Journal of Paleolimnology 16: 227-238

Hattersley-Smith G and Serson H (1964) Stratified water of a glacial lake in northern Ellesmere Island. Arctic 17: 108-111

Head KH (1992) Manual of soil laboratory testing. Pentech Press, London, UK 388 pp

Hill PS, Milligan TG and Geyer WR (2000) Controls on effective settling velocity of suspended sediment in the Eel River flood plume. Continental Shelf Research 20: 2095-2111

Hill PS, Syvitski JP, Cowan EA and Powell RD (1998) *In situ* observations of floc settling velocities in Glacier Bay, Alaska. Marine Geology 145: 85-94

Hodder KR, Gilbert R and Desloges JR (2007) Glaciolacustrine varved sediment as an alpine hydroclimatic proxy. Journal of Paleolimnology 38: 365-394

Hoyal DCJD, Bursik MI and Atkinson JF (1999) Settling-driven convection: a mechanism of sedimentation from stratified fluids. Journal of Geophysical Research 104: 7953-7966

Hydat CD-ROM (2005). Surface Water and Sediment Data. Water Survey of Canada. http://www.wsc.ec.gc.ca/products/main_e.cfm?cname=products_e.cfm. Last accessed January 8, 2009

Hutchinson GE (1937) A contribution to the limnology of arid regions. Trans. Conn. Acad. Arts Sci. 33: 47-132

Jones LM and Faure G (1972) The isotopic composition and concentration of strontium of the brine from Tuborg Lake, Ellesmere Island Arctic 25: 154-155

JPOTS Editorial Panel (1991) Processing of Oceanographic Station Data. UNESCO, Paris, FR 138 pp

Klingbjer P (2004) Recurring jökulhlaups in Sälka, northern Sweden. Geografiska Annaler 86: 169-179

Koerner RM (2005) Mass balance of glaciers in the Queen Elizabeth Islands, Nunavut, Canada. Annals of Glaciology 42: 417-423

Kranck K (1973) Flocculation of suspended sediment in the sea. Nature 246: 348-350

Lambert A and Giovanoli F (1988) Records of riverborne turbidity currents and indications of slope failures in the Rhone Delta of Lake Geneva. Limnology and Oceanography 33: 458-468

Lamoureux SF (1999) Spatial and interannual variations in sedimentation patterns recorded in nonglacial varved sediment in the High Arctic. Journal of Paleolimnology 21: 73-84

Lamoureux SF (2000) Five centuries of interannual sediment yield and rainfall-induced erosion in the Canadian High Arctic recorded in lacustrine varves. Water Resources Research 36: 309-318

Lamoureux SF and Bollmann J (2004) Image Acquisition. In: P. Francus (ed.), Image Analysis, Sediments and Paleoenvironments. Springer, Dordrecht, NL pp. 11-34

Lamoureux SF and Gilbert R (2004) A 750-year record of autumn snowfall and temperature variability and winter storminess recorded in the varved sediments of Bear Lake, Devon Island, Arctic Canada. Quaternary Research 61: 134-147

Lamoureux SF, England JH, Sharp MJ and Bush BG (2001) A varve record of increased 'little ice age' rainfall associated with volcanic activity, Arctic archipelago, Canada. The Holocene 11: 243-249

Leonard EM (1986) Varve Studies at Hector Lake, Alberta, Canada and the Relationship Between Glacial Activity and Sedimentation. Quaternary Research 25: 199-214

Lewis T, Gilbert R and Lamoureux SF (2002) Spatial and temporal changes in sedimentary processes at proglacial Bear Lake, Devon Island, Nunavut. Arctic, Antarctic, and Alpine Research 34: 119-129

Lewis T, Braun C, Hardy DR, Francus P and Bradley RS (2005) An extreme sediment transfer event in a Canadian High Arctic stream. Arctic, Antarctic, and Alpine Research 37: 477-482

Lewis T, Francus P and Bradley RS (2007) Limnology, sedimentology, and hydrology of a jökulhlaup into a meromictic high arctic lake. Canadian Journal of Earth Sciences 44: 791-806

Lewis T, Francus P and Bradley RS (2009) Recent occurrence of large jökulhlaups at Lake Tuborg, Ellesmere Island, Nunavut. Journal of Paleolimnology DOI: 10.1007/s10933-008-9240-4

Lewkowicz AG and Wolfe PM (1994) Sediment transport in Hot Weather Creek, Ellesmere Island, N.W.T., Canada, 1990-1991. Arctic and Alpine Research 26: 213-226

Liestøl O (1956) Glacier dammed lakes in Norway. Norsk geografisk tidsskrift 15: 122-149

Long A (1967) Age of trapped sea-water at the bottom of Lake Tuborg, Ellesmere Island, N.W.T. Transactions, American Geophysical Union 48: 136

Ludlam SD (1996) The comparative limnology of high arctic, coastal, meromictic lakes. Journal of Paleolimnology 16: 111-131

Maag H (1969) Ice dammed lakes and marginal glacial drainage on Axel Heiberg Island, Axel Heiberg Island Research Reports. McGill University, Montreal, PQ p. 147

Maizels J and Russell A (1992) Quaternary perspectives on jökulhlaup prediction. Quaternary Proceedings 2: 133-152

Marcus MG (1960) Periodic drainage of glacier-dammed Tulsequah Lake, British Columbia. Geol. Rev. 50: 89-106

Maria A, Carey S, Sigurdsson H, Kincaid C and Helgadóttir G (2000) Source and dispersal of jökulhlaup sediments discharged to the sea following the 1996 Vatnajökull eruption. Geological Society of America Bulletin 112: 1507-1521

Marren PM (2005) Magnitude and frequency in proglacial rivers: a geomorphological and sedimentological perspective. Earth-Science Reviews 70: 203-251

McCool WW and Parsons JD (2004) Sedimentation from buoyant fine-grained suspensions. Continental Shelf Research 24: 1129-1142

McLeod P, Carey S and Sparks SJ (1999) Behaviour of particle-laden flows into the ocean: experimental simulation and geological implications. Sedimentology 46: 523-536

Menounos B. (2006) Anomalous early 20th century sedimentation in proglacial Green Lake, British Columbia, Canada. Canadian Journal of Earth Sciences 43: 671-678

Milliman JD and Syvitski JPM (1992) Geomorphic/tectonic control of sediment discharge to the ocean: the importance of small mountainous rivers. The Journal of Geology 100: 525-544

Mulder T and Syvitski JPM (1995) Turbidity currents generated at river mouths during exceptional discharges to the world oceans. Journal of Geology 103: 285-299

Mulder T and Alexander J (2001) The physical character of subaqueous sedimentary density flows and their deposits. Sedimentology 48: 269-299

Mulder T, Syvitski JPM, Migeon S, Faugeres J-C and Savoye B (2003) Marine hyperpycnal flows: initiation, behavior and related deposits. A review. Marine and Petroleum Geology 20: 861-882

Naruse H and Masuda F (2006) Visualization of the internal structure of the massive division in experimental sediment-gravity-flow deposits by mapping of grain fabric. Journal of Sedimentary Research 76: 854-865

Nederbragt AJ, Francus P, Bollmann J and Soreghan MJ (2004) Image calibration, filtering and processing. In: P Francus (ed.), Image Analysis, Sediments and Paleoenvironments. Springer, Dordrecht, pp 35-58

Ng F and Björnsson H (2003) On the Clague-Mathews relation for jökulhlaups. Journal of Glaciology 49: 161-172

Ng F, Liu S, Mavlyudov B and Wang Y (2007) Climatic control on the peak discharge of glacier outburst floods. Geophysical Research Letters DOI:10.1029/2007GL031426

Ohlendorf C, Niessen F and Weissert H (1997) Glacial varve thickness and 127 years of instrumental climate data: a comparison. Climatic Change 36: 391-411

Ojala AE and Francus P (2002) Comparing X-ray densiometry and BSE-image analysis of thin section in varved sediments. Boreas 31: 57-64

Old GD, Lawler D, M and Snorrason Á (2005) Discharge and suspended sediment dynamics during two jökulhlaups in the Skaftá river, Iceland. Earth Surface Processes and Landforms 30: 1441-1460

Oswald WW, Anderson PM, Brown TA, Brubaker LB, Hu FS, Lozhkin AV, Tinner W and Kaltenrieder P (2005) Effects of sample mass and macrofossil type on radiocarbon dating of arctic and boreal lake sediments. The Holocene 15: 758-767

Ouellet M, Dickman M, Bisson M and Pagé P (1989) Physico-chemical characteristics and origin of hypersaline meromictic Lake Garrow in the Canaidan High Arctic. Hydrobiologia 172: 215-234

Overpeck J, Hughen KA, Hardy D, Bradley R, Case R, Douglas M, Finney B, Gajewski K, Jacoby G, Jennings A, Lamoureux S, Lasca A, MacDonald G, Moore J, Retelle M, Smith S, Wolfe A and Zielinski G (1997) Arctic environmental change of the last four centuries. Science 278: 1251-1256

Pagé P, Ouellet M, Hillaire-Marcel C and Dickman M (1984) Isotopic analyses (18O, 13C, 14C) of two meromictic lakes in the Canadian High Arctic. Limnology and Oceanography 29: 564-573

Parsons JD, Bush JWM and Syvitski JPM (2001) Hyperpycnal plume formation from riverine outflows with small sediment concentrations. Sedimentology 48: 465-478

Parsons JD, Friedrichs CT, Traykovski PA, Mohrig D, Imran J, Syvitski JPM, Parker G, Puig P, Buttles JL and Garcia MH (2007) The mechanics of marine sediment gravity flows In: C Nittrouer, J Austin, M Field, J Kravitz, J P M Syvitski and P Wiberg (eds), Continental Margin Sedimentation. Wiley-Blackwell, pp. 275-337

Peach PA and Perrie LA (1975) Grain-size distribution within Glacial Varves. Geology 3: 43-46

Pharo CH and Carmack EC (1979) Sedimentation processes in a short residence-time intermontane lake, Kamloops Lake, British Columbia. Sedimentology 26: 523-540

Phelps KJ (1996) Laminated lacustrine sediments from glacial Lake Tuborg, Northern Ellesmere Island, Canada. Geology. Bates College, Lewiston, ME, p. 85

Prowse TD (1990) Northern hydrology: an overview. In: T D Prowse and C S L Ommanney (eds), Northern hydrology, Canadian Perspectives. National Hydrology Research Institute, Saskatoon, pp 1-36

Rasband WS (2008) ImageJ. U. S. National Institutes of Health, Bethesda, MD, USA

Reading HG (1996) Sedimentary environments: processes, facies and stratigraphy. Blackwell Publishing, Oxford, 704 pp

Reedyk S., Cooke S., Burchett G. and Prepas, E.E. 1997 Design for an inexpensive continuous digital output water level recorder. Water Resources Research 33: 1523-1526

Retelle MJ and Child JK (1996) Suspended sediment transport and deposition in a high arctic meromictic lake. Journal of Paleolimnology 16: 151-167

Rimoldi B, Alexander J and Morris S (1996) Experimental turbidity currents entering density stratified water: analogues for turbidites in Mediterranean hypersaline basins. Sedimentology 43: 527-540

Rittenour TM, Brigham-Grette J and Mann ME (2000) El Niño-like climate teleconnections in New England during the Late Pleistocene. Science 288: 1039-1042

Roberts MJ (2005) Jökulhlaups: a reassessment of floodwater flow through glaciers. Reviews of Geophysics, 43: RG1002, DOI:10.1029/2003RG000147. 21 pp

Roberts MJ, Tweed FS, Russell AJ, Knudsen Ó and Harris T (2003) Hydrologic and geomorphic effects of temporary ice-dammed lake formation during jökulhlaups. Earth Surface Processes and Landforms 28: 723-737

Rothwell RG, Hoogakker B, Thomson J, Croudace IW and Frenz M (2006) Turbidite emplacement on the southern Balearic Abyssal Plain (western Mediterranean Sea) during marine isotope stages 1-3: an application of ITRAX XRF scanning of sediment cores to lithostratigraphic analysis. In: RG Rothwell (ed), New techniques in sediment core analysis. The Geological Society Special Publications, London, pp. 79-98

Rushmer EL, Russell A, Tweed FS, Knudsen Ó and Marren PM (2002) The role of hydrograph shape in controlling glacier outburst flood (jökulhlaup) sedimentation. The structure, function and management implications of fluvial sedimentary systems. International Association of Hydrological Sciences, publication no. 276, Alice Springs, AU, pp. 305-313

Russ JC (2002) The Image Processing Handbook CRC Press, Boca Raton, 744 pp

Russell AJ (1989) A comparison of two recent jökulhlaups from an ice-dammed lake, Søndre Strømfjord, West Greenland. Journal of Glaciology 35: 157-162

Russell AJ, Roberts MJ, Fay H, Marren PM, Cassidy NJ, Tweed FS and Harris T (2006) Icelandic jökulhlaup impacts: implications for ice-sheet hydrology, sediment transfer and geomorphology. Geomorphology 75: 33-64

Schiefer E (2006) Depositional regimes and areal continuity of sedimentation in a montane lake basin, British Columbia, Canada. Journal of Paleolimnology 35: 617-628

Schlitzer R (2005) Ocean data view [online], Available from http://www.awi-bremerhaven.de/GEO/ODV [last accessed October 7, 2006]

Scranton MI, Astor Y, Bohrer R, Ho T-Y and Muller-Karger F (2001) Controls on temporal variability of the geochemistry of the deep Cariaco Basin. Deep-Sea Research I 48: 1605-1625

Seelos K and Sirocko F (2005) RADIUS - rapid particle analysis of digital images by ultra-high-resolution scanning of thin sections. Sedimentology 52: 662-681

Shaw J, Munro-Stasiuk M, Sawyer B, Beaney C, Lesermann J-E, Musacchio A, Rains B and Young RR (1999) The channeled scabland: back to Bretz? Geology 27: 605-608

Smith LN (2006) Stratigraphic evidence for multiple drainings of glacial Lake Missoula along the Clark Fork River, Montana, USA. Quaternary Research 66: 311-322

Smith ND and Ashley GM (1985) Proglacial Lacustrine Environment. In: G M Ashley, J Shaw and N D Smith (eds), Glacial Sedimentary Environments. Society of Paleontologists and Mineralogists, Tulsa, OK, pp. 135-246

Smith S.V., Bradley R.S. and Abbott M.B. (2004) A 300 Year Record of Environmental Change from Lake Tuborg, Ellesmere Island, Nunavut, Canada. Journal of Paleolimnology 32: 137-148

Smith SV (1997) A record of environmental change derived from varved sediments in lakes along the margin of the Agassiz Ice Cap. Geosciences. University of Massachusetts, Amherst, MA, 103 pp

Soreghan MJ and Francus P (2004) Processing backscattered electron digital images of thin sections. *In* Image Analysis, Sediments and Paleoenvironments. *Edited by* P. Francus. Springer, Dordrecht, NL pp. 203-228

Stewart KA, Lamoureux SF and Finney BP (2007) Multiple ecological and hydrological changes recorded in varved sediments from Sanagak Lake, Nunavut, Canada. Journal of Paleolimnology DOI: 10.1007/s10933-007-9153-7

Stewart KM and Platford RF (1986) Hypersaline gradients in two Canadian High Arctic lakes. Canadian Journal of Fisheries and Aquatic Sciences 43: 1795-1803

Stuiver M and Reimer PJ (2005) Radiocarbon Calibration Program Calib

Thorarinsson S (1939) The ice-dammed lakes of Iceland, with particular reference to their values as indicators of glacier oscillations. Geografiska Annaler 21: 216-242

Tomkins JD and Lamoureux SF (2005) Multiple hydroclimatic controls over recent sedimentation in proglacial Mirror Lake, southern Selwyn Mountains, Northwest Territories. Canadian Journal of Earth Sciences 42: 1589-1599

Toth DJ and Lerman A (1975) Stratified lake and oceanic brines: Salt movement and time limits of existence. Limnology and Oceanography 20: 715-728

Trettin HP (1996) Geology, parts of Greely Fiord East, Greely Fiord West and Cañon Fiord, District of Franklin, Northwest Territories. Geological Survey of Canada, Map 1888A, scale 1:250 000

Tweed FS (2000) Jökulhlaup initiation by ice-dam flotation: the significance of glacier debris content. Earth Surface Processes and Landforms 25: 105-108

Tweed FS and Russell AJ (1999) Controls on the formation and sudden drainage of glacier-impounded lakes: implications for jökulhlaup characteristics. Progress in Physical Geography 23: 79-110

User's Manual for SEASOFT-Win32: SBE Data Processing (2005). Sea-Bird Electronics, Inc, Bellevue, WA, p. 124

van den Berg EH, Bense VF and Schlager W (2003) Assessing textural variation in laminated sands using digital image analysis of thin sections. Journal of Sedimentary Research 73: 133-143

van Hove P, Belzile C, Gibson JA and Vincent WF (2006) Coupled landscape-lake evolution in High Arctic Canada. Canadian Journal of Earth Sciences 43: 533-546

Waitt RB (1984) Periodic jökulhlaups from Pleistocene glacial Lake Missoula--New evidence from varved sediment in northern Idaho and Washington. Quaternary Research 22: 46-58

Waitt J, RB (1985) Case for periodic, colossal jökulhlaups from Pleistocene glacial Lake Missoula. Geological Society of America Bulletin 96: 1271-1286

Walder JS and Costa JE (1996) Outburst floods from glacier-dammed lakes: the effect of mode of lake drainage on flood magnitude. Earth Surface Processes and Landforms 21: 701-723

Weirich FH (1985) Sediment budget for a high energy glacial lake. Geografiska Annaler 67 A: 83-99

Weirich FH (1986) The record of density-induced underflows in a glacial lake. Sedimentology 33: 261-277

Wheatcroft RA (2000) Oceanic flood sedimentation: a new perspective. Continental Shelf Research 20: 2059-2066

Wolfe AP, Miller GH, Olsen CA, Forman SL, Doran PT and Holmgren SU (2004) Geochronology of high latitude lake sediments. In: R Pienitz, M S V Douglas and J P Smol (eds), Long-term Environmental Change in Arctic and Antarctic Lakes. Springer, Dordrecht, NL pp. 19-52

Wüest A and Lorke A (2003) Small-scale hydrodynamics is lakes. Annual Review of Fluid Mechanics 35: 373-412

Zolitschka B (1996) Recent sedimentation in a high arctic lake, northern Ellesmere Island, Canada. Journal of Paleolimnology 16: 169-186

Zwally HJ, Schutz R, Bentley C, Bufton J, Herring T, Minster J, Spinhirne J and Thomas R (2003, updated 2007) GLAS/ICESat L2 Global Land Surface Altimetry Data, Release 28. National Snow and Ice Data Center, Boulder, CO. Digital media